Doctoral Thesis at Chuo University

Development of Laser Ablation in Liquid for the Determination of Trace Elements in Hard-to-digest Ceramics by ICPMS

Ryo MACHIDA

Graduate School of Science and Engineering

Applied Chemistry Course

Chuo University

March 2016

Abstract

In resent, a power semiconductor device using silicon carbide (SiC) materials was developed, and elemental analysis of these samples was needed for control for semiconductor manufacturing. Although silicon carbide (SiC) are difficult to be decomposed by acid digestion, Laser ablation–inductively coupled plasma mass spectrometry (LA-ICPMS) is able to determine trace elements in hard-to-digest samples such as SiC without any sample preparation. However, LA-ICPMS suffers from elemental fractionation, a phenomenon in which the elements in a sample are enriched (or depleted) during LA and in the ICP, depending on the elemental properties. In order to obtain more-accurate data, certified reference materials (CRMs) which have a similar matrix to the sample have to be prepared for calibration.

In this study, we focused on the reason why elemental fractionation occurs during LA and in the ICP separately. Furthermore, we developed laser ablation in liquid (LAL)-ICPMS as a new quantification technique for the determination of trace elements in hard-to-digest ceramics.

A fractionation index (FI) is a good indicator of elemental fractionation because it indicates a transition of elemental ratio during LA-ICPMS. When laser ablation was performed under defocus conditions, FI peak was observed at 2-3 min after the start of ablation and then, most of elements which have this peak were volatile elements. We considered that this phenomenon was very useful to understand elemental fractionation by LA-ICPMS.

The results of SEM observation and size distributions of ablated particles were clarified that larger ablated particles were introduced into the ICP at 2-3 min. When larger ablated particles introduced into the ICP, the ablated particles larger than critical size could not be decomposed completely in the ICP.

On the other hand, the analytical result of chemical composition of ablated particles collected before introduced into the ICP indicates that volatile elements were enriched in the ablated particles smaller than sub-micrometer and were depleted in the ablated particles larger than sub-micrometer during LA process. As another fact, the both magnitudes of enrichment and depletion were constant during LA process. In summary, the volatile elements in larger particles were depleted during LA process but were enriched when the particles were introduced into the ICP. We confirmed that elemental fractionation was caused by temporal changes of size distribution of ablated particles.

For the development of LAL-ICPMS, LAL sampling was used to generate micro- to nanosized particles from a sample. LAL sampling generates particles smaller than several micrometers, and it transforms hard-to-digest crystals to soluble spherical particles. This allows LAL-sampled micro- to nanoparticles to easily decompose by acid digestion. The digested sample was measured by solution calibration ICPMS with high reliability. Here, we demonstrated for the first time that LAL sampling can be used to determine trace elements in hard-to-digest samples; sintered SiC and single-crystal SiC. Results obtained by LA-ICPMS and LAL-ICPMS were compared in terms of accuracy and limits of quantification.

Contents

Abstract ⋯ i

Chapter 1 General introduction ⋯ 1

1.1. Laser ablation-inductively coupled plasma mass spectrometry (LA-ICPMS) ⋯ 2

1.1.1. Introduction ⋯ 2

1.1.2. Elemental analysis by LA-ICPMS ⋯ 3

1.1.3. Elemental fractionation ⋯ 6

1.1.4. Comparison with secondary ionization mass spectrometry (SIMS), and glow discharge mass spectrometry (GD-MS) ⋯ 8

1.2. Laser ablation in liquid (LAL) ⋯ 11

1.2.1. Generation of nanomaterials by LAL ⋯ 11

1.2.2. LAL sampling for ICPMS measurements ⋯ 12

1.3. Silicon carbide (SiC) for semiconductor manufacturing ⋯ 14

1.3.1. Power semiconductor device ⋯ 14

1.3.2. Characteristics of SiC ⋯ 15

1.3.3. Social needs ⋯ 16

1.4. Objectives of the doctoral studies ⋯ 16

Chapter 2 Temporal changes of fractionation index explained by changes in the large size of ablated particles ⋯ 18

2.1. Introduction ⋯ 19

2.2. Experimental ⋯ 20

2.2.1. Instrumentation ⋯ 20

2.2.2. LA-ICPMS measurement ⋯ 21

2.2.3. Particle sampling and SEM observation ⋯ 24

2.2.4. Crater shape monitoring ⋯ 25

2.3. Results and discussion ⋯ 25

2.3.1. Single site mode ⋯ 25

2.2.2. Line-scan mode ⋯ 35

2.2.3. Classification of elements ⋯ 38

2.4. Summary ⋯ 43

Chapter 3 Temporal changes of size distribution of mass and relative intensity ⋯ 45

3.1. Introduction ⋯ 46

3.2. Experimental ⋯ 47

3.2.1. Instrumentation ⋯ 47

3.2.2. Reagents ⋯ 50

3.2.3. Collection of size-classified ablated particles with a low-pressure impactor ⋯ 50

3.2.4. Acid digestion ⋯ 52

3.3. Results and discussion ⋯ 52

3.3.1. Fractionation index obtained by means of LA-ICPMS with a cascade impactor ⋯ 52

3.2.2. Mass of size-classified ablated particles collected with a low-pressure impactor … 54

3.2.3. Chemical composition of size-classified ablated particles … 57

3.4. Summary … 60

Chapter 4 Particle size-related elemental fractionation in laser ablation in liquid (LAL) … 61

4.1. Introduction … 62

4.2. Experimental … 64

4.2.1. Instrumentation … 64

4.2.2. Reagents … 66

4.2.3. LAL sampling … 66

4.2.4. Acid digestion … 68

4.3. Results and discussion … 68

4.3.1. Optimization of the LAL sampling procedure … 68

4.3.2. Line-scanning mode and single-site mode … 71

4.3.3. Dependence of elemental fractionation on the size of particles generated by LAL in line-scanning mode … 73

4.3.4. Quantification of NIST 610 by LAL-ICPMS … 77

4.3.5. Comparison of elemental fractionation in the ICP with that during LAL sampling … 80

4.4. Summary … 82

Chapter 5 Determination of trace elements in silicon carbide (SiC) ⋯ 83

5.1. Introduction ⋯ 84

5.2. Experimental ⋯ 86

5.2.1. Instrumentation ⋯ 86

5.2.2. Calculation of ablated amounts and sampled amounts ⋯ 90

5.2.3. Reagents ⋯ 90

5.2.4. Sample preparation ⋯ 91

5.3. Results and discussion ⋯ 94

5.3.1. SEM observation of LAL-sampled particles ⋯ 94

5.3.2. Analysis of NMIJ 8001a and NMIJ 8002a CRMs ⋯ 96

5.3.3. Analysis of sintered SiC and single-crystal SiC ⋯ 99

5.4. Summary ⋯ 105

Chapter 6 Concluding remarks and future prospects ⋯ 107

References ⋯ 110

List of publications ⋯ 117

Acknowledgements ⋯ 118

Chapter 1

General introduction

1.1. Laser ablation-inductively coupled plasma mass spectrometry (LA-ICPMS)

1.1.1. Introduction

1.1.2. Elemental analysis by LA-ICPMS

1.1.3. Elemental fractionation

1.1.4. Comparison with secondary ionization mass spectrometry (SIMS), and glow discharge mass spectrometry (GD-MS)

1.2. Laser ablation in liquid (LAL)

1.2.1. Generation of nano-particles by LAL

1.2.3. LAL sampling for ICPMS measurements

1.3. Silicon carbide (SiC) for semiconductor manufacturing

1.3.1. Power semiconductor device

1.3.2. Silicon carbide

1.3.3. Social needs

1.4. Objectives of the doctoral studies

Chapter 1 General introduction

1.1. Laser ablation-inductively coupled plasma mass spectrometry (LA-ICPMS)

1.1.1. Introduction

The laser (light amplification by stimulated emission of radiation) was invented first by Maiman in 1960.[1] It was soon realized that high powered laser could be used for various fields. Various laser sources have been developed such as solid-state laser, gas laser, and semiconductor laser at present. A lot of lasers are used for heat treatment, generating fine particles, laser cutting, and laser marking, and so on.

On the other hand, Houk et al. reported that the ICP was used for the first time as an ion source for the analysis of elements in 1980.[2] The ICP is at a temperature between 6,000 and 10,000 K, depending on the region in the plasma. Elements in aerosol were melted, vaporized and then ionized in the ICP. ICPMS is generally used to measure samples that are solution with several percent acid. The sample solution was sprayed and introduced into the ICP with a nebulizer. The hyphenated technique LA-ICPMS was developed as a powerful tool for direct solid analysis by Alan Gray in 1985,[3] just five years after the ICP was first used for analysis.

LA-ICPMS permits multielement analysis with minimal sample preparation and is widely used for direct analysis of solid samples. A laser beam from the laser system is focused on the sample surface. The laser beam has a high peak power pulse, and then, a laser induced plasma and a shockwave are generated by interaction between the laser and the sample surface. The ablated particles are generated and introduced into the ICP by an inert gas stream. The LA has a minimum spatial resolution of 10 μm and a minimum depth resolution of 100 nm. LA-ICPMS is carried out under atmospheric pressure without sample pretreatment. The overall precision of LA-ICPMS has been reported to be better

than 5 %RSD for all samples, and the detection limits of trace elements were in a range from ng g^{-1} to μg g^{-1}.[4-5] Recently, D. Tabersky et al. reported that no ablation cell technique for a large stalagmite sample was developed by using a gas exchange device.[6]

1.1.2. Elemental analysis by LA-ICPMS

For elemental analysis with LA-ICPMS, geochemistry community continued to lead LA-ICPMS developments. In the geochemical field, geochemical age dating has been studied for a long time because isotopic ratio analysis was able to be performed without certified reference materials and inhomogeneous geological samples need the spatial resolution.[7-12] Recently, LA system was improved to achieve higher special resolution. The spot size of laser beam was focused narrowly until several micrometer, and a laser ablation cell was structurally-engineered to reduce wash-out time. The large format cell is shown in Fig. 1-1. The small volume of a quartz ring (such as 0.8 cm^3) was mounted just above the sample that was set in the large format cell (15 cm by 15 cm). In addition, the shorter integration time improved to achieve higher time resolution when signal intensity was obtained by ICPMS.[13] These improved techniques are able to perform elemental imaging for the samples of biological, environmental, and semiconductor materials which need high special resolution. The purpose of these studies was to visualize the element the sample surface by using the signal intensities of sample surface. Conversion of the visualized signal intensity distribution to quantitative data is required in the future.[14]

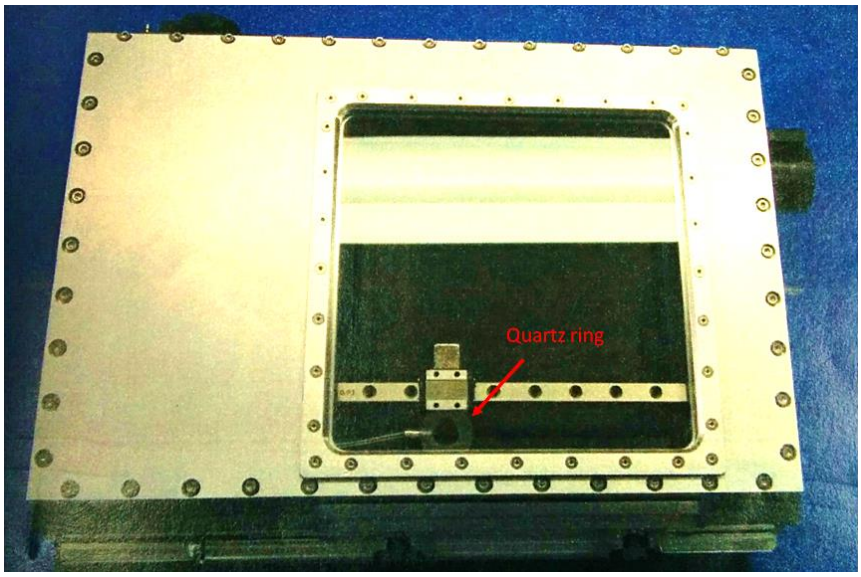

Fig. 1-1 The photograph of large format cell with quartz ring

When trace elements were quantified by means of LA-ICPMS, the precision and the accuracy of the data are worse than those obtained by solution nebulization ICPMS. To improve the precision of LA-ICPMS signal, it was required that a signal intensity was normalized by signals emitted from laser-induced plasma or signal intensity observed by ICPMS (Fig. 1-2).[15-17] Generally, internal standard was used as a main matrix element or a minor element that contained enough to detect. Certified reference material (CRMs) are required for calibration which has a similar matrix to the sample. Nevertheless, preparation of matrix matched CRMs is difficult and laborious. Therefore, some quantitative strategies were developed for LA-ICPMS; commercially available NIST reference glasses (SRM 610-617) were widely used for non-matrix matched calibration, and laboratory made disk-shaped pellet standards could be prepared by pressed powder sample after addition of standard solution. Schematic diagram of LA-ICPMS combination with an ultra-sonic nebulizer (USN) is shown in Fig. 1-3. If on-line solution-

based calibration procedure was used, relative sensitivity factor should be used for correction for signal intensities.[18, 19] It should be noted that the sensitivity (cps over ppm) of different matrix sample was related to ablated amount by LA and ionization efficiency in the ICP (Fig. 1-4).

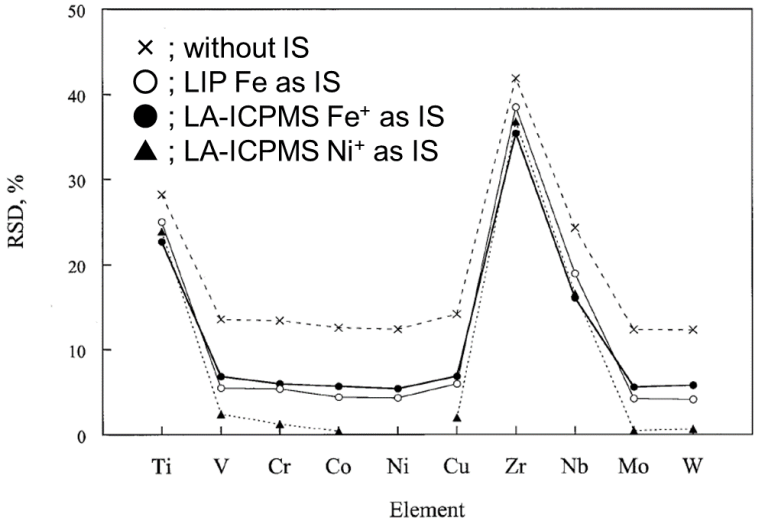

Fig. 1-2 Improvement of accuracy of LA-ICPMS by internal standard methods

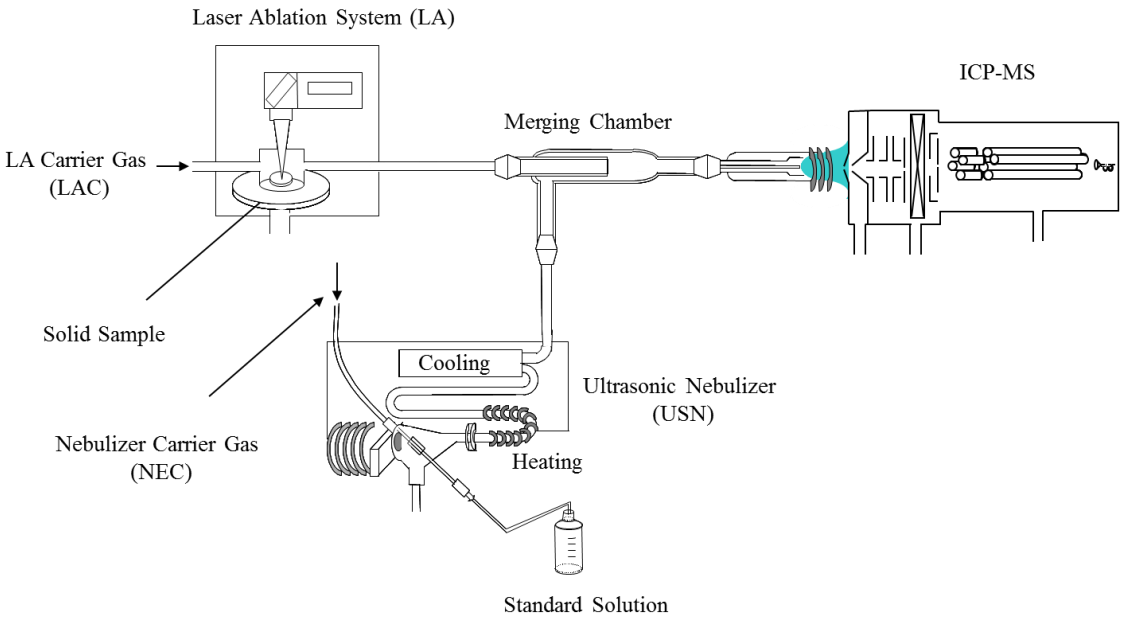

Fig. 1-3 Schematic diagram of LA-ICPMS combination with USN

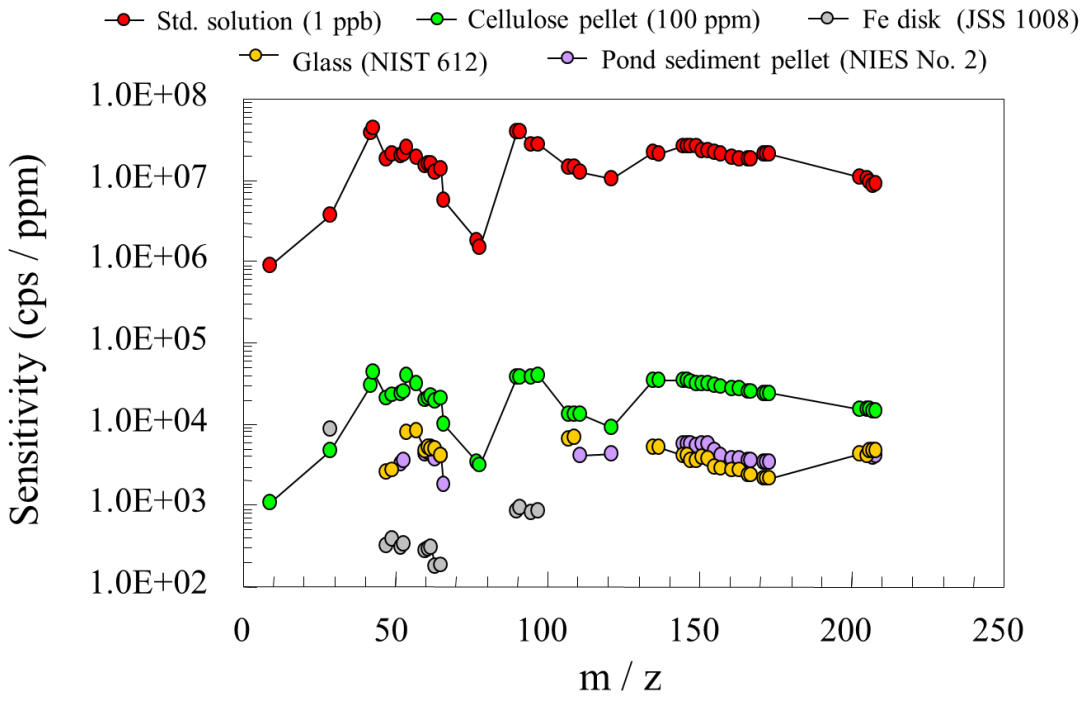

Fig. 1-4 Response curve obtained by LA-ICPMS combination with USN

1.1.3. Elemental fractionation

Elemental fractionation is a phenomenon that elements in a sample are enriched or depleted depending on the properties of the elements. In the quantification of the elements, LA-ICPMS is obstructed by the elemental fractionation because the elemental fractionation occurred during the laser ablation, transport process, and in the ICP. For the LA part, the sample surface was heated by laser energy. This heating can cause the preferential vaporization for volatile elements. It has been reported that the volatile elements such as As were enriched in smaller particles.

Ablated particles are not transported completely into the ICP[20], a part of ablated

particles adhere to the inner wall and are piled up around the crater. A transport efficiency of ablated particles corresponding to the tube length is listed in Table 1-1. The transport efficiency of ablated particles was reduced with increasing the tube length. The photograph of the crater after laser ablation during 10 min (Fig. 1-5a) and mapping data of the signal intensity of As and Zr are shown in Fig. 1-5b and Fig. 1-5c, respectively. The enrichment factor of As and Zr normalized by Ca are shown in Fig. 1-5d and Fig. 1-5e. These data indicate that the enrichment of volatile elements such as As was observed in the debris that were piled up around the crater. The enrichment of non-volatile elements such as Zr was not observed.

A lot of researches in recent years have focused on that how the wavelength and the pulse width of the laser affect the elemental fractionation.[9, 21] These studies have suggested that a short wavelength (such as the 193 nm wavelength of an excimer laser) can decrease the magnitude of elemental fractionation, and short pulse widths (such as femtosecond laser) also can decrease the magnitude of elemental fractionation.[22-24]

Fundamental mechanisms of laser ablation, such as vaporization, ionization and generation of particles, have been studied in efforts to achieve stoichiometric ablation, and ionization mechanisms in ICP also have been investigated.[25-30] It has been reported that when particles generated by LA were introduced into the ICP, mass-load-dependent matrix effects were caused in LA-ICPMS.[31]

Table 1-1 Transport efficiency corresponding to tube length

Tube length (m)	Transport efficiency (%)
1.8	35
3.2	31
6	25
10	21

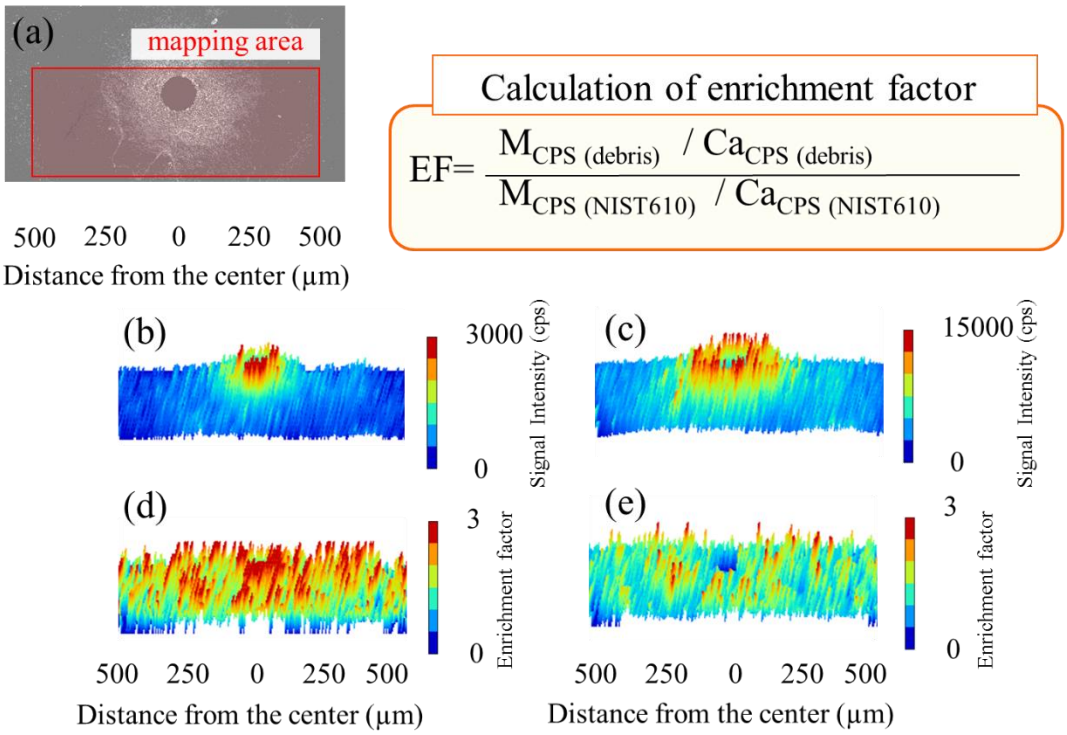

Fig. 1-5 (a) Photograph of ablate crater after laser ablation during 10 min, (b) mapping data of signal intensity of As, (c) mapping data of signal intensity of Zr, (d) mapping data of enrichment factor of As, and (e) mapping data of enrichment factor of Sr.

1.1.4. Comparison with secondary ionization mass spectrometry (SIMS), and glow discharge mass spectrometry (GD-MS)

LA-ICPMS, SIMS, and GD-MS is able to measure solid materials both in bulk and in spatially resolved analysis. These characteristics are summarized in Table 1-2.[5] LA-ICPMS is used for a high lateral resolution less than μm order. GD-MS is used for qualification and semi-quantification for bulk analysis. However, the detection limit of GD-MS is influenced by the matrix and conductivity of the sample. The detection limits of trace elements in semi-conductivity samples were reported as 1 to 100 μg g^{-1}.[32] GD-

MS provides a poor lateral resolution but an excellent depth resolution (nm order). SIMS is the most powerful method for micro region analysis compared with LA-ICPMS and GD-MS. The lateral resolution and depth resolution is nm-μm order and nm order, respectively. That is useful to obtain depth profile of ion-impurity (donner and accepter) for semiconductor. For the SIMS analysis, oblique impact angle and primary ion energy have to be optimized for each element.[33, 34] Therefore, SIMS is not suitable for quantitative analysis for trace elements. The precision and accuracy of trace element determination by inorganic mass spectrometry should be improved by direct solid analytical techniques. For quantitative analysis, CRMs are required to determination of elements for solid state analysis in almost case. It is necessary that interaction between ion source and sample should be corrected for by CRMs. From the point of the precision and accuracy, solution nebulization ICPMS is an excellent analytical technique because determination of ultratrace elements are performed by standard solution calibration without CRMs.[4]

Table 1-2 Summary of the most relevant characteristics of different analytical methods
Data were sited from Pisonero *et al.*[5]

	GD-MS	LA-ICP-MS	SIMS/SNMS
Analytical Information	Elemental/Molecular Isotopic	Elemental Isotopic	Elemental/Molecular Isotopic
Sample Vacuum Conditions	1–10 torr	760 torr (atmospheric)	<10–8 torr
Sample Throughput	~min/sample	~min/sample	~hour/sample
Depth Resolution	~nm	~100 nm	≤nm
Lateral Resolution	~mm	~μm	≤100 nm
Limits of Detection	≤μg/g	μg/g–ng/g	≤ng/g
Quantitative Analysis	Possible use of matrix and non-matrix matched calibration samples	Generally, matrix-matched calibration samples	Matrix-matched calibration samples required
Sample Size and Shape Requirements	Usually, flat surface with an area bigger than the GD anode diameter (4–8 mm)	Generally, limited by size of ablation cell.	Limited by size of sample holder
Typical sample consumption	(100 ng–100 μg)	(10 pg–100 ng)	(pg–ng)
Typical precision values	<3%	<5%	<10%
More information on sample requirements	Conductivity for dc-GD; Press pellets for the analysis of powders; Porous samples require special holder	Stable form (solid or pressed powder and dry or cooled-frozen)	Suitable for high vacuum conditions; usually flat surface; cells usually cryofixed and freeze-dried before embedding in resin

1.2. Laser ablation in liquid (LAL)

1.2.1. Generation of nano-particles by LAL

Laser ablation in liquid (LAL) was first reported as a technique for the generation of nanomaterials in 2003, and ablation mechanisms have been widely studied.[35, 36] The sample is set in an open-top chamber. Then, the sample surface was irradiated with the laser through the water. The laser pulse must pass through a layer of liquid before reaching the target. Laser energy should be delivered to the target only. In general, nano-particles were generated by thermodynamic mechanism under short pulse laser conditions such as hundreds of nanosecond laser. In contrast, ultra-short pulse laser such as femtosecond provide non-thermal ablation. In this case, the ablation mechanism is generically defined as fragmentation.

Amendola *et al.* and Itina *et al.* reported basic mechanism of LAL and generation of nano-particles.[37] Temporal sequence of the ablation stages is shown in Fig. 1-6. The lattice of sample surface was heated by the laser energy in a timescale of several picosecond. The nucleation for nano-materials formation occurred at that same time. Thermal processes of vaporization and boiling may lead to material detachment from sample surface. Shockwave propagation may promote the detachment of materials from the crater at the same time. The plasma plume is generated onto the crater area at 10^{-10}-10^{-7} sec. The evolution kinetic of the plasma plume is very fast, and then, solid fragments are able to be generated by the plasma plume. The plasma plume vanished at 10^{-8}-10^{-7} sec, and then, cavitation babble generates in a timescale of 10^{-7}-10^{-6} sec. The nano-particles in liquid is transferred by expanding of cavitation bubbles. Cavitation bubble's temperature decreases and bubble's internal pressure decreases to a value lower than that in the surrounding liquid. Shockwave by the bubble collapses is happened at 10^{-4} sec. The

nano-particle growth and agglomeration subsequently proceed.

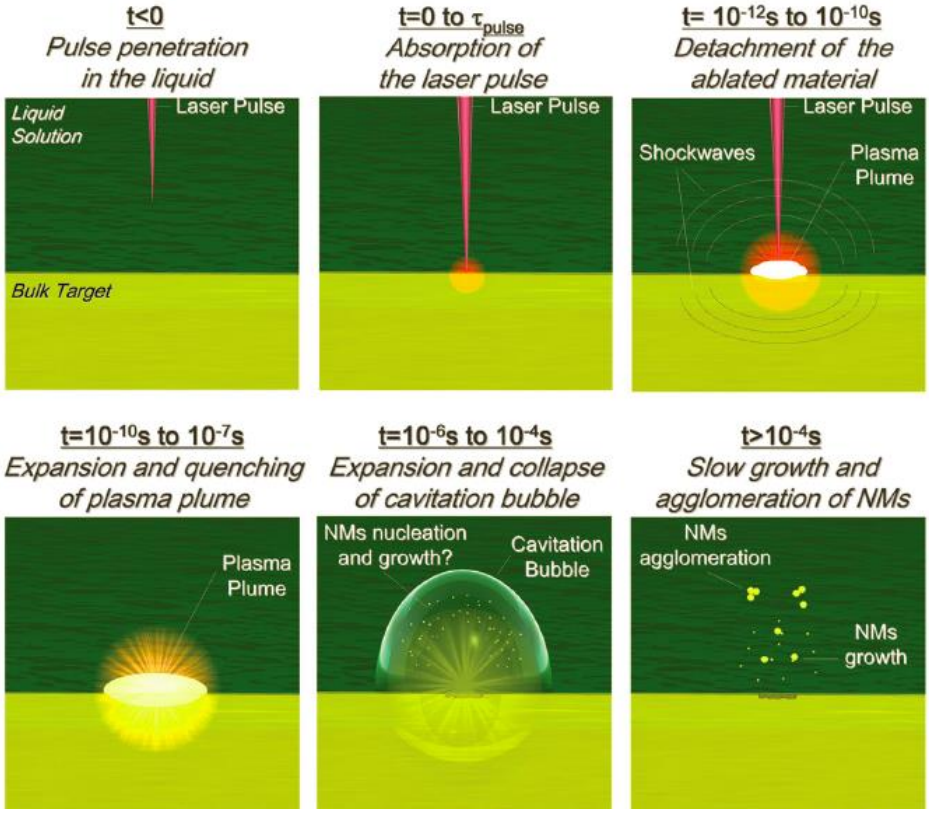

Fig. 1-6 Schematic images of LAL process corresponding to time scale. Data are sited from Amendola *et al.*[37]

1.2.2. LAL sampling for ICPMS measurements

Recently, LAL sampled particles was analyzed by ICPMS for determination of trace elements and isotope ratio analysis.[10] LAL was applied as a new sampling technique for ICPMS measurement. The SEM images of LAL samples under laser fluence of 10 J cm^{-2}, repetition ratio was 20 Hz, scan speed of 10 μm sec^{-1}, and line scanning mode are shown in Fig.1-7. Spherical, agglomerated, and edge-shaped particles were observed in ablated particles. The size of LAL sampled particles were 0.01-5 μm. Although quantitative analysis by means of LAL sampling slurry nebulization ICPMS has been reported, determination data of volatile elements such as As has not been reported.[38] It

might be considered that volatile elements were difficult to measure by means of slurry nebulization ICPMS. Because elemental fractionation occurred when the large size of LAL sampled particles were introduced into the ICP. Therefore, further investigation of LAL sampling was necessary for ICPMS measurements.

In addition, LAL sampling has some advantages for determination of elements in hard-to-digest samples. The ability of microparticulation is expected that hard-to-digest sample becomes decompose easily. That results in, solution nebulization ICPMS after acid digestion is able to determine trace elements with high reliability compared with LA-ICPMS. This technique is good at for analysis of semiconductor materials.

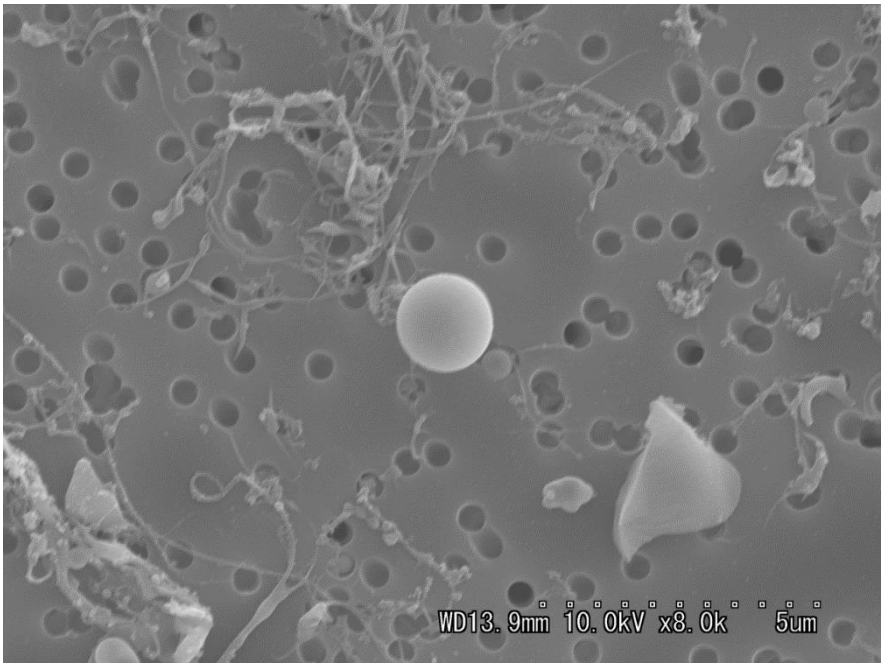

Fig. 1-7 SEM images of LAL sampled particles (NIST 610 glass).

1.3. Silicon carbide (SiC) for semiconductor manufacturing

1.3.1. Power semiconductor device

Power device has been used for multi-stage of power conversion such as rail-way system, industrial motor, uninterruptible power systems, and green vehicle. The inverter which provides optimal electric power is a typical example of a power converter. In general, power device is required higher dielectric withstanding voltage under the off state, small power loss during operation, stability during high-temperature operation, wide safe operating area and high breakdown field, and long-term reliability.

Various Power electronics have been developed such as the metal-oxide-semiconductor field effect transistor (MOSFET), gate turn-off thyristor (GTO), and insulated gate bipolar transistor (IGBT). The existing power devices were almost manufactured on the silicon substrate, silicon power device technology has matured, and those essential limit due to the physical properties of the silicon was worried.

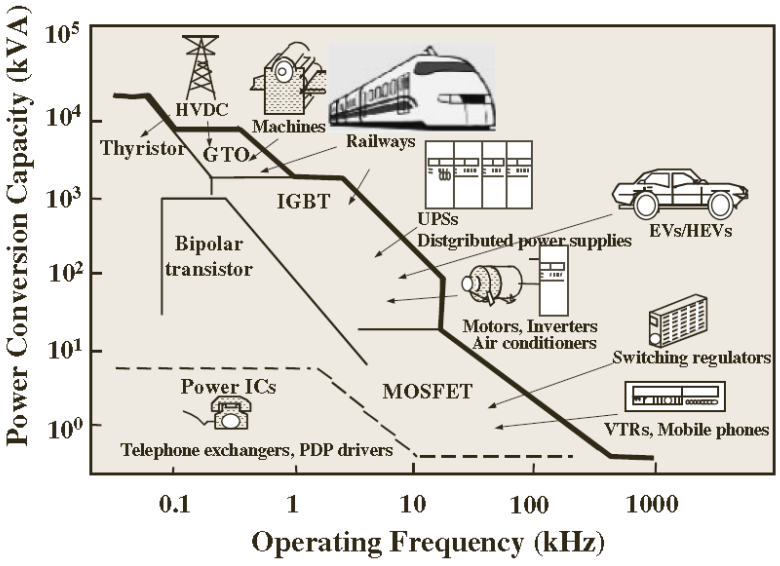

Fig. 1-8 Various application areas of power electronics, where high-efficiency switching devices are used. Data were sited from Okumura et al.[39]

1.3.2. Silicon carbide

Silicon carbide is composed of silicon and carbon. Silicon and carbon are present a lot on the earth, however, crystal of silicon carbide does not exist in the nature. In 19th century, industrial synthesis method of silicon carbide called Acheson method was developed.[40] It was applied to a lot of fields such as abrasive and refractory parts because SiC has properties of hardness (next to diamond), refractoriness and chemical stabilities. A sublimation technique was developed in 1955 as the breakthrough of crystallizing SiC. Since then, application to semiconductor was researched and developed.

The physical properties of SiC, GaN, Si, and GaAs are listed in Table 1-3. Especially, remarkable physical characteristics for power device were the band gap and the breakdown field. [41] The band gap of SiC was about three times higher than that of Si. These excellent properties of SiC are very attractive as power semiconductor. Selective doping of both donor and acceptor impurities can be achieved by ion implantation into SiC. From chemical point of view, SiC is difficult to decompose by acid digestion.[42] Therefore, evaluation for SiC quality has been performed by direct solid analysis and slurry nebulization ICPMS.[43-46]

Table 1-3 Physical properties of SiC, GaN, Si, and GaAs
Data were sited from Matunami et al.[41]

	SiC(4H)	GaN	Si	GaAs
Band gap (eV)	3.26	3.39	1.12	1.43
Electron mobility ($cm^2/V{\cdot}s$)	1000	1000	1350	8000
Breakdown field (MV/cm)	3.0	3.0	0.3	0.4
Saturation drift velocity (cm/s)	2×10^7	2×10^7	1×10^7	1×10^7
Thermal conductivity (W/K·cm)	4.9	1.3	1.5	0.5

1.3.3. Social needs for SiC semiconductor manufacturing

The development of industry and growing world population have proceed with increasing speed since late 20th century. The problem of energy supply has been highlighted in the world. At the same time, there is a need to develop of clean energy and converting technique of power efficiently. Therefore, power device produced by SiC has been expected as a new solution for energy problem.

For development of SiC power divide, crystal growth has been strongly researched for a long time.[40, 41, 47] In the results, micro-pipe free SiC substrate has become commercially available. In the next stage of SiC device development, semiconductor function is made on the surface of SiC substrate. For the semiconductor manufacturing, the surface layer purity was required for reliable semiconductor function. [39] In the case of silicon semiconductor manufacturing, surface layer analysis is performed by means of acid digestion ICPMS. However, it is impossible that the surface layer of SiC materials is analyzed by means of acid digestion ICPMS because SiC is hard-to-digest depending on the crystal types. Surface analysis with high reliability was required for the SiC power device manufacturing.

1.4. Objectives of the doctoral studies

One of the purpose in this study is explanation of how to elemental fractionation occurs in LA-ICPMS. And the other is development of quantitative analysis for hard-to-digest ceramics such as silicon carbide with high reliability. We observed elemental fractionation under defocus conditions, so that we tried to explain the reason why this phenomenon occurred. Ablated particles larger than 2 μm were discussed in Chapter 2. In the next, four fractions of size-classified ablated particles (Dp values of <0.06, 0.06–

0.22, 0.22–2.2, and >2.2 μm) were collected on filters. Collected particles were analyzed and those chemical composition and size distribution were discussed in Chapter 3.

LAL sampling technique was developed in Chapter 4. This technique was also used to evaluate elemental fractionation observed during the LAL and in the ICP separately. To understand the phenomenon that occurs in the LA process, the LAL-sampled particles suspended in the water were divided into two size classes by filtration. The size related fractionation was discussed. LAL-sampled particles were measured by means of slurry nebulization ICPMS for understanding elemental behavior in the ICP.

In the end, sintered SiC and single-crystal SiC were measured by means of both LA-ICPMS and LAL sampling ICPMS in Chapter 5. Single-crystal SiC was analyzed at the first time by using LAL sampling ICPMS.

Chapter 2

Temporal changes of fractionation index explained by changes in the large size of ablated particles

2.1. Introduction

2.2. Experimental

2.2.1. Instrumentation

2.2.2. LA-ICPMS measurement

2.2.3. Particle sampling and SEM observation

2.2.4. Crater shape monitoring

2.3. Results and discussion

2.3.1. Single-site mode

2.2.2. Line-scan mode

2.2.3. Classification of elements

2.4. Summary

Chapter 2 Temporal changes of fractionation index explained by changes in the large size of ablated particles

2.1. Introduction

Laser ablation-inductively coupled plasma mass spectrometry (LA-ICPMS) is an effective sample introduction technique that has been applied to multi-elemental analysis in solids. However, LA-ICPMS suffers from elemental fractionation,[48, 49] a phenomenon in which the elements in a sample are enriched (or depleted) by LA and ICP, depending on the elemental properties. Although interactions between the laser and the sample surface have gradually come to be understood,[48] the underlying causes of elemental fractionation have not been elucidated clearly.

Elemental fractionation can be quantitatively evaluated in terms of the fractionation index (FI). The FI shows how the intensity ratios of elements change in particles generated by the LA; for example, Ca intensity is often used as an internal standard in the case of measuring NIST glasses.[31, 50, 51] Research in recent years has focused on how the wavelength, repetition rate and the pulse width of the laser affect the FI.[9, 21] These studies have suggested that a short wavelength, such as the 193 nm wavelength of an excimer laser, can decrease the amount of elemental fractionation. Short (femtosecond) pulse widths also have been reported to enable stoichiometric, non-thermal ablation and to yield smaller particles than those generated by lasers with longer pulse widths.[22-24]

Fundamental mechanisms of laser ablation, such as vaporization, ionization, and generation of particles, have been studied in efforts to achieve stoichiometric ablation, and ionization mechanisms in ICP also have been investigated.[25-30, 52] It has been reported that when particles generated by LA were introduced into the ICP, mass-load-dependent

matrix effects were caused in LA-ICPMS.[31] Therefore, various quantitative strategies using LA-ICPMS have been developed.[18, 15, 53-55] To better understand the relationship between the elements in ICP, and the number and the size of particles observed in LA-ICPMS, researchers have suggested that internal-standard elements should be chosen with the selection criterion that the LA-ICPMS behavior of these elements be the same as that of the target elements. This information will be useful for quantitative analysis with high accuracy.

In this study, in order to achieve an understanding of the relationship between FI and elemental properties, temporal changes in the FIs of ablated particles were monitored. First, temporal changes in the FIs were studied for a wide range of elements monitored during 10 min of laser ablation using single-site or line-scan mode and under in-focus, 0.5 mm defocus, or 1.0 mm defocus conditions. Second, to measure changes of ablated particles, the ablated particles were collected on a membrane filter, and the number of particles larger than 2 μm as well as the largest particle size for each sample was measured by means of scanning electron microscopy (SEM).

2.2. Experimental

2.2.1. Instrumentation

A laser ablation system (UP213, ESI, Portland, OR) in combination with ICPMS (Agilent 7500ce, Agilent Technologies, Tokyo, Japan) was used in this study. NIST 610 (National Institute of Standards and Technology, Gaithersburg, MD) glass standard material was used to generate samples. NIST 610 contains 61 trace elements each at a concentration of approximately 500 mg kg^{-1}, and its matrix composition is 72% SiO_2, 12% CaO, 14% Na_2O, and 2% Al_2O_3. A large format cell with 6-sq.-in. was used for a laser ablation cell.

To reduce wash-out time, a quartz ring with a volume of approximately 0.8 cm^3 was mounted just above the sample. High purity He gas was flowed into the inlet of the large format cell at 1.0 L min^{-1}. Ablated particles were produced under He atmosphere. Ar gas was admixed with He at a flow rate of 0.8 L min^{-1} after the ablation cell via a Y-shape gas line. Ablated particles were carried by He and Ar gas mixtures into the ICP.

2.2.2. LA-ICPMS measurement

The LA-ICPMS measurement conditions used in this study are summarized in Table 2-1. The LA-ICPMS was tuned so as to provide the highest sensitivity for isotopes of ^{59}Co, ^{139}La, and ^{232}Th by using NIST612 glass standard. The repetition rate (20 Hz) and the diameter crater (100, 60, and 200 μm) were used in this study because these conditions enable large enough signal to detect by LA-ICPMS. The isotopes ^{24}Mg, ^{27}Al, ^{29}Si, ^{42}Ca, ^{45}Sc, ^{49}Ti, ^{52}Cr, ^{55}Mn, ^{59}Co, ^{60}Ni, ^{63}Cu, ^{66}Zn, ^{69}Ga, ^{75}As, ^{82}Se, ^{88}Sr, ^{89}Y, ^{90}Zr, ^{107}Ag, ^{111}Cd, ^{120}Sn, ^{121}Sb, ^{125}Te, ^{137}Ba, ^{140}Ce, ^{157}Gd, ^{173}Yb, ^{178}Hf, ^{184}W, ^{185}Re, ^{208}Pb, ^{209}Bi, ^{232}Th, and ^{238}U were measured using single-site mode and under in-focus, 0.5 mm defocus, and 1.0 mm defocus conditions (Fig. 2-1). In the case of 0.5 mm defocus and 1.0 mm defocus conditions, the laser was defocused by focusing it 0.5 or 1.0 mm beneath the sample surface based on the CCD image. Under 1.5 mm defocus conditions, no signal was observed by LA-ICPMS. So in-focus, 0.5 mm defocus, and 1.0 mm defocus conditions were adopted for understanding trends of defocus conditions. As 34 isotopes were measured with an integration time of 0.05 s, each isotope was measured with an interval of 2 sec. When the focus was changed from in-focus, 0.5 mm defocus, and 1.0 mm defocus, the crater size was changed to 100, 60, and 200 μm, respectively. Therefore, the fluence was also changed to 16, 46, and 4 J cm^{-2} depending on the crater size. In the next,

^{75}As, ^{88}Sr, ^{90}Zr, and ^{42}Ca (as an internal standard) were measured using line-scan mode and under in-focus and 1.0 mm defocus conditions.

Table 2-1 Operating conditions used for laser ablation and ICPMS measurements

Laser model	UP213
Laser type	Nd:YAG
Wavelength	213 nm
Pulse width	4 ns
Ablation mode	Single-site, Line-scan
Repetition rate	20 Hz
Carrier gas	Helium
Carrier gas flow (He)	1.0 L min^{-1}

Laser energy and fluence			
	Laser energy (mJ)	Diameter of crater (μm)	Fluence (J cm^{-2})
Single-site mode			
in-focus	1.3	100	16*
0.5 mm defocus	1.3	60	46*
1.0 mm defocus	1.3	200	4*
Line-scan mode			
in-focus	1.3	100	16
1.0 mm defocus	1.3	200	4

* Asterisk indicates an initial value of fluence. The actual fluence was changed with time.

ICPMS model	Agilent 7500ce
RF power	1600 W
Integration time	0.05 sec
Additional gas flow (Ar)	0.8 L min^{-1}
Collision gas (He)	2 mL min^{-1}
Isotopes measured	^{24}Mg, ^{27}Al, ^{29}Si, ^{42}Ca, ^{45}Sc, ^{49}Ti, ^{52}Cr, ^{55}Mn, ^{59}Co, ^{60}Ni, ^{63}Cu, ^{66}Zn, ^{69}Ga, ^{75}As, ^{82}Se, ^{88}Sr, ^{89}Y, ^{90}Zr, ^{107}Ag, ^{111}Cd, ^{120}Sn, ^{121}Sb, ^{125}Te, ^{137}Ba, ^{140}Ce, ^{157}Gd, ^{173}Yb, ^{178}Hf, ^{184}W, ^{185}Re, ^{208}Pb, ^{209}Bi, ^{232}Th, ^{238}U

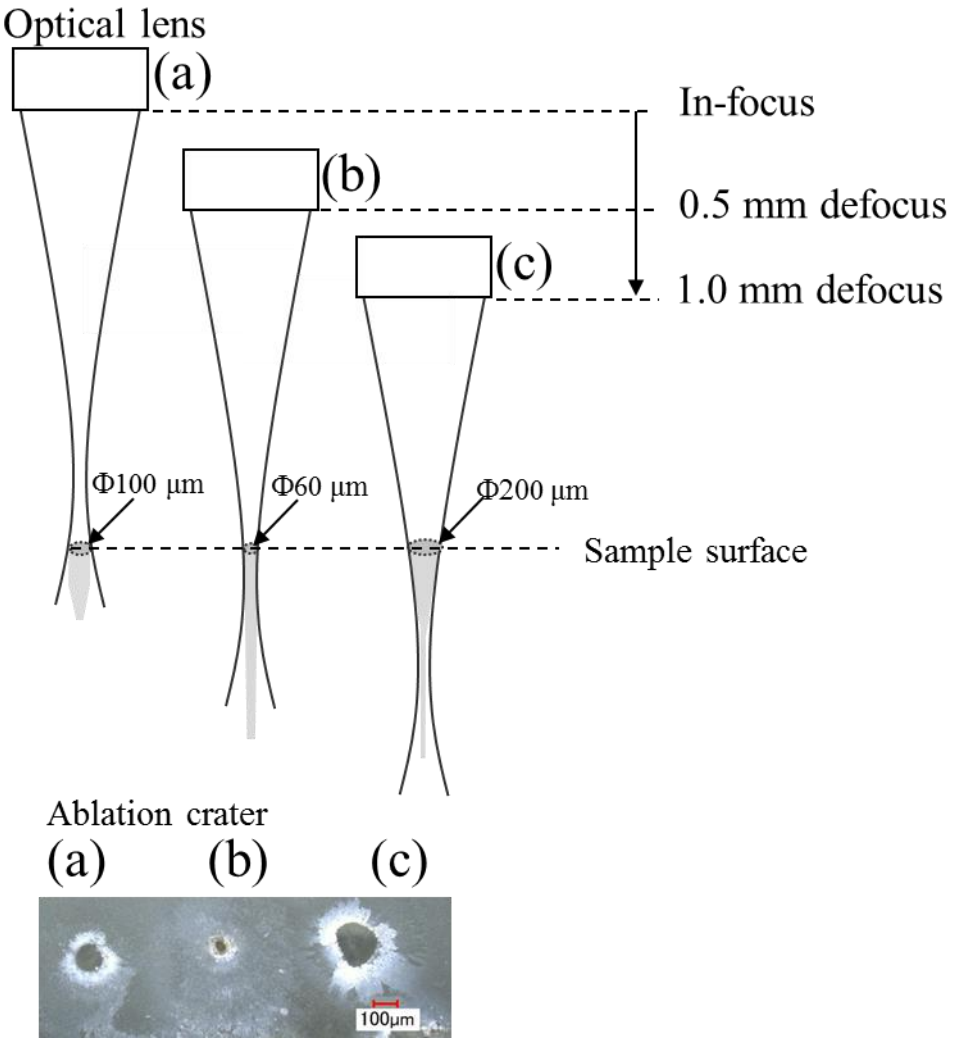

Fig. 2-1 Schematic diagram of the flat-top laser and ablation craters formed under different focus conditions: (a) in-focus, (b) 0.5 mm defocus, and (c) 1.0 mm defocus.

2.2.3. Particle sampling and SEM observation

A schematic diagram of experimental setup for collecting ablated particles is shown in Fig. 2-2. Ablated particles were directly collected on a nitrocellulose membrane filter (pore size: 0.45 μm, diameter: 13 mm, Waters, Milford, MA). The filter was mounted on a syringe filter holder (Millipore, Darmstadt, Germany). The ablated particles in He and Ar gas mixture were sacked from the large format cell at 1.8 L min^{-1} by means of a diaphragm pump (FTP-10B, KNF, Tokyo, Japan) equipped with a mass flow controller (Azbil Co., Tokyo, Japan). An NIST 610 glass was ablated using either single-site mode or line-scan mode during 10 min. In order to collect the ablated particles every minute, T-shape valves were used to switch two filter holders every minute. The filter was replaced every minute.

A scanning electron microscope (SEM; S-4300, Hitachi High Technologies, Tokyo, Japan) was performed to observe the number and the size of ablated particles. The filter surface was coated with a Pt/Pd alloy by ion sputtering (E-1045, Hitachi High Technologies, Tokyo, Japan). The largest three ablated particles were searched from all over the filter surface and SEM images of a rectangular area of 500 μm by 380 μm were obtained around the largest particle with a magnification of 250.

The number and the size of ablated particles were measured by counting the particles with diameters of larger than 2 μm and also by noting the largest-size particle observed in the rectangular area of 500 μm by 380 μm. Ablated particles with diameters larger than 2 μm were counted as a particle clearly. Spherical, agglomerated, and edge-shaped particles were observed in ablated particles less than 2 μm. Edge-shaped particles were mainly observed in ablated particles larger than 2 μm.

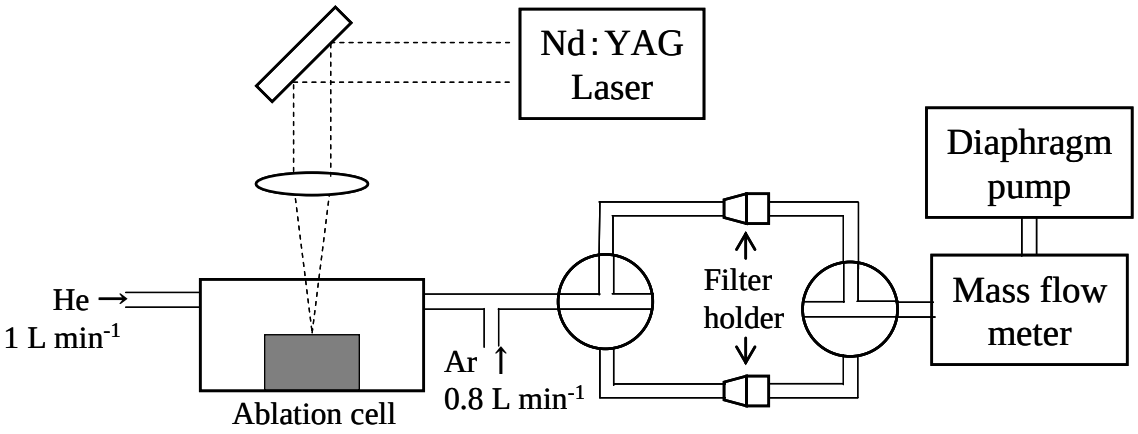

Fig. 2-2 Schematic diagram of experimental setup to collect ablated particles at 1-min intervals on two filters alternatively.

2.2.4. Crater shape monitoring

Detailed examination of the crater size and depth has been carried out using an optical microscope (VHX-2000, Keyence, Osaka, Japan). Crater size and depth were measured by observation of sample surface and side, respectively, after laser irradiation. The drilling rate of laser ablation was determined by measuring the depths of craters created by laser ablation every minute.

2.3. Results and discussion

2.3.1. Single-site mode

Using single-site mode and under in-focus, 0.5 mm defocus, and 1.0 mm defocus conditions, the elemental intensities of As, Ca, Sr, and Zn were measured by means of

time-resolved analysis. Under in-focus, 0.5 mm defocus, and 1.0 mm defocus conditions, the fluences were 16, 46, and 4 J cm^{-2}, respectively, depending on the crater size (Fig. 2-1), while the laser energy was fixed at 1.3 mJ. The signal intensities of As, Sr, and Zr as a function of ablation time are shown in Fig. 2-3a. For this set of experiments, As, Sr, and Zr were selected as typical elements, in accordance with the classification of elements described in the later chapter of "*2.2.3.Classification of elements*".

For laser ablation using single-site mode under 16, 46, and 4 J cm^{-2} fluences, the signal intensities of all measured elements decreased with time because increasing the depth of the crater pit made it difficult for the ablated particles to fly out from the crater pit, and the drilling amount decreased with an increase in the depth of the pit. From Fig. 2-3a, the FI was calculated from the following Eq. (2-1):

$$FI = \frac{\Sigma \text{ cps } (M_{\Delta 1 \text{ min}}) / \Sigma \text{ cps } (Ca_{\Delta 1 \text{ min}})}{\Sigma \text{ cps } (M_{0\text{-}1 \text{ min}}) / \Sigma \text{ cps } (Ca_{0\text{-}1 \text{ min}})} \qquad (2\text{-}1)$$

where cps ($M_{\Delta 1 \text{ min}}$) and cps ($Ca_{\Delta 1 \text{ min}}$) are the signal intensities of an element and Ca, respectively, observed every minute during the 10-min ablation period; and cps ($M_{0\text{-}1 \text{ min}}$) and cps ($Ca_{0\text{-}1 \text{ min}}$) are the signal intensities of the element and Ca, respectively, observed during only the first minute of ablation. The FIs of As, Sr, and Zr as a function of ablation time are shown in Fig. 2-3b. LA-ICPMS measurements and calculation of the FIs were repeated three times and an error bar of FIs is shown in Fig. 2-3 b.

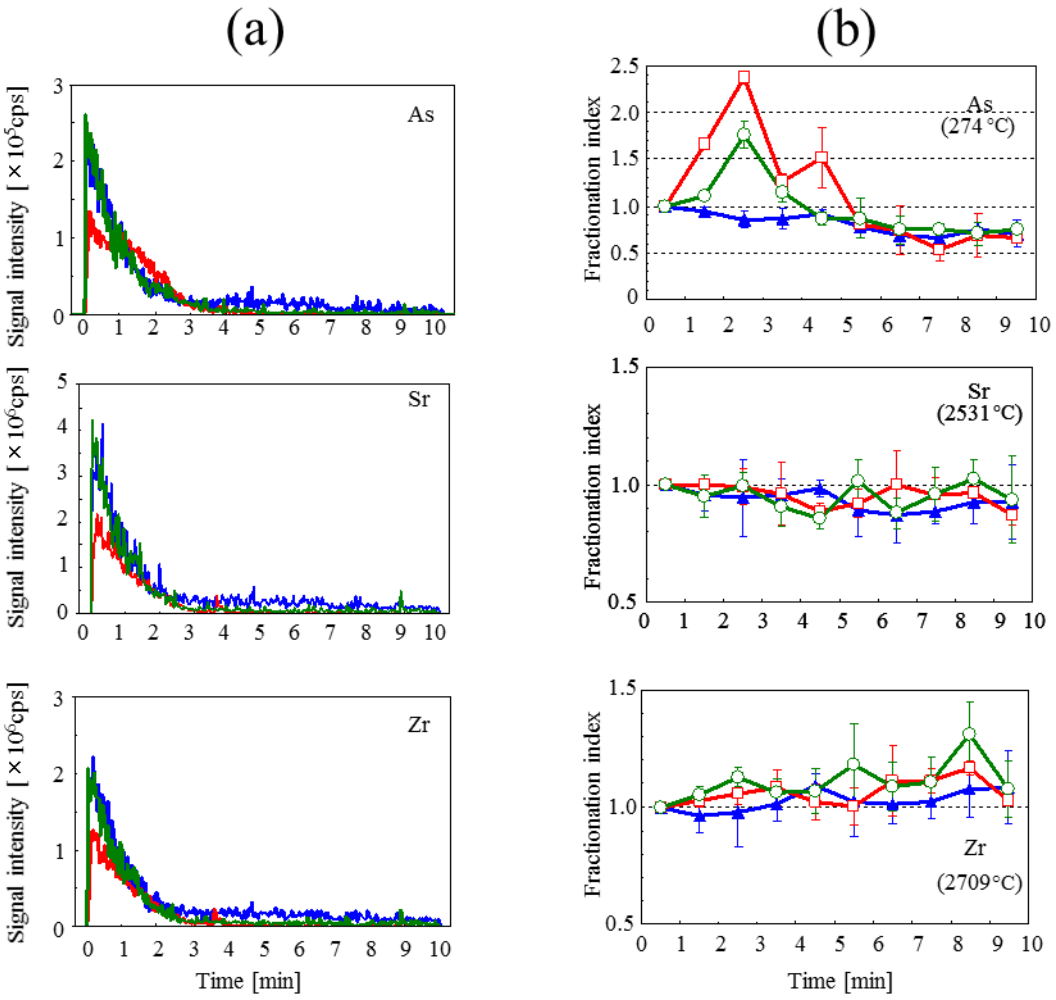

Fig. 2-3 (a) Signal intensities for As, Sr, and Zr obtained by LA-ICPMS. Laser ablation was performed using single-site ablation mode and under different focus conditions. ▬ in-focus with 16 J cm^{-2}, ▬ 0.5 mm defocus with 46 J cm^{-2}, ▬ 1.0 mm defocus with 4 J cm^{-2}, (b) The FIs of As, Sr, and Zr during ablation for 10 min. -▲- in-focus with 16 J cm^{-2}, -□- 0.5 mm defocus with 8 J cm^{-2}, -○- 1.0 mm defocus with 4 J cm^{-2}. The temperature in parentheses indicates the melting point of each element's corresponding metal oxide.

In the case of in-focus conditions, for As, the FIs decreased to 0.7 at 10 min. In contrast, the FIs for Sr and Zr remained mostly constant during the 10-min ablation process. The FIs of As increased to 2.4 at 3 min under 0.5 mm defocus conditions and increased to 1.8 at 3 min under 1.0 mm defocus conditions; the FIs then decreased under both defocus conditions. For Sr, the FIs under defocus conditions exhibited the same trends as those observed under in-focus conditions. The FIs of Zr increased slightly to 1.1 under 0.5 mm defocus and 1.0 mm defocus conditions.

We concluded that the differences in FI observed for these three elements were likely related to differences in their elemental properties, including melting point and boiling point. For example, As is more volatile than the reference Ca, whereas the elemental properties of Sr are similar to those of Ca, which probably explains why the FIs for Sr remained mostly constant during ablation. Elements with high melting and boiling points, such as Zr, probably were difficult to vaporize in the ICP during the first minute of ablation before becoming more efficiently vaporized with increasing time, thus explaining the observed FIs behavior for Zr.

Guillong et al.[7] and Guillong and Günther[29] reported that the excitation process within the ICP, such as vaporization, atomization, and ionization, was influenced by the size of ablated particles. Therefore, we assumed that the temporal changes of FIs observed in this study were related to the size of ablated particles. In order to investigate the possible effect of temporal changes in particle size on the observed FIs, we acquired SEM images of the particles generated by laser ablation. The particles generated by laser ablation were collected on a filter every minute. SEM images of the laser ablated particles under in-focus conditions (each image is a rectangular area of 500 μm by 380 μm) are shown on the left side of Fig. 2-4. Regions of interest in these images (red boxes in Fig.

2-4, left) were magnified 10× to acquire additional SEM images (Fig. 2-4, right). These images clearly show that the number of particles collected on the filter decreased and that the particle size also decreased with increasing ablation time.

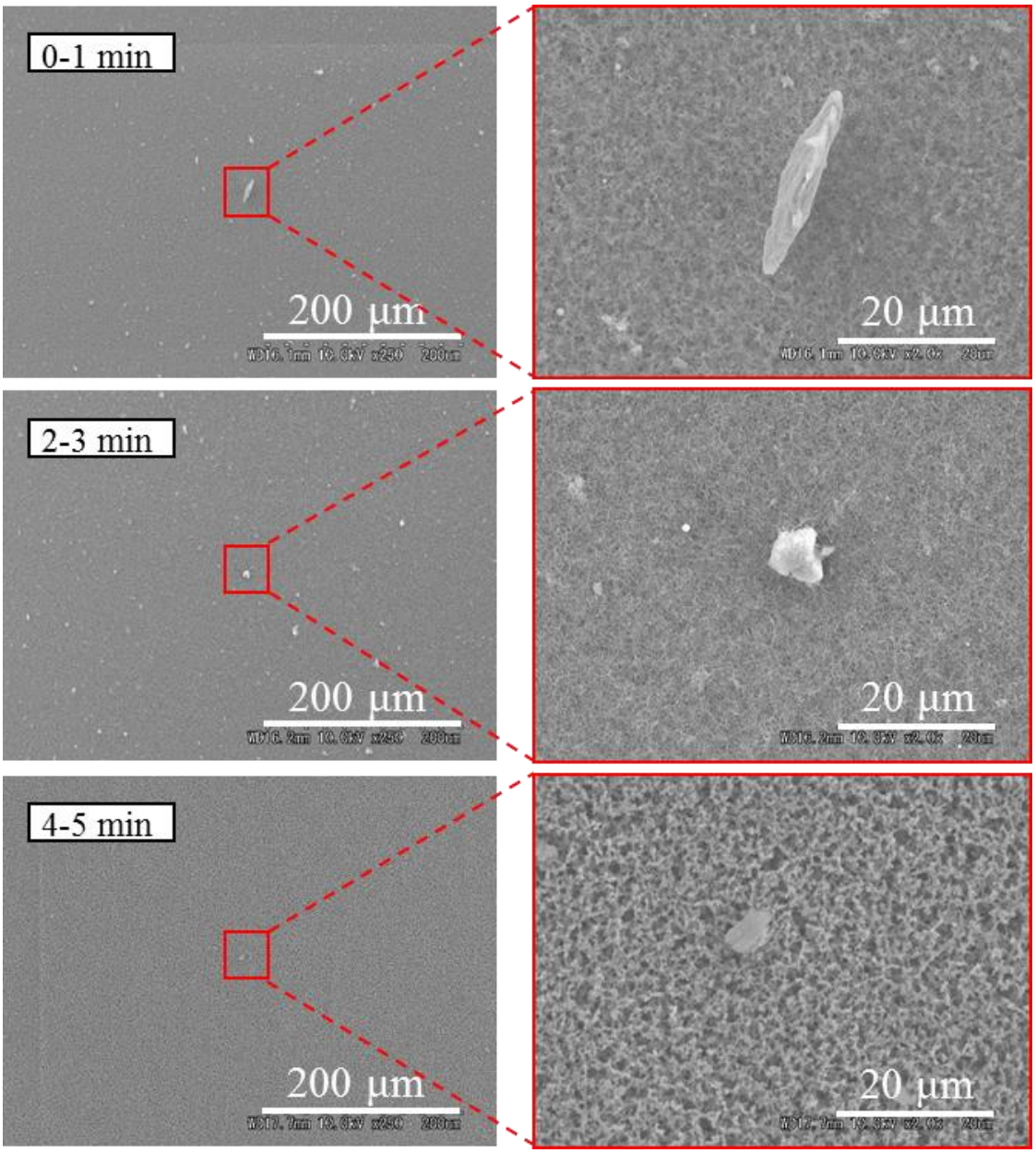

Fig. 2-4 SEM images of particles collected at 1-min intervals during laser ablation using single-site mode and under in-focus conditions with 16 J cm^{-2}.

The number of particles larger than 2 μm, as well as the largest particle observed, were recorded for each SEM-imaged rectangular area. The number of particles and the diameter of the largest particle are shown in Figs. 2-5a- 2-5c. SEM image measurements at 5-6, 7-8, and 9-10 min did not show any remarkable change.

Under in-focus conditions, we observed an average of 184 ± 5 particles larger than 2 μm at 0-1 min. The diameter of the largest particle observed in this set of images was 14.0 ± 10.2 μm. The number of particles larger than 2 μm and the diameter of the largest particle observed decreased with increasing ablation time. After 8-9 min, only 3 ± 3 particles larger than 2 μm were observed, and the diameter of the largest particle was 3.9 ± 0.7 μm.

To explain these observed decreases in particle size, we again considered differences in elemental properties among the elements. Arsenic was ionized more easily than Ca, because As oxide has a much lower melting point (274°C) than Ca oxide (2570°C). The generation of smaller particles increased after 1 min ablation, and then the Ca in these particles was easily ionized in the ICP. As the size of the ablated particles decreased, the rate of ionization of Ca increased relative to that of As. In contrast, the FIs of Sr remained constant with time, because Sr, an alkaline earth metal like Ca, has an oxide melting point (2531°C) similar to that of Ca oxide. The melting point of Zr oxide (2709°C) is higher than that of Ca oxide (2570°C), and therefore Zr was more difficult to vaporize in the ICP than Ca. This difference between melting points of Zr oxide and Ca oxide exerted the largest influence on particles larger than 2 μm. With increasing ablation time, the diameter of the ablated particles became smaller, and that induced that vaporization efficiency of refractory elements was improved more than that of Ca. Therefore, the FIs of Zr slightly increased with ablation time.

Volatile elements in the particles were easily vaporized in the ICP regardless of particle size. Refractory elements such as Zr in particles were difficult to vaporize in the ICP, however these elements became easy to vaporize with decreasing particle size. We concluded that this particle-size-dependent vaporization was one of the mechanisms that contributed to the observed differences in elemental fractionation.

In the case of 1.0 mm defocus conditions with 4 J cm^{-2}, as shown in Fig. 2-5c, the largest particle observed on filters collected at 1-2, 2-3, 3-4, and 4-5 min were larger than those collected at 0-1 min, in contrast to the particle-size trend observed for particles collected under in-focus conditions (Fig. 2-5a). The diameter of the largest particles collected at 1-2, 2-3, and 3-4 min under 0.5 mm defocus conditions were also larger than those collected at 0-1 min (Fig. 2-5b).

The signal intensity and the FIs of As (shown in Fig. 2-3) as a function of crater depth is shown in Fig. 2-6a. The crater depth observed every minute and a microscope image of the crater after 10 min ablation under 1.0 mm defocus conditions are shown in Figs. 2-6b and 2-6c, respectively. In the case of defocus conditions, actual laser fluence increased due to crater size decrease as the ablation process progressed. The higher fluence can induce larger shockwave, and then produced large edge-shaped particles at the depth of 410-520 μm. As the result, the maximum value of the FI was observed at 2-3 min (Fig. 2-3). The aspect ratio of 2-2.6 was calculated from the crater size and the depth created during 2-3 min ablation process.

For explanation of the observed increase in the FIs for As, we presumed that Ca became difficult to ionize as the diameter of particles increased with increasing ablation time up to 5 min. The FIs of As decreased below 1.0 after 5 min because the particles collected after 5 min were smaller than the particles collected at 0-1 min under both 0.5

and 1.0 mm defocus conditions. In this study, particles more than 2 μm were counted by using SEM, however there was a possibility that the relative number of particles less than 2 μm might increase as the ablation process progressed. Koch et al.[56] indicated that using femtosecond LA at fluence of <5 J cm^{-2} and generating ultra-fine aerosols (mean diameter ≈ 10 nm) led to decrease of elemental fractionation. The volume of particles with diameter of 2 μm (4×10^{-12} cm^3) is 8×10^6 times larger than that of 10 nm (5×10^{-19} cm^3). Consequently, the signal intensity within the ICP was affected by the large ablated particles. Therefore, the temporal changes in the number and the large ablated particles were one of reasons of elemental fractionation. The FIs of Sr remained constant regardless of the ablated particles' number and the largest size of them. The FIs of Zr slightly increased as the number of particles larger than 2 μm decreased. As mentioned above, there might be the relative number of particles less than 2 μm increase as the ablation process progressed.

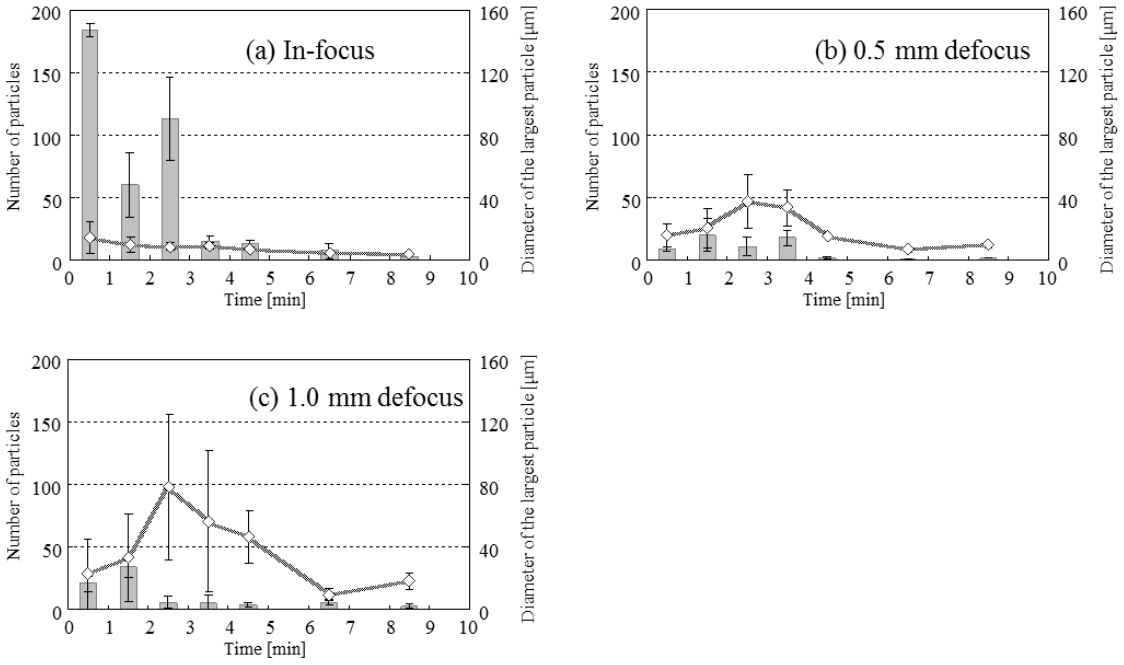

Fig. 2-5 The number of particles larger than 2 μm and the diameter of the largest particle observed in SEM images of laser-ablated particles obtained under single-site mode and in-focus, 0.5 mm defocus, and 1.0 mm defocus conditions. ■; Number of particles, ◇; Diameter of the largest particle. Error bars indicate standard deviation (n=3).

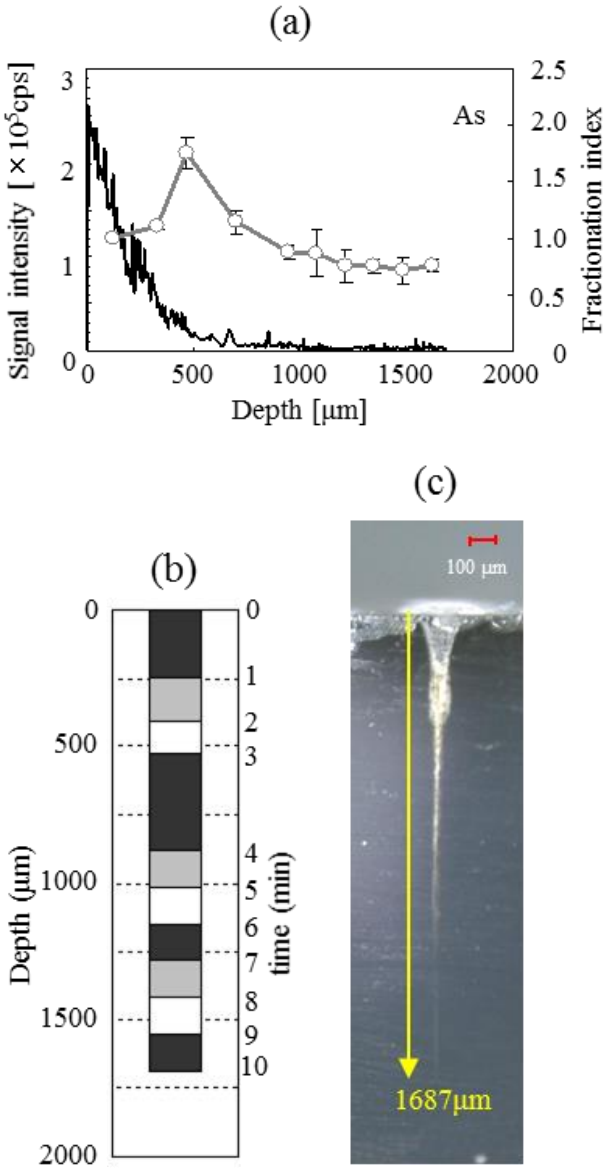

Fig. 2-6 (a) Signal intensities and FIs of As obtained by LA-ICPMS. Laser ablation was performed using single-site ablation mode and under 1 mm defocus conditions. ━ signal intensities, -○- FIs. (b) The crater depth observed every minute. (c) A microscope image of crater after 10 min ablation under 1.0 mm defocus conditions.

2.2.2. Line-scan mode

Using line-scan mode and under in-focus and 1.0 mm defocus conditions, the elemental intensities of As, Sr, and Zr were measured. The signal intensities of As, Sr, and Zr as a function of ablation time are shown in Fig. 2-7a. The FIs were calculated from the intensity data and plotted in Fig. 2-7b. When the line-scan mode was employed, the FIs of all elements was constant under both in-focus and 1.0 mm defocus conditions. SEM images of particles ablated using line-scan mode and under in-focus conditions at 0-1 and 4-5 min are shown in Fig. 2-8a. These particle sizes observed in these SEM images are similar to those observed at 0-1 min using single-site mode (Fig. 2-4).

The number of particles larger than 2 μm and the diameter of the largest particle observed within a rectangular area of 500 μm by 380 μm are shown in Fig. 2-8b. The diameter of the largest particle observed using line-scan mode was larger than that observed at 0-1 min using single-site mode, and the aspect ratio using line-scan mode was smaller than that of using single-site mode. These effects helped that the signal intensity was larger using line-scan mode. The number of particles and the diameter of the largest particle did not change during the ablation process. This result most likely occurred because the interaction between the laser and the sample surface would have remained nearly constant throughout the line-scan mode ablation, because the laser would have been continually scanning over unablated areas of the sample; in contrast, in single-site mode ablation the same point on the sample surface is ablated continuously, which caused the laser-sample interactions to fluctuate during ablation.

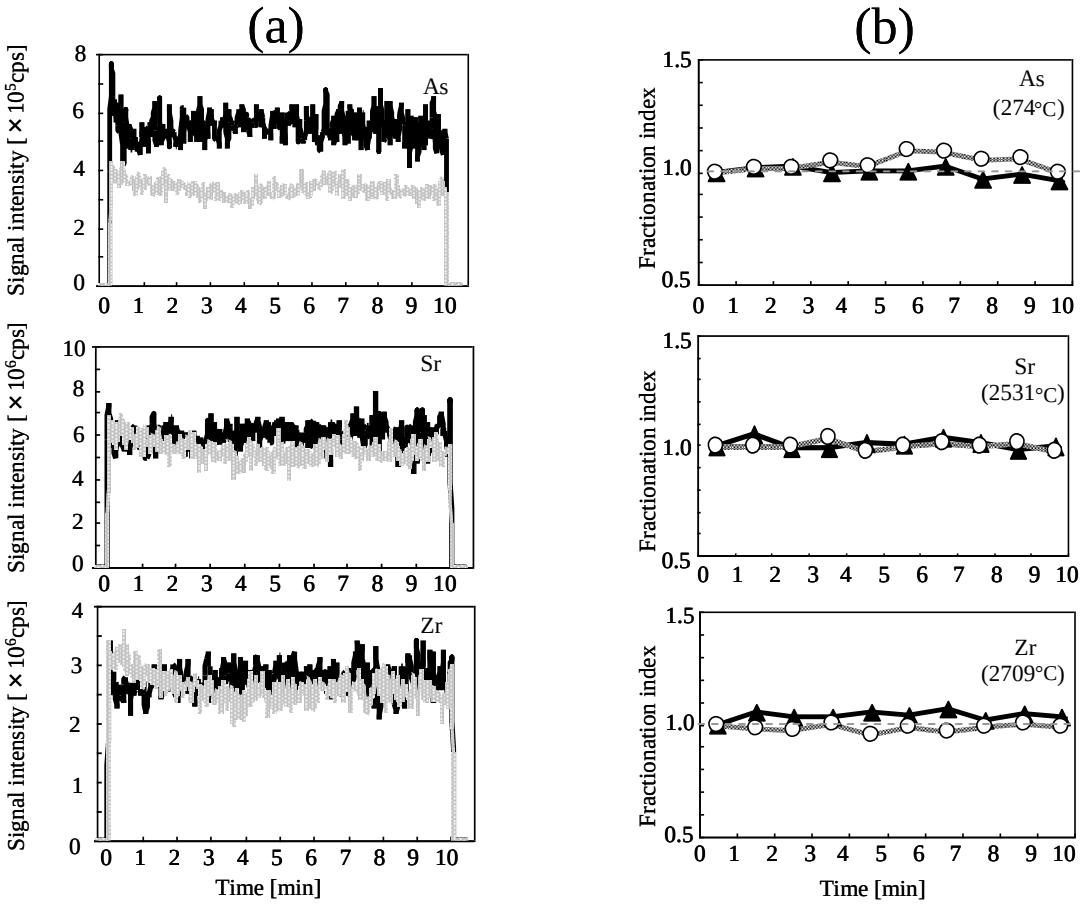

Fig. 2-7 (a) Signal intensities of As, Sr, and Zr obtained by ICPMS. Laser ablation was performed using line-scan mode and under in-focus and 1.0 mm defocus conditions. ▬ in-focus with 16 J cm^{-2}, ▬ 1.0 mm defocus with 4 J cm^{-2} (b) FIs of As, Sr, and Zr during ablation for 10 min. The temperature in parentheses indicates each element's corresponding metal oxide. -▲- in-focus with 16 J cm^{-2}, -○- 1.0 mm defocus with 4 J cm^{-2}.

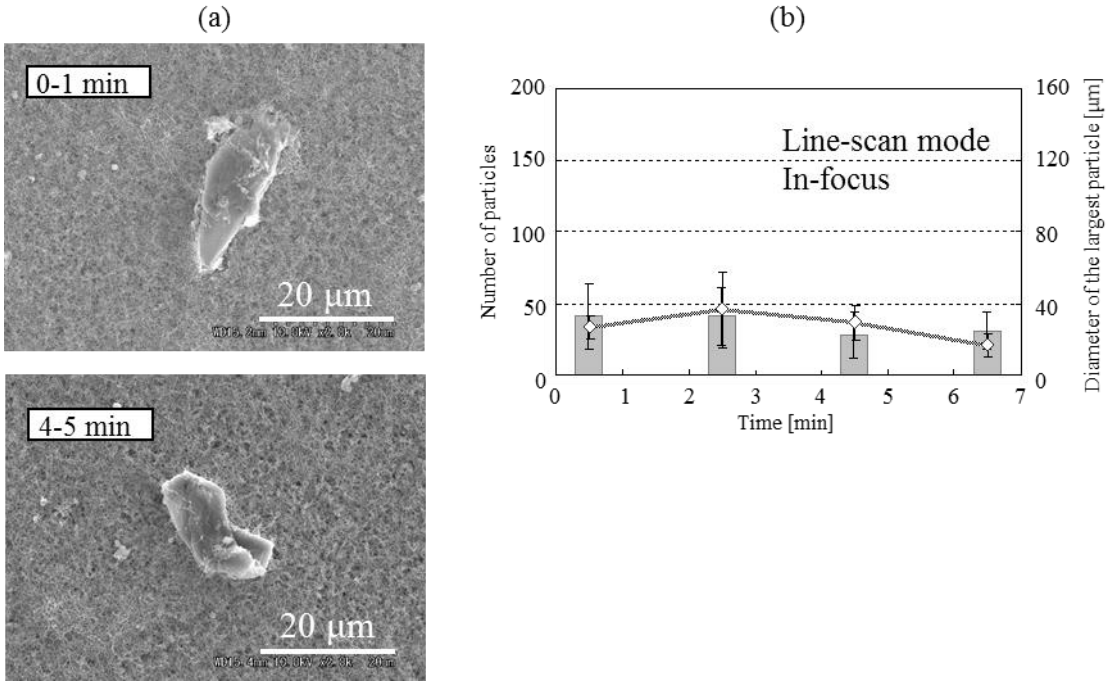

Fig. 2-8 SEM images of particles (a) and the number of particles larger than 2 μm and the diameter of the largest particle (b) collected at 1-min intervals during laser ablation using line-scan mode and under in-focus conditions with 16 J cm^{-2}. ■; Number of particles, ◇; Diameter of the largest particle. Error bars indicate standard deviation (n=3).

2.2.3. Classification of elements

The FIs behavior of 34 elements in NIST 610 (which contains 65 elements total, including its matrix components) was measured using single-site mode and under 1.0 mm defocus conditions (Figs. 2-9 and 2-10). Each of the elements was classified into two groups in accordance with their observed temporal changes in FIs. The classification of the elements, values of FI (during 2-3 min), along with the melting, boiling points of metal oxides, bond dissociation energy (BDE), and boiling point of atomic elements25 are listed in Table 2-2. The elements Ag, As, Se, Sb, Ga, Te, Bi, Pb, Cd, Re, Sn, Cu, W, and Zn were classified in Group 1, because FI values (2-3 min) of these were larger than over 1.20. The elements Si, Co, Mn, Ti, Ni, Ba, Al, Ce, Cr, Gd, Yb, Y, Sc, Sr, Ca, Zr, Hf, Mg, U, and Th were classified in Group 2 because FI values (2-3 min) of these were within 1 ± 0.15.

As shown in Fig. 2-9, the FIs of Ag, As, Se, Sb, Ga, Te, Bi, Pb, Cd, Re, Sn, Cu, W, and Zn showed an increasing trend until 3 min of laser ablation, at which point the FIs decreased for each of these elements, in a similar manner to that observed for As (Fig. 2-3). The FIs of these elements exceeded 1 when particles larger than those observed at 0-1 min of ablation were introduced into the ICP, and fell below 1 when particles smaller than those observed at 0-1 min of ablation were introduced into the ICP. The melting points of all metal oxides in Group 1 are lower than that of Ca oxide (Table 2-2). Of all the Group 1 elements, Zn oxide has the highest melting point, but because this boiling point of Zn atom is lower than that of elements classed in Group 2. Zinc exhibited FIs trends similar to those of the other elements in Group 1.

As shown in Fig. 2-10, the FIs of Si, Co, Mn, Ti, Ni, Ba, Al, Ce, Cr, Gd, Yb, Y, Sc, Sr, Ca, Zr, Hf, Mg, U, and Th remained nearly constant throughout the 10-min ablation

process, similar to the behavior observed for Sr and Zr (Fig. 2-3). The FIs of these elements were constant regardless of changes in the large ablated particles, because these elements behaved similarly to Ca in the ICP. Therefore, these elements were classified into Group 2. Most of the oxides in Group 2 have higher melting points than those in Group 1.

In summary, classification of these elements from temporal changes in their FIs during laser ablation using single-site mode under 1.0 mm defocus conditions enabled us to identify trends in the behavior of the elements in the ICP. Elemental fractionation was caused by large particles introduced into the ICP when fluence increased using single-site ablation mode. Under 1.0 mm defocus conditions, this phenomenon occurred when fluence increased at the depth of 410-520 μm. It is noticed that an appropriate selection of internal-standard element and control of laser fluence are necessary depending on the sample.

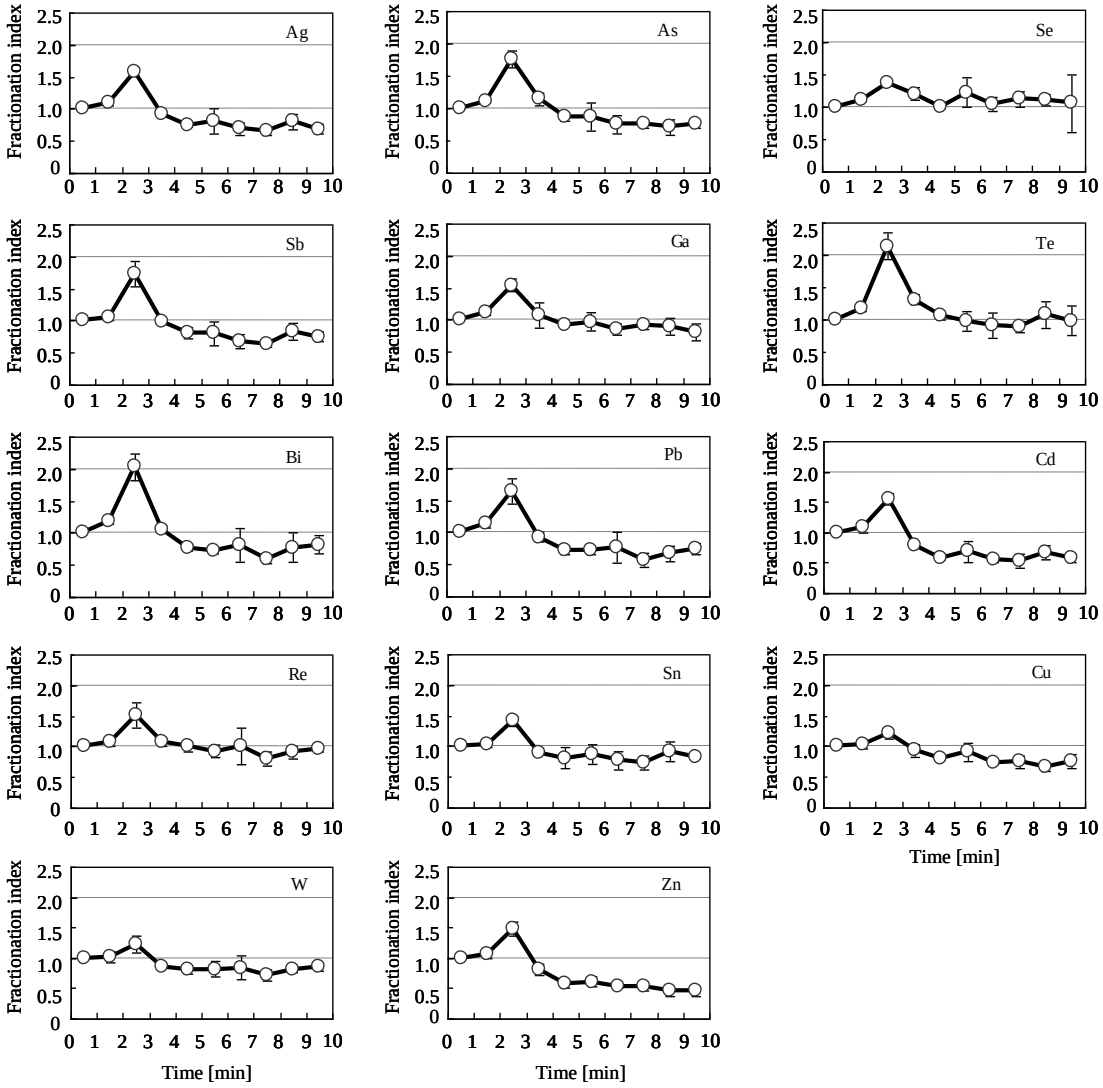

Fig. 2-9 Temporal changes in FIs of Ag, As, Se, Sb, Ga, Te, Bi, Pb, Cd, Re, Sn, Cu, W, and Zn during laser ablation using single-site mode and under 1.0 mm defocus conditions with 4 J cm^{-2}. These elements were classified into Group 1.

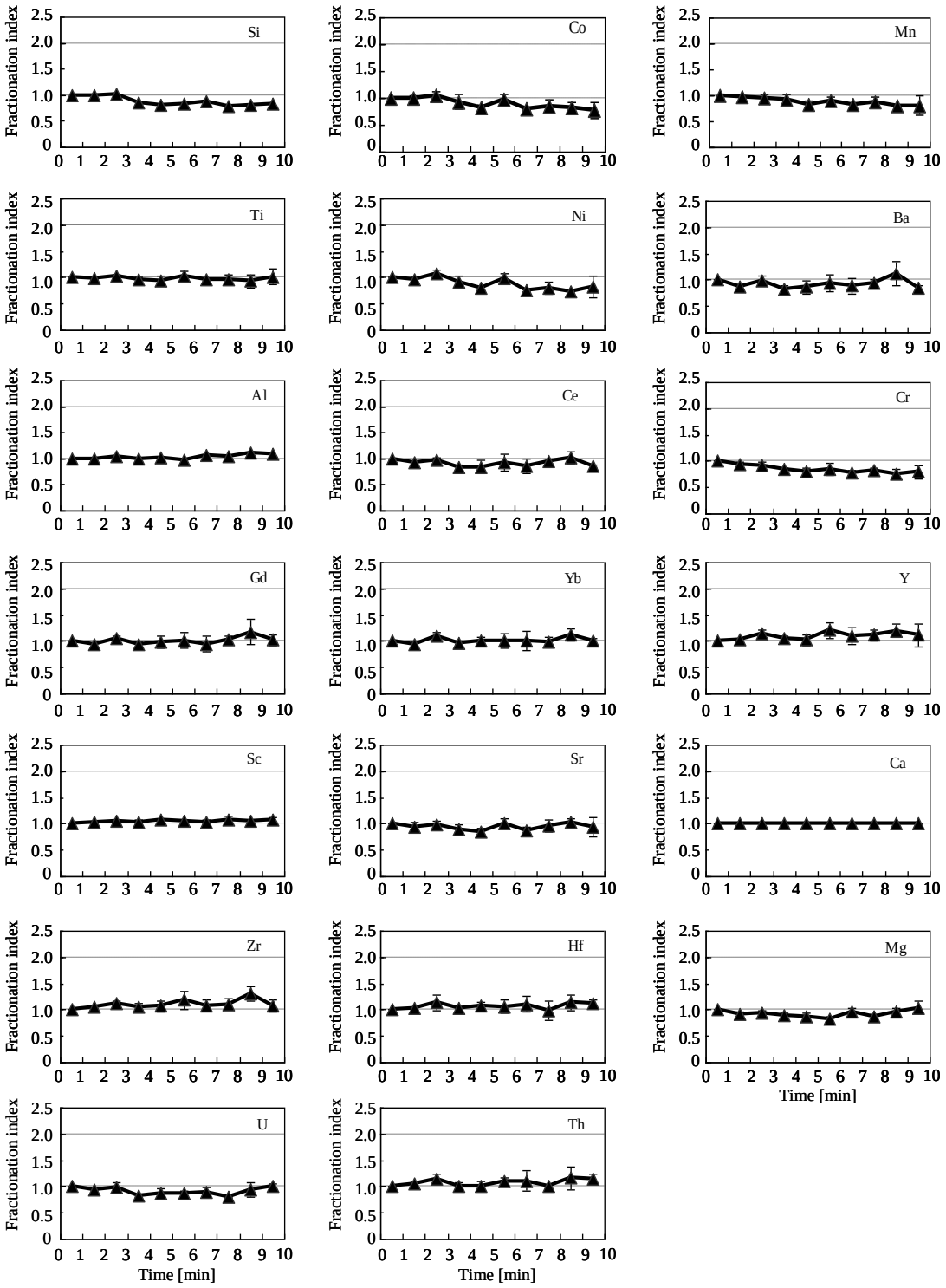

Fig. 2-10 Temporal changes in FIs of Si, Co, Mn, Ti, Ni, Ba, Al, Ce, Cr, Gd, Yb, Y, Sc, Sr, Ca, Zr, Hf, Mg, U, and Th during laser ablation using single-site mode and under 1.0 mm defocus conditions with 4 J cm^{-2}. These elements were classified into Group 2.

Table 2-2 Classification of 34 elements depending on their observed temporal changes in FIs along with their melting point (mp), boiling point (bp), and bond dissociation energy (BDE).[57]

Element	Group	FI	Oxide				Atom
		2-3 min	compound	m.p. [ºC]	b.p. [ºC]	BDE [kJ/mol]	b.p. [ºC]
Ag	1	1.58	Ag_2O	200	–	221	2162
As	1	1.76	As_2O_3	274	460	484	603
Se	1	1.38	SeO_2	340	–	469	685
Sb	1	1.73	Sb_2O_3	570	1425	434	1587
Ga	1	1.54	Ga_2O	660	800	374	2204
Te	1	2.14	TeO_2	733	1245	377	988
Bi	1	2.03	Bi_2O_3	817	1990	337	1564
Pb	1	1.64	PbO	897	–	238	1749
Re	1	1.52	ReO_2	900	–	627	5596
Sn	1	1.41	SnO	1080	–	528	2602
Cu	1	1.20	Cu_2O	1235	1800	281	2562
W	1	1.23	WO_2	1500	–	832	5555
Cd	1	1.54	CdO	>1500	1559	236	767
Zn	1	1.49	ZnO	1974	–	226	907
Si	2	1.01	SiO_2	1722	2950	800	3265
Co	2	1.04	CoO	1830	–	385	2927
Mn	2	0.96	MnO	1839	–	362	2061
Ti	2	1.03	TiO_2	1843	2900	668	3287
Ni	2	1.07	NiO	1955	–	366	2913
Ba	2	0.99	BaO	1972	–	562	1897
Al	2	1.04	Al_2O_3	2053	3000	502	2519
Ce	2	0.98	Ce_2O_3	2210	3730	790	3443
Cr	2	0.92	Cr_2O_3	2329	3000	461	2671
Gd	2	1.06	Gd_2O_3	2339	3900	715	3273
Yb	2	1.10	Yb_2O_3	2355	4070	401	1196
Y	2	1.14	Y_2O_3	2438	–	698	3345
Sc	2	1.06	Sc_2O_3	2485	–	671	2836
Sr	2	1.00	SrO	2531	–	426	1382
Ca	2	1.00	CaO	2570	2850	383	1484
Zr	2	1.13	ZrO_2	2709	4300	766	4409
Hf	2	1.14	HfO_2	2774	–	801	4603
Mg	2	0.94	MgO	2825	3600	358	1090
U	2	0.99	UO_2	2827	–	755	4131
Th	2	1.15	ThO_2	3390	4400	877	4788

2.4. Summary

In this study, we measured temporal changes in the FIs of ablated particles during 10 min of laser ablation under in-focus, 0.5 mm defocus, and 1.0 mm defocus conditions. In the case of volatile elements (Group 1), a remarkable peak of FI was observed at 2-3 min under 0.5 and 1.0 mm defocus conditions. The particles that were produced at 2-3 min were observed by SEM. The large particles more than 2 μm were monitored by SEM. It was considered that the large edge-shaped particles were produced by shockwave which was induced by an increase of fluence as the ablation process progressed. We assumed that the temporal changes of FIs were caused by the large particles more than 2 μm which were related to an increase of fluence. Although, there is a possibility that the FIs were affected by particles less than 2 μm. For further investigations, we need to focus on particle size distribution and chemical composition of fine particles.

We are now proceeding with these experiments. Temporal changes in FIs were explained by elemental behavior due to changes in the large size of ablated particles introduced into the ICP. The FIs indicated how the signal ratio of a given pair of elements (i.e., a sample element and a Ca standard) in the particles generated by laser ablation changed upon introduction to the ICP. In addition, comprehensive evaluation of the particle number and the size by SEM observation and of temporal changes in the FIs helped to further elucidate elemental behavior in the ICP. The results of these experiments were used to classify the elements into two groups. The elements that were classified according to temporal changes in their FIs behaved differently from one another according to changes in the large ablated particles. Therefore, we concluded that changes in the large size of ablated particles are one of the main causes for elemental fractionation. To control the influence of ablated-particle size on LA-ICPMS analysis, a certified

reference material with a matrix similar to that of the sample should be used for calibration. However, such certified reference materials are not always available. In the case of glass sample analysis, the results of this work should be helpful.

Selection of an appropriate internal-standard element is important to obtain accurate LA-ICPMS measurements. On the basis of our findings in this study, we recommend that an internal standard element be chosen from the same group in Table 2-2 as the target element because the relative signal intensities of these elements in LA-ICPMS should remain similar even if the number and the size of particles change over time. We also found that laser ablation using line-scan mode provided a means to stabilize the number and the size of ablated particles and minimize changes therein.

Chapter 3

Temporal changes of size distribution of mass and relative intensity

3.1. Introduction

3.2. Experimental

3.2.1. Instrumentation

3.2.2. Reagents

3.2.3. Collection of size-classified ablated particles with a low-pressure impactor

3.2.4. Acid digestion

3.3. Results and discussion

3.3.1. Fractionation index obtained by means of LA-ICPMS with a cascade impactor

3.2.2. Mass of size-classified ablated particles collected with a low-pressure impactor

3.2.3. Chemical composition of size-classified ablated particles

3.4. Summary

Chapter 3 Temporal changes of size distribution of mass and relative intensity

3.1. Introduction

Laser ablation–inductively coupled plasma mass spectrometry (LA-ICPMS) is an effective technique for multielemental analysis of solid samples. However, LA-ICPMS suffers from elemental fractionation, whereby elements in a sample are enriched (or depleted) during the laser ablation process and in the plasma, to an extent that depends on the elemental properties.[58, 59] The fractionation mechanism has not been definitively elucidated.[22-24] Elemental fractionation can be quantified in terms of the fractionation index (FI).[31, 51, 60] Temporal changes of FIs were investigated under laser defocus conditions. When laser ablation was performed under defocus conditions, a large variation of the diameter of ablated particles was observed. It was a useful technique for understanding relationship between temporal changes of FIs and the size of ablated particles. We previously reported that temporal changes in FIs are caused by changes in elemental behavior resulting from changes in ablated particles with aerodynamic diameters (Dp) larger than 2.0 μm introduced into the ICP, which could not be decomposed completely in the ICP.[58] However, the variation of FIs for smaller ablated particles and the chemical composition of fine particles have not been sufficiently investigated. Koch *et al.* studied the particle size distributions and composition of a brass sample.[56] In the current study, we used NIST 610 glass standard material as a sample. Four fractions of size-classified ablated particles (Dp values of <0.06, 0.06–0.22, 0.22–2.2, and >2.2 μm) were collected on filters and digested with HNO_3 and HF, and then the elements in the particles were determined by ICPMS. Elemental fractionation is discussed

on the basis of the size distribution of mass and the relative intensity of metal and ytterbium.

3.2. Experimental

3.2.1. Instrumentation

A laser ablation system (UP-213, ESI, Portland, OR, USA) combined with an ICPMS instrument (Agilent 7500ce, Agilent Technologies, Tokyo, Japan) was used to analyze a NIST 610 (National Institute of Standards and Technology, Maryland, USA) glass standard sample. The beam the laser system was a flat top shape under in focus conditions. A commercially available large-format (15 sq. cm) laser ablation cell (ESI, Portland, OR, USA) was used. To reduce wash-out time, a quartz ring with a volume of approximately 0.8 cm^3 was put inside the large-format cell. Laser ablation was carried out in a He atmosphere, and the ablated particles were introduced into a cascade impactor (inline type with NL-1-1A (<1.0 μm), Tokyo Dylec, Tokyo, Japan), which removes ablated particles larger than 1.0 μm. Ar gas was introduced between the large-format cell and the cascade impactor. The LA-ICPMS measurement conditions used in this study are summarized in Table 3-1. In focus, 0.5 mm defocus, and 1.0 mm defocus conditions were used to evaluate the effects of defocus conditions. These three focus conditions were selected as typical trends of temporal changes of FIs. Under -1.0 mm defocus and 1.5 mm defocus conditions, no signal was observed by LA-ICPMS. Temporal changes of FIs under -0.5 mm defocus conditions showed the same trend as those under in focus conditions.

An optical microscope (VHX-2000, Keyence, Osaka, Japan) was used for detailed observation of the crater. Crater diameters and depths were measured by observing the sample from top and from side, respectively, after laser irradiation under in focus, 0.5 mm

defocus, and 1.0 mm defocus conditions. When laser ablation was performed during 10 min, 12000 shots (20 Hz × 600 s) of laser pulse were irradiated on the sample surface. The crater diameters were 100, 60, and 200 μm, respectively, and the crater depths were 380, 1500, and 1600 μm, respectively. The craters were a top hat shape under in focus conditions and a reverse circular cone shape under defocus conditions.

Table 3-1 Operating conditions used for laser ablation and ICPMS measurements

Laser Ablation		
Laser model	UP213	
Laser type	Nd:YAG	
Wavelength	213 nm	
Pulse width	4 ns	
Ablation mode	Single site	
Repetition rate	20 Hz	
Carrier gas (He) flow rate	1.0 L min^{-1}	
Laser energy on sample surface	0.9 mJ	
Initial laser fluence*		
In focus	11 J cm^{-2}	
0.5 mm defocus	30 J cm^{-2}	
1.0 mm defocus	3.0 J cm^{-2}	
Crater diameter		
In focus	100 ± 5 μm	
0.5 mm defocus	60 ± 4 μm	
1.0 mm defocus	200 ± 10 μm	
Crater depth		
In focus	380 ± 30 μm	
0.5 mm defocus	1500 ± 150 μm	
1.0 mm defocus	1600 ± 150 μm	
ICPMS Measurements		
ICPMS model	Agilent 7500cc	
RF power	1600 W	
Integration time	0.05 s	
Collision gas (He) flow rate	2.0 mL min^{-1}	
	for laser ablation	for solution nebulization
Carrier gas (Ar) flow rate	0.8 L min^{-1}	1.2 L min^{-1}
Sample uptake rate	-	0.1 mL min^{-1}
Isotopes measured	^{42}Ca, ^{75}As	^{75}As, ^{85}Rb, ^{103}Rh, ^{139}La, ^{157}Gd, ^{173}Yb, ^{182}W,^{185}Re, ^{232}Th

* Actual fluence changed with time.

3.2.2. Reagents

Hydrofluoric acid (25 M, Daikin Industries, Osaka, Japan) and HNO_3 (ultrapure, 11 M, Kanto Chemical, Tokyo, Japan) were used for acid digestion. Calibration standard solutions were prepared from the following SPEX CertiPrep (Metuchen, NJ, USA) multielement standards for ICPMS: XSTC-1, XSTC-8, and XSTC-13. The standards were diluted with 0.1 M HNO_3. Calibration curves were prepared by the measurement of standard solutions at concentrations of 0, 10, 100, 500, and 5000 pg mL^{-1}.

3.2.3. Collection of size-classified ablated particles with a low-pressure impactor

Four fractions of size-classified ablated particles (Dp values of <0.06, 0.06–0.22, 0.22–2.2, and >2.2 μm) were collected by means of a low-pressure impactor (LP-20; Tokyo Dylec Co., Tokyo, Japan), which was placed in an ISO class 4 clean bench equipped with HEPA filters (Fig. 3-1). Particle fractions were collected on PTFE filters (T010A080C, 80 mm diameter, Advantec Toyo Kaisya, Tokyo, Japan), except for the finest fraction (<0.06 μm), which was collected on a quartz fiber filter (2500 QAT-UP; 80 mm diam., Pall Corporation, Port Washington, NY, USA).

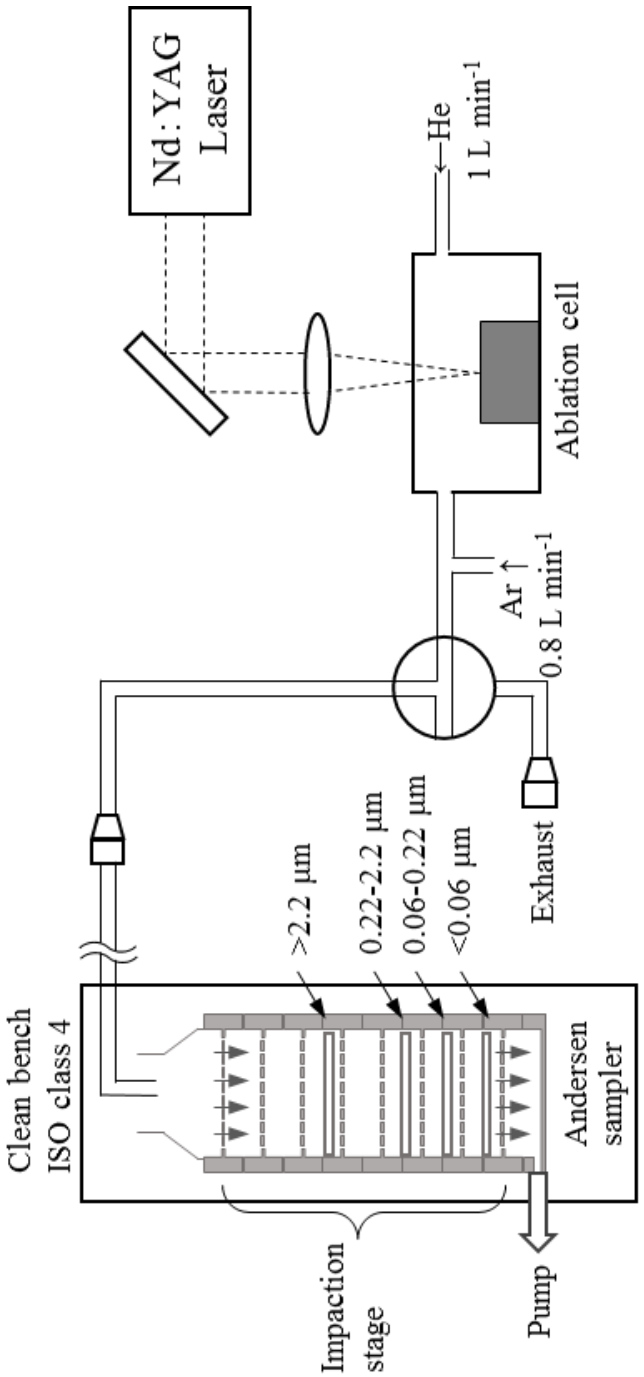

Fig. 3-1 Schematic diagram of experimental setup used to collect ablated particles on four separate filters.

3.2.4. Acid digestion

The collected particles were decomposed with a mixture of 25 M HF (0.3 mL) and 11 M HNO_3 (0.6 mL) at 180 °C on a hotplate until the HF had evaporated completely. Heating continued until the digested solution became one droplet. Then, the digested solution was diluted to 2 mL with 0.1 M HNO_3. As an internal standard, 20 ng of Rh was added into the samples.

3.3. Results and discussion

3.3.1. Fractionation index obtained by means of LA-ICPMS with a cascade impactor

Using the single-site mode under in focus, 0.5 mm defocus, and 1.0 mm defocus conditions, we measured the elemental intensities of As and Ca by means of time-resolved analysis. In the previous paper,[58] 34 elements were classified into two groups in accordance with their observed temporal changes of FIs. Elements in the first group (Group 1) showed the FI peak at 2-3 min after the start of laser ablation under defocus conditions. Volatile elements such as As are included in the first group. Elements in the second group (Group 2) did not show the FI peak as laser ablation progressed. Non-volatile elements such as Ca are included in the second group. For this set of experiments, As was selected as a typical element of the first group of elements. The signal intensities and FIs for As as a function of ablation time are shown in Fig. 3-2.

Under the in focus conditions, the plot of FIs for As did not show a peak at an ablation time of 2–3 min, whereas a peak in FIs was observed at 2–3 min under the 0.5 mm defocus and 1.0 mm defocus conditions (Fig. 3-2d–f). The magnitudes of the FI peaks were 2.3 without the 1.0 μm impactor and 1.9 with the impactor under the 0.5 mm defocus

conditions. Under the 1.0 mm defocus conditions, the corresponding magnitudes were 1.9 and 1.4, respectively. That is, although the FI peak was suppressed by the use of the impactor, the peak did not disappear completely.

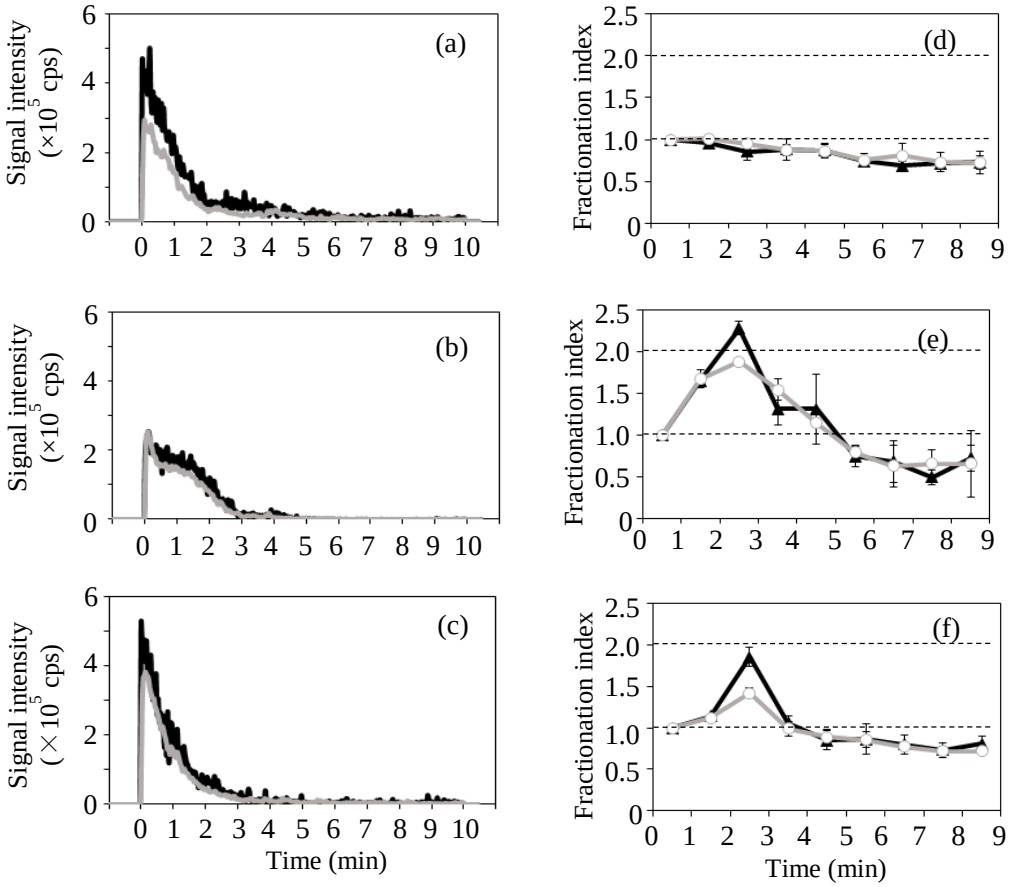

Fig. 3-2 Signal intensities of As obtained by LA-ICPMS. Laser ablation was performed under (a) in-focus, (b) 0.5 mm defocus, and (c) 1.0 mm defocus conditions without (black) and with (gray) a 1.0 μm impactor. Fractionation indexes of As during laser ablation under (d) in-focus, (e) 0.5 mm defocus, and (f) 1.0 mm defocus conditions without (triangles) and with (circles) a 1.0 μm impactor. Error bars indicate standard deviations (n = 3).

3.2.2. Mass of size-classified ablated particles collected with a low-pressure impactor

The size-classified ablated particles were collected on different filters by means of the low-pressure impactor sampler. The particle fractions were decomposed with acid, and ICPMS was used to determine Yb, which was suitable for estimation of the mass of ablated particles because the background was low and the sensitivity was high for ICPMS measurement. Moreover, Yb is typical of the elements classified as Group 2 in our previous study.[58] The mass of ablated particles was calculated from the mass of Yb by dividing by the certified value for Yb (473 μg g^{-1}) in the NIST 610 glass standard. A mass fraction was calculated by dividing the mass of ablated particles at 1-5 min to the mass of ablated particles at 0-1 min.

The masses of ablated particles and the mass fractions of the size-classified ablated particles are shown in Fig. 3-3. The total masses of ablated particles collected at 0-1 min of ablation under in focus, 0.5 mm defocus, and 1.0 mm defocus conditions were 15.2, 10.2, and 8.8 pg, respectively, and the total masses of ablated particles collected at 1-5 min under in focus, 0.5 mm defocus, and 1.0 mm defocus conditions were 5.1, 3.6, and 3.2 pg, respectively. The ratios of the total masses collected at 1-5 min to the total masses collected at 0-1 min of ablation were 34%, 35%, and 36% under in focus, 0.5 mm defocus, and 1.0 mm defocus conditions, respectively. Under the defocus conditions, the mass fractions of particles larger than 0.22 μm were high: specifically, 57% (0.22–2.2 μm) and 59% (>2.2 μm) under the 0.5 mm defocus conditions and 54% (0.22–2.2 μm) and 51% (>2.2 μm) under the 1.0 mm defocus conditions. These results confirm that the mass of particles larger than 0.22 μm was higher at 1–5 min than at 0–1 min when laser ablation was performed under defocus conditions.

Smaller particles (<0.06 μm) were produced in greater amounts than larger particles. However, under all three focus conditions, the mass fractions of these smaller particles were the same as the ratios of the total masses collected at 1-5 min to the total masses collected at 0-1 min of ablation. The mass fractions of the larger particles increased under defocus conditions. Therefore, we concluded that the FI peak at 2–3 min was caused by changes in ablated particles larger than 0.22 μm.

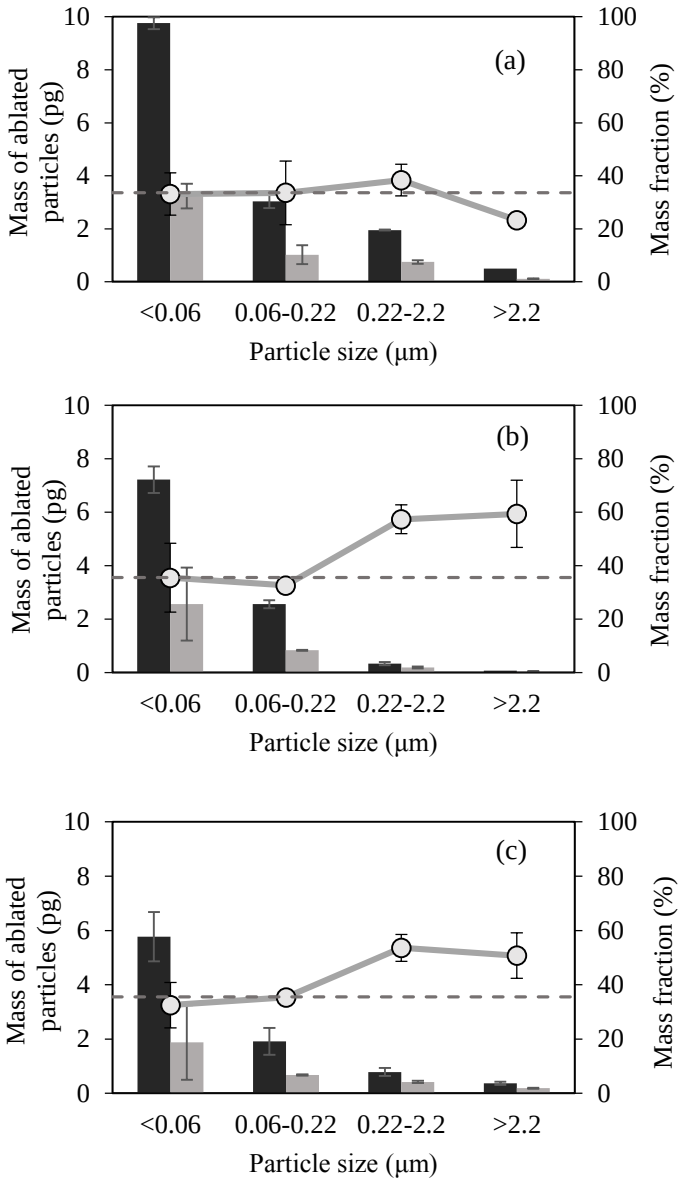

Fig. 3-3 Masses of ablated particles (bars) and mass fractions of size-classified ablated particles obtained under (a) in focus, (b) 0.5 mm defocus, and (c) 1.0 mm defocus conditions at 0-1 min of ablation (black bars) and at 1-5 min of ablation (gray bars). Dashed lines indicate the ratios of the total masses collected at 1-5 min to the total masses collected at 0-1 min. Error bars indicate standard deviations (n = 3).

3.2.3. Chemical composition of size-classified ablated particles

The amounts of As, Rb, Re, W, La, Gd, Th, and Yb in the size-classified ablated particles were determined by means of ICPMS, and temporal FIs were calculated from Eq. (3-1):

$$\text{temporal FI} = \left[\frac{(\text{M} / \text{Yb})_{\text{1-5 min}}}{(\text{M} / \text{Yb})_{\text{0-1 min}}} \right] \qquad (3\text{-}1)$$

where $(M/Yb)_{1\text{-}5\ min}$ is the relative intensity of element M normalized by the signal intensity of Yb at 1-5 min of ablation, and $(M/Yb)_{0\text{–}1\ min}$ is the relative intensity of element M normalized by the signal intensity of Yb at 0-1 min of ablation. The relative intensities and temporal FIs of all the elements, along with the melting points (mp) of their oxides, are listed in Table 3-2. The temporal FIs of the first group of elements (Group 1) were between 0.8 and 1.2 and those of the second group of elements (Group 2) were between 0.9 and 1.1. All the FIs were approximately 1 and did not depend on the size of the ablated particles, indicating that the magnitude of the enrichment did not change as laser ablation progressed.

The crater aspect ratios under in focus (11 J cm^{-2}), 0.5 mm defocus (30 J cm^{-2}), and 1.0 mm defocus (3.0 J cm^{-2}) conditions were 3.8, 25, and 8.0, respectively. The fluence was calculated from the diameter of the crater produced on the sample surface. The actual fluence increased as laser ablation progressed. For the elemental composition, the relative intensities of As in the particles smaller than 0.06 μm at 0-1 min of ablation under in focus, 0.5 mm defocus, and 1.0 mm defocus conditions were 0.08, 0.20, and 0.13, respectively. The corresponding values for Rb were 1.53, 2.73, and 1.81. The relative intensities of the volatile elements under 0.5 mm defocus conditions were larger than those of the ones under in focus and 1.0 mm defocus conditions. However, the relative intensities of the elements in Group 2 were constant regardless of the focus conditions.

The relative intensities of volatile elements increased as the aspect ratio of the crater increased. The relative intensities of As at 0-1 min of ablation under 0.5 mm defocus conditions were 0.20, 0.17, 0.09, and 0.11 for particles with sizes of <0.06, 0.06–0.22, 0.22–2.2, and >2.2 μm, respectively. The relative intensities of As in particles smaller than 0.22 μm were larger than those of As in particles larger than 0.22 μm. The same trend was observed for Rb. We confirmed that during laser ablation, the magnitude of the enrichment varied with the aspect ratio.[61] Volatile elements were enriched in smaller particles because smaller particles were generated by hydrodynamic sputtering in the heat-effective zone on the sample surface. The size dependence of the chemical composition of the particles was caused by noncongruent evaporation.[62-64]

However, the relative intensities of elements in Group 1 at 1-5 min of ablation were the same as those observed at 0-1 min of ablation. That is, the magnitude of the enrichment of the elements in Group 1 at 0-1 min of ablation was the same as that at 1-5 min of ablation. This result indicates that the FI peak observed for elements in Group 1 at 2–3 min after the start of laser ablation was not caused by smaller particles but by particles larger than 0.22 μm. Particles larger than 0.22 μm could not be decomposed completely in the ICP and elements in Group 1 were more easily vaporized and ionized than Ca.

Table 3-2 Relative intensity data for size-classified particles and temporal FIs of elements along with melting points of their oxides

			Aerodynamic diameter under in focus conditions											
			<0.06 μm			0.06-0.22 μm			0.22-2.2 μm			>2.2 μm		
Group*	Element	mp of oxide (°C)	Relative intensity $(M/Yb)_{0-1}$	$(M/Yb)_{1-5}$	temporal FI	Relative intensity $(M/Yb)_{0-1}$	$(M/Yb)_{1-5}$	temporal FI	Relative intensity $(M/Yb)_{0-1}$	$(M/Yb)_{1-5}$	temporal FI	Relative intensity $(M/Yb)_{0-1}$	$(M/Yb)_{1-5}$	temporal FI
1	As	274	0.08	0.09	1.1 ± 0.2	0.04	0.05	1.1 ± 0.2	0.04	0.05	1.1 ± 0.2	0.06	0.05	1.0 ± 0.2
1	Rb	412	1.53	1.66	1.1 ± 0.0	0.84	0.94	1.1 ± 0.1	0.87	0.77	0.9 ± 0.1	0.99	0.96	1.0 ± 0.2
1	Re	900	0.19	0.17	0.9 ± 0.1	0.15	0.17	1.1 ± 0.1	0.15	0.15	1.0 ± 0.2	0.18	0.16	0.9 ± 0.2
1	W	1500	1.01	0.90	0.9 ± 0.1	0.88	0.92	1.0 ± 0.1	0.94	0.76	0.8 ± 0.2	0.90	0.85	0.9 ± 0.0
2	La	2315	3.47	3.51	1.0 ± 0.1	3.34	3.53	1.1 ± 0.1	3.45	3.37	1.0 ± 0.0	3.79	3.36	0.9 ± 0.1
2	Gd	2339	0.75	0.76	1.0 ± 0.2	0.72	0.77	1.1 ± 0.1	0.72	0.73	1.0 ± 0.0	0.82	0.80	1.0 ± 0.4
2	Th	3390	3.00	2.64	0.9 ± 0.1	3.41	3.48	1.0 ± 0.0	3.45	3.47	1.0 ± 0.0	3.39	3.38	1.0 ± 0.0

			Aerodynamic diameter under 0.5 mm defocus conditions											
			<0.06 μm			0.06-0.22 μm			0.22-2.2 μm			>2.2 μm		
Group*	Element	mp of oxide (°C)	Relative intensity $(M/Yb)_{0-1}$	$(M/Yb)_{1-5}$	temporal FI	Relative intensity $(M/Yb)_{0-1}$	$(M/Yb)_{1-5}$	temporal FI	Relative intensity $(M/Yb)_{0-1}$	$(M/Yb)_{1-5}$	temporal FI	Relative intensity $(M/Yb)_{0-1}$	$(M/Yb)_{1-5}$	temporal FI
1	As	274	0.20	0.22	1.1 ± 0.1	0.17	0.20	1.2 ± 0.2	0.09	0.09	1.0 ± 0.3	0.11	0.10	0.9 ± 0.2
1	Rb	412	2.73	2.60	1.0 ± 0.3	1.68	1.70	1.0 ± 0.2	0.91	0.80	0.9 ± 0.1	0.96	0.95	1.0 ± 0.2
1	Re	900	0.16	0.16	1.0 ± 0.2	0.36	0.37	1.0 ± 0.2	0.17	0.15	0.9 ± 0.2	0.11	0.10	0.9 ± 0.3
1	W	1500	1.47	1.47	1.0 ± 0.1	1.97	2.15	1.1 ± 0.2	1.14	1.03	0.9 ± 0.1	1.14	1.12	1.0 ± 0.3
2	La	2315	3.73	3.42	0.9 ± 0.1	3.90	3.73	1.0 ± 0.1	3.37	3.43	1.0 ± 0.1	2.89	3.02	1.0 ± 0.1
2	Gd	2339	0.84	0.88	1.1 ± 0.1	0.79	0.75	0.9 ± 0.1	0.68	0.63	0.9 ± 0.1	0.77	0.77	1.0 ± 0.3
2	Th	3390	2.73	2.88	1.1 ± 0.1	3.01	3.01	1.0 ± 0.0	2.85	2.75	1.0 ± 0.1	2.65	2.81	1.1 ± 0.3

			Aerodynamic diameter under 1.0 mm defocus conditions											
			<0.06 μm			0.06-0.22 μm			0.22-2.2 μm			>2.2 μm		
Group*	Element	mp of oxide (°C)	Relative intensity $(M/Yb)_{0-1}$	$(M/Yb)_{1-5}$	temporal FI	Relative intensity $(M/Yb)_{0-1}$	$(M/Yb)_{1-5}$	temporal FI	Relative intensity $(M/Yb)_{0-1}$	$(M/Yb)_{1-5}$	temporal FI	Relative intensity $(M/Yb)_{0-1}$	$(M/Yb)_{1-5}$	temporal FI
1	As	274	0.13	0.15	1.1 ± 0.3	0.06	0.05	0.9 ± 0.1	0.06	0.05	1.0 ± 0.2	0.09	0.10	1.1 ± 0.1
1	Rb	412	1.81	1.68	0.9 ± 0.2	0.84	0.92	1.1 ± 0.2	0.84	0.81	1.0 ± 0.1	0.91	0.92	1.0 ± 0.3
1	Re	900	0.19	0.18	1.0 ± 0.2	0.16	0.17	1.1 ± 0.1	0.12	0.12	1.0 ± 0.2	0.17	0.18	1.0 ± 0.3
1	W	1500	1.04	1.15	1.1 ± 0.4	N. D.	N. D.	−	N. D.	N. D.	−	N. D.	N. D.	−
2	La	2315	3.14	3.46	1.1 ± 0.1	3.52	3.85	1.1 ± 0.1	3.51	3.69	1.1 ± 0.1	3.63	3.98	1.1 ± 0.2
2	Gd	2339	0.67	0.76	1.1 ± 0.3	0.74	0.78	1.1 ± 0.1	0.75	0.71	0.9 ± 0.1	0.77	0.81	1.1 ± 0.2
2	Th	3390	3.20	2.96	0.9 ± 0.3	3.36	3.40	1.0 ± 0.0	3.34	3.11	0.9 ± 0.1	3.27	3.62	1.1 ± 0.2

Table 2.2

3.4. Summary

In this study, ablated particles were classified by the size, and the chemical composition of the particles was investigated. The FI peak observed for elements in Group 1 under defocus conditions at 2–3 min after the start of laser ablation was suppressed by the use of a 1.0 μm impactor, but the peak did not disappear completely. Under the in focus conditions, the mass fraction of ablated particles did not change. In contrast, under 0.5 mm defocus and 1.0 mm defocus conditions, the mass fraction of ablated particles increased for ablated particles larger than 0.22 μm.

Volatile elements were enriched in small particles produced during laser ablation regardless of the focus conditions. The magnitude of the enrichment increased as the aspect ratio of the crater increased. However, the magnitude of the enrichment at 0-1 min of ablation was the same as that at 1-5 min of ablation. These experimental results indicate that the FI peak observed for Group 1 elements under defocus conditions at 2–3 min after the start of ablation was not caused by smaller particles but by particles larger than 0.22 μm. Particles larger than 0.22 μm could not be decomposed completely in the ICP and elements in Group 1 were more easily vaporized and ionized than Ca.

Chapter 4

Particle size-related elemental fractionation in laser ablation in liquid (LAL)

4.1. Introduction

4.2. Experimental

4.2.1. Instrumentation

4.2.2. Reagents

4.2.3. LAL sampling

4.2.4. Acid digestion

4.3. Results and discussion

4.3.1. Optimization of the LAL sampling procedure

4.3.2. Line-scanning mode and single-site mode

4.3.3. Dependence of elemental fractionation on the size of particles generated by LAL in line-scanning mode

4.3.4. Quantification of NIST 610 by LAL-ICPMS

4.3.5. Comparison of elemental fractionation in the ICP with that during LAL sampling

4.4. Summary

Chapter 4 Particle size-related elemental fractionation in laser ablation in liquid (LAL)

4.1. Introduction

Laser ablation inductively coupled plasma mass spectrometry (LA-ICPMS) is a technique for direct analysis of solid samples without the need for sample preparation procedures; ablated particles are generated by the interaction between laser light and the sample surface. LA-ICPMS has been used for various purposes, such as isotope-ratio analysis in the field of earth science and qualitative analysis of biological tissues and other materials.[13, 53, 65, 66] Various quantitative strategies that use LA-ICPMS have been investigated, such as a correction method involving the use of a relative sensitivity factor and a standard addition method.[18, 67-69] However, LA-ICPMS suffers from elemental fractionation, whereby elements in a sample are enriched or depleted during the LA process and in the ICPMS, depending on the properties of the elements. Although the problem of elemental fractionation has not yet been solved. During laser ablation process, elemental fractionation depends on the laser type, operating conditions, and aspect ratio (depth/diameter) of a crater. Larger elemental fractionation occurs when aspect ratios of crater incresase.[70] On the other hand in the ICP, elemental fractionation occurs when particles larger than a critical size are introduced into the ICP. For example, one hundred fifty nanometer (150 nm) is a critical size for silicates.[25] Shorter laser-pulse durations (e.g., on the order of femtoseconds) and the use of ultraviolet radiation (193 nm) have been investigated for the smaller heat effective zone and the generation of smaller particles.[31, 51, 56, 60]

Laser ablation in liquid (LAL) was first reported as a technique for the generation of

nanomaterials in 2003, and ablation mechanisms have been widely studied.[35–37] In this technique, the sample surface is irradiated by a laser beam through a liquid medium. Interest in LAL has been increasing recently owing to its versatility. For instance, LAL has been used for surface-enhanced Raman scattering labeling, production of nanomaterial coatings, photonic materials, and catalysis.[71–74] LAL-sampled particles can be analyzed by ICPMS. Although quantitative analysis by means of slurry nebulization and isotope-ratio analysis have been reported,[10, 38] quantification of volatile elements such as As has not been reported. The contributions of particle size–related elemental fractionation during LA and in the ICP have not been clarified. Although slurry nebulization is useful for quantitative analysis,[75-77] the analysis is carried out on the assumption that the particles decompose completely in the ICP. However, large particles do not in fact decompose completely, and the extent of vaporization and atomization of the elements in the particles depends on the elemental properties.[78, 79] If these effects could be elucidated, ICPMS analysis with LAL sampling could be an effective tool for the determination of trace elements in hard-to-digest materials, such as glass and fine ceramics.

In this study, elemental fractionation during LAL sampling was investigated separately from elemental fractionation in the ICP. Particle size-related elemental fractionation during LAL sampling was evaluated by comparison between LAL-sampled particles larger than 0.4 μm and those smaller than 0.4 μm, and elemental fractionation in the ICP was evaluated by comparison between the results obtained by slurry nebulization and those obtained by acid digestion.

4.2. Experimental

4.2.1. Instrumentation

A laser ablation system (UP-213, ESI, Portland, OR, USA) was used for LAL sampling. A microwave acid digestion system (ETHOS One, Milestone Sorisole, Italy) was used for decomposition of samples collected on a polycarbonate filter. ICPMS was conducted with an Agilent 7500ce instrument (Agilent Technologies, Tokyo, Japan) at settings optimized to provide the highest sensitivity for ^{7}Li, ^{89}Y, and ^{205}Tl and to keep the ^{140}Ce^{16}O/^{140}Ce ratio below 3% (Table 4-1). A scanning electron microscope (S-4300, Hitachi High Technologies, Tokyo, Japan) was used to observe the LAL-sampled particles. The particles were collected on a 0.4 μm polycarbonate filter, the surface of which was coated with a Pt/Pd alloy with an ion-beam sputter coater (E-1045, Hitachi High Technologies, Tokyo, Japan) prior to measurement.

Table 4-1 Operating conditions used for laser ablation in liquid inductively coupled plasma mass spectrometry (ICPMS)

Laser model	UP213
Laser type	Nd:YAG
Wavelength	213 nm
Pulse width	4 ns
Ablation mode	Single-site or line-scanning
Repetition rate	20 Hz
Diameter of crater	100 μm
Laser fluence	6 J cm^{-2}
Scanning speed	10 μm s^{-1}
Sampling medium	Ultrapure water (1130 μL)

ICPMS model	Agilent 7500ce
RF power	1400 W
Integration time	0.1 s
Carrier gas (Ar) flow rate	1.2 L min^{-1}
Collision gas (He) flow rate	3.0 mL min^{-1}
Isotopes measured	^{27}Al, ^{42}Ca, ^{52}Cr, ^{55}Mn, ^{60}Ni, ^{63}Cu, ^{66}Zn, ^{69}Ga, ^{75}As, ^{85}Rb, ^{88}Sr, ^{89}Y, ^{90}Zr, ^{107}Ag, ^{111}Cd, ^{121}Sb, ^{122}Sn, ^{137}Ba, ^{157}Gd, ^{173}Yb, ^{178}Hf, ^{184}W, ^{185}Re, ^{205}Tl, ^{206}Pb, ^{209}Bi, ^{232}Th, ^{238}U

4.2.2. Reagents

Hydrofluoric acid (25 M, Daikin Industries, Osaka, Japan) and HNO_3 (Ultrapur, 11 M, Kanto Chemical, Tokyo, Japan) were used in this study. Calibration standard solutions were prepared from the following SPEX multielement standards for ICPMS: XSTC-1, XSTC-7, XSTC-8, and XSTC-13 (SPEX CertiPrep, Metuchen, NJ, USA). The multielement standards were diluted with 0.1 M HNO_3. Calibration curves were prepared by measuring standard solutions at concentrations of 0, 10, 100, 500, 5000, and 10,000 pg mL^{-1}.

4.2.3. LAL sampling

NIST 610 (National Institute of Standards and Technology, Gaithersburg, MD, USA) was used as a reference sample. NIST 610 contains 61 trace elements, and its matrix composition is 72% SiO_2, 12% CaO, 14% Na_2O, and 2% Al_2O_3. An open-top chamber made of PFA (tetrafluoroethylene–perfluoroalkyl vinyl ether copolymer) was used for LAL sampling. The outer diameter, inner diameter, and height of the chamber were 27, 18, and 10 mm, respectively. The NIST 610 sample was placed in the chamber, and then 1130 μL of ultrapure water (>18.2 MΩ cm, Milli-Q, Merck Millipore, Darmstadt, Germany) was added; as a result, the surface of the sample was 3 mm below the surface of the water. The sample surface was irradiated with the laser through the water (Fig. 4-1). In the case of single-site mode, laser irradiation was performed for 10 min and laser frequency was 20 Hz. The number of laser pulses were 12000 shots for a single position. In the case of line-scanning mode, laser lines were five with 5 mm length at 200 μm intervals. The line width was 100 μm, laser frequency was 20 Hz, and scanning speed was 10 μm s^{-1}. That is, the number of laser pulses were 200 shots a single spot of 100 μm.

The LAL-sampled particles suspended in the water were divided into two size classes by filtration: particles larger than 0.4 μm were collected on the polycarbonate filter, and particles smaller than 0.4 μm passed into the filtrate. The amount of ablated particles larger than 0.4 μm and smaller than 0.4 μm were 0.057 mg and 0.15 mg, respectively.

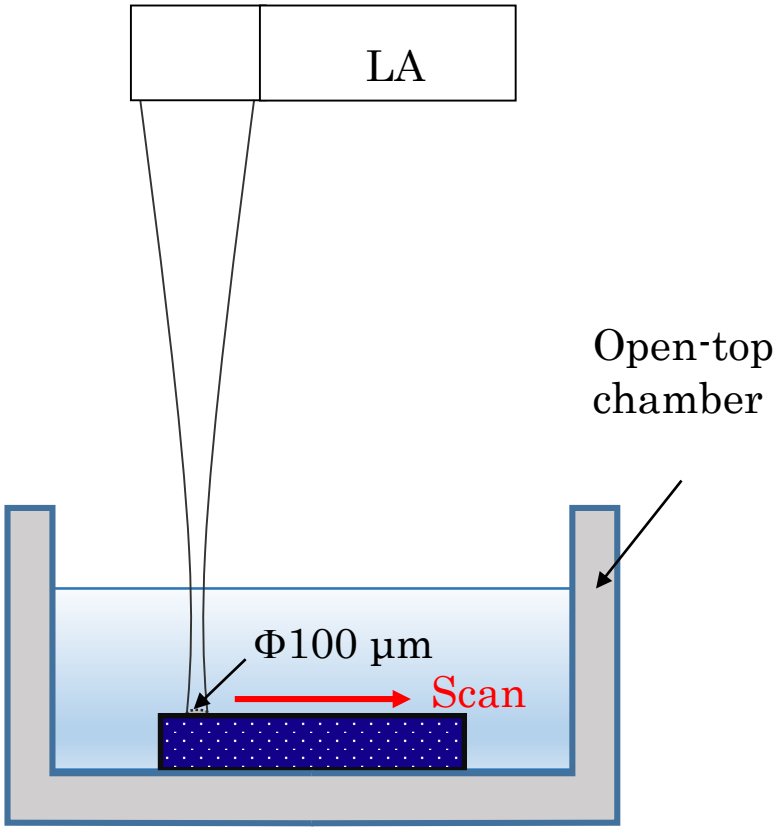

Fig. 4-1 Schematic diagram of laser ablation in liquid set-up. Red line indicates scanning direction of laser beam.

4.2.4. Acid digestion

NIST 610 was crushed and ground to a powder in an agate mortar. Two milligrams of the powder was weighed into a PFA vial and decomposed with a mixture of 0.3 mL of 25 M HF and 0.6 mL of 11 M HNO_3 at 180 °C on a hotplate. Heating was continued until the HF had evaporated completely, and then the digested solution was diluted to 100 mL with 0.1 M HNO_3. LAL-sampled particles were decomposed by means of the same procedure, except that a microwave digestion system was used for particles larger than 0.4 μm (that is, the particles that were collected on the polycarbonate filter). In the case of LAL-sampled particles, the final volume was adjusted to 10 mL with 0.1 M HNO_3 for particles larger than 0.4 μm and smaller than 0.4 μm. When microwave digestion was performed, a mixture of 3.0 mL of 25 M HF and 6.0 mL of 11 M HNO_3 was used.

4.3. Results and discussion

4.3.1. Optimization of the LAL sampling procedure

The laser focus and the distance from the water surface to the sample surface were optimized carefully for LAL sampling. A focus of a CCD camera became longer with increasing the distance from the water surface to the sample surface. Actual focus position of a laser beam was above the focus position of a CCD camera. The defocus adjustment, *Z*, can be estimated from Eq. (4-1):

$$Z = h - a \qquad (4\text{-}1)$$

where *h* is the distance between the water surface and the sample surface, and *a* is the apparent depth. *a* can be estimated from Eq. (4-2):

$$a = \frac{h}{n} \qquad (4\text{-}2)$$

where n is the refractive index of water (n = 1.333). The following Eq. (4-3) is derivable from Eq. (4-1) and Eq. (4-2):

$$Z = h\left(1 - \frac{1}{n}\right) \qquad (4\text{-}3)$$

When h is 3 mm, the defocus adjustment is calculated to be 0.75 mm, indicating that the objective lens has to be moved down 0.75 mm. The optimized value of the defocus was experimentally confirmed. Images of the ablation track after LAL sampling in line-scanning mode are shown in Fig. 4-2. The focus was adjusted while the surface was monitored with a CCD camera. Under the in-focus conditions, the width of the ablation track was 60 μm (Fig. 4-2a), which was narrower than the nominal value (controlled by the software at 100 μm). Under -0.50 mm defocus and -1.00 defocus conditions, the ablation tracks (200 and 120 μm, respectively; Fig. 4-2b and 4-2d) were wider than the nominal value. In contrast, under the -0.75 mm defocus conditions, the width of the ablation track was equal to the nominal value (Fig. 4-2c).

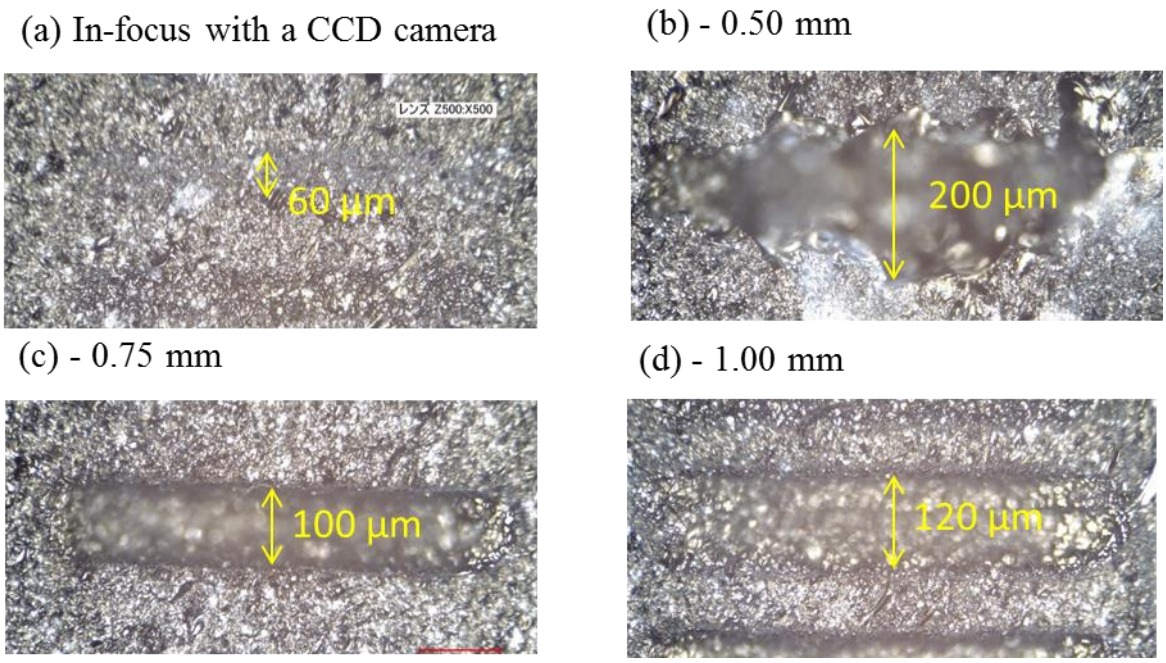

Fig. 4-2 CCD images of tracks of line scans: (a) in-focus with a CCD camera, (b) –0.50 mm defocus, (c) –0.75 mm defocus, and (d) –1.00 mm defocus.

4.3.2. Line-scanning mode and single-site mode

In both the line-scanning mode and the single-site mode, all of the LAL-sampled particles were decomposed, and the elemental intensities of Ca, As, Sr, Zr, Cd, Sb, Sn, Pb, Th, and U were measured by ICPMS. Enrichment factors (EFs) were calculated from Eq. (4-4):

$$EF = \left[\frac{\left(M_{cps}/Ca_{cps}\right)_{LAL\text{-}sample}}{\left(M_{cps}/Ca_{cps}\right)_{reference}} - 1 \right] \times 100 \qquad (4\text{-}4)$$

where $(M_{cps}/Ca_{cps})_{LAL\text{-}sample}$ is the ratio of the signal intensity of element M to that of ^{42}Ca for the sample solution obtained by LAL sampling, and $(M_{cps}/Ca_{cps})_{reference}$ is the same ratio for the sample solution obtained by decomposition of the NIST 610 powder. The EFs of these elements are shown in Fig. 4-3.

When the measurement was conducted in line-scanning mode, the EFs of all the elements were 0% ± 5%. In contrast, in single-site mode, the EFs of As, Cd, Sb, Sn, and Pb were –25%, –30%, –13%, –12%, and –14%, respectively; whereas the EFs of Sr, Zr, Th, and U were 0% ± 5%. In addition the aspect ratio of the crater was 0.5 when laser ablation was performed under line-scanning mode, and the aspect ratio of the crater was 4.8 when laser ablation was performed under single-site mode. More heating effect (preferential evaporation of volatile elements) occurs under higher aspect ratios.[70] Elemental fractionation was also observed in the heat effective zone under LAL. Cavitation bubbles were generated at microsecond to sub-millisecond after laser irradiation,[35] and then, nano particles were formed inside the cavitation bubbles.[80] In the case of single-site mode, laser irradiation heated a single spot on the sample surface, and larger cavitation bubbles were generated. Both larger aspect ratio and larger cavitation bubbles under single-site mode caused the loss of volatile elements into the gas phase via cavitation bubbles. This phenomenon was much clearer in single-site mode than in line-

scanning mode because in the former mode, large size of cavitation bubbles was generated at a single position. Our results indicate that for quantitative analysis of elements in solid samples, LAL sampling in line-scanning mode provides more-accurate results without elemental loss. To obtain reliable data, all of the ablated particles must be collected in the liquid medium.

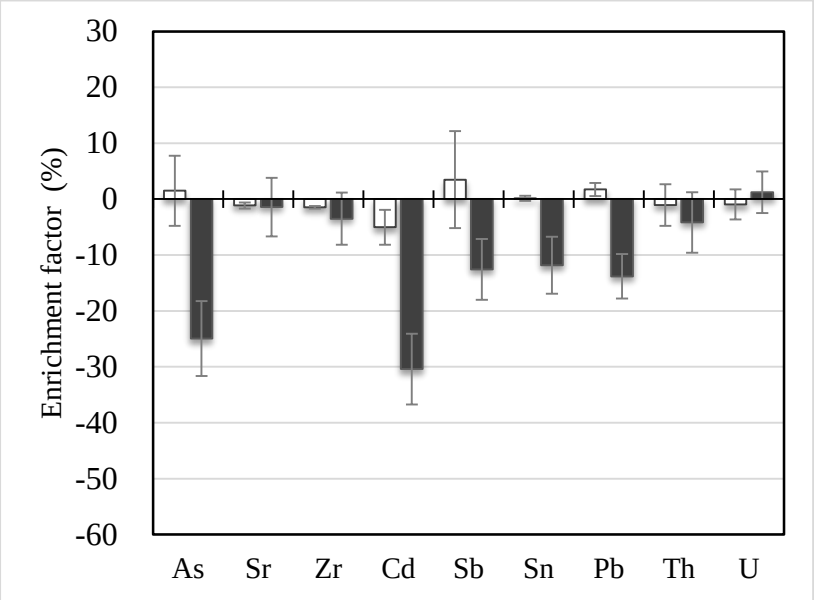

Fig. 4-3 Enrichment factors (%) for laser ablation in liquid sampling: (□) line-scan mode and (■) single-site mode. Error bars indicate standard deviations (n = 3).

4.3.3. Dependence of elemental fractionation on the size of particles generated by LAL in line-scanning mode

LAL-sampled particles obtained in line-scanning mode were divided into two size classes by filtration: particles larger than 0.4 μm (collected on the polycarbonate filter) and particles smaller than 0.4 μm (collected in the filtrate). Scanning electron microscopy images of the two sizes of particles are shown in Fig. 4-4. Spherical, agglomerated, and edge-shaped particles were observed in the image of the particles on the polycarbonate filter (Fig. 4-4a), whereas spherical particles were the main type of particles in the filtrate (Fig. 4-4b). Ablated particles are generated in the heat effective zone resulting from interaction between the sample surface and the laser beam. Larger particles are generated when hydromechanical sputtering dominates and smaller particles are generated by hydrodynamic sputtering when the heat effective zone is thin and the laser fluence is high enough for laser ablation.[62]

The elemental intensities of Ca, As, Sr, Zr, Cd, Sb, Sn, Pb, Th, and U were measured by ICPMS, and the EFs of these elements are shown in Fig. 4-5. In the case of the particles smaller than 0.4 μm, the EFs of As and Sb were 14% and 9%, respectively; these volatile elements were enriched by the melting-congelation process in the heat effective zone. In contrast, in the case of particles larger than 0.4 μm, the EFs of As, Cd, Sb, Sn, and Pb were –42%, –20%, –30%, –9%, and –14%, respectively. That is, the volatile elements were enriched in the LAL-sampled smaller particles, and depletion of the volatile elements was observed in the larger particles. These results imply that the degree of elemental fractionation during LAL sampling was related to the size of the ablated particles. Note that the EFs of As, Cd, Sb, Sn, and Pb were negative for particles larger than 0.4 μm, which means that these elements were depleted in these particles.

Analytical data for both sizes of LAL-sampled particles, along with the acid digestion data for the NIST 610 powder, are summarized in Table 4-2. The intensity values for the elements were normalized by the intensity of Ca, and the recovery percentage for each element was calculated by dividing the elemental intensity for the LAL-sampled particles by the corresponding elemental intensity for NIST 610. The recovery of all elements was 100% ± 10%. Enrichment of As, Cd, Sb, Sn, and Pb in the particles smaller than 0.4 μm and depletion of As, Cd, Sb, Sn, and Pb in the particles larger than 0.4 μm were almost balanced, within the margin of error.

Our results indicate that ICPMS analysis of LAL-sampled particles is suitable for separate study of elemental fractionation effects during LAL sampling and in the ICP. Many studies of elemental fractionation effects in LA-ICPMS have been reported,[59] but the number of papers, which described the effects that occurred during LAL sampling, during transport, and in the ICP separately, was small.[25, 81]

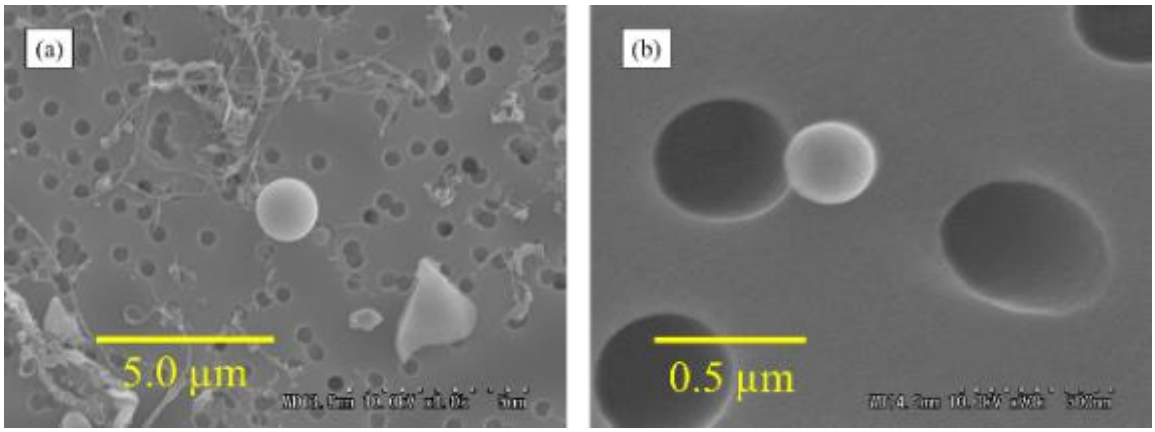

Fig. 4-4 Scanning electron microscopy images of the particles obtained by laser ablation in liquid sampling: (a) particles on the polycarbonate filter and (b) particles in the filtrate.

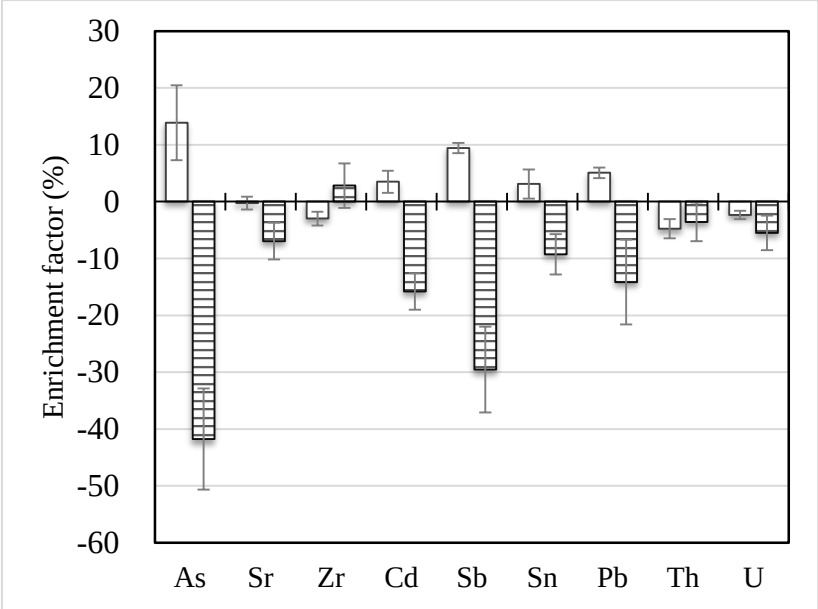

Fig. 4-5 Enrichment factors (%) for laser ablation in liquid sampling: (☐) particles ≤0.4 μm and (▤) particles >0.4 μm. Error bars indicate standard deviations (n = 3).

Table 4-2 Intensity data obtained for LAL-sampled particles and NIST 610 powder

Elements	LAL-sampled particles ≤ 0.4 μm			
	Intensity (cps)	Intensity ratio M / Ca	Enrichment Factor (%)	Enrichment (cps)
Ca	19817	1.0	—	—
As	2732	0.14	13.9 ± 6.6	378 ± 180
Cd	2294	0.12	3.5 ± 2.4	80 ± 53
Sb	8364	0.42	9.4 ± 0.9	788 ± 75
Sn	1785	0.090	3.1 ± 2.6	55 ± 45
Pb	5335	0.27	5.1 ± 0.9	271 ± 49

Elements	LAL-sampled particles >0.4 μm			
	Intensity (cps)	Intensity ratio M / Ca	Enrichment Factor (%)	Depletion (cps)
Ca	7541	1.0	—	—
As	509	0.067	-41.8 ± 8.9	-212 ± 45
Cd	723	0.096	-20.4 ± 3.7	-147 ± 26
Sb	2060	0.27	-29.5 ± 7.6	-608 ± 155
Sn	598	0.079	-9.3 ± 3.6	-55 ± 21
Pb	1673	0.22	-14.1 ± 7.4	-236 ± 124

Elements	Addition of data for LAL-sampled particles ≤0.4 μm and >0.4 μm		Acid digestion data for NIST 610 powder		Recovery (%)
	Intensity (cps)	Intensity ratio M / Ca	Intensity (cps)	Intensity ratio M / Ca	
Ca	27358	1.0	27843	1.0	100
As	3241	0.12	3514	0.13	94
Cd	3017	0.11	3038	0.11	101
Sb	10424	0.38	10734	0.39	99
Sn	2383	0.087	2428	0.087	100
Pb	7008	0.26	7253	0.26	98

4.3.4. Quantification of NIST 610 using LAL-ICPMS

The LAL-sampled particles obtained in line-scanning mode were decomposed by acid digestion, and Ag, As, Rb, Sb, Ga, Tl, Bi, Pb, Cd, Re, Sn, Cu, W, Mn, Ni, Ba, Zn, Al, Cr, Gd, Yb, Y, Sr, Zr, Hf, U, and Th were measured by ICPMS. In addition, a sample that was not subjected to acid digestion was also measured by ICPMS (by means of slurry nebulization) to investigate the effect of the particles introduced into the ICP. From The concentration of Ca, total mass of ablated particles were estimated and all the elements other than Ca were determined. The recovery percentage for each element was calculated by dividing the concentration for the elements by the certified value of NIST 610. The analytical results and the elemental recoveries, along with the certified values, are summarized in Table 4-3, in which the elements are arranged in order by the melting points of their oxides. In the case of quantification by means of LAL sampling with acid digestion, the measured data were in good agreement with the certified values, and the analytical precision was <9%. These results indicate that this method is appropriate for elemental quantification in analyses involving LAL sampling.

In the case of slurry nebulization, analytical precision for the volatile elements (such as Ag, As, Rb, Ga, Tl, Cd, and Sn) was >10%. This spike noise was caused by vaporization of the volatile elements from the larger particles. The analytical precision for the other elements was <10%, except in the cases of U and Th. The reason that the analytical precision for these two refractory elements was slightly worse may have been the higher melting points of their oxides. The recoveries of Ag, As, Sb, Ga, Pb, Cd, Re, W, and Zn were >120%. These elements are vaporized more easily than Ca (the reference) because their oxides melt at much lower temperatures than does Ca oxide (2570 °C). The recovery of elements whose oxides have melting points of >1500 °C was 100% ± 20%.

Elemental fractionation of these elements was small. Note that the recoveries of Cd and Zn greatly exceeded 100% in the case of slurry nebulization. The enhanced recovery of these two elements cannot be explained in terms of the melting points of their oxides, but perhaps it was due to the fact that Cd and Zn have lower boiling points (767 and 907 °C, respectively) than Ca (1484 °C). These elements were probably ionized more readily than Ca in the ICP.

Table 4-3 Comparison of LAL analytical data of NIST 610 glass standard obtained by slurry nebulization and acid digestion

Element	Certified	mp of oxide	Slurry nebulization			Acid digestion		
			Concentration		Recovery	Concentration		Recovery
	(μg g^{-1})	(°C)	(μg g^{-1})	(%RSD)	(%)	(μg g^{-1})	(%RSD)	(%)
Ag	254	200	390 ± 73	(18)	153 ± 19	267 ± 21	(7.8)	105 ± 8.1
As	350	274	460 ± 56	(12)	131 ± 12	346 ± 20	(5.7)	98 ± 5.9
Rb	425	412	474 ± 54	(11)	111 ± 11	439 ± 25	(5.6)	103 ± 5.7
Sb	426	570	557 ± 50	(8.9)	130 ± 9.0	416 ± 21	(5.0)	97 ± 5.2
Ga	431	660	610 ± 82	(13)	141 ± 13	462 ± 12	(2.5)	107 ± 2.7
Tl	61	717	73 ± 9.0	(12)	118 ± 12	65 ± 4.0	(6.1)	106 ± 7.3
Bi	369	817	440 ± 28	(6.3)	119 ± 6.4	396 ± 10	(2.5)	107 ± 2.5
Pb	426	897	530 ± 15	(2.8)	124 ± 2.8	434 ± 12	(2.7)	102 ± 2.9
Cd	296	900	494 ± 59	(11)	166 ± 12	298 ± 21	(7.0)	100 ± 7.3
Re	49	900	68 ± 3.6	(5.2)	138 ± 5.3	54 ± 1.7	(3.1)	108 ± 3.1
Sn	443	1080	516 ± 87	(16)	116 ± 17	471 ± 17	(3.6)	106 ± 3.8
Cu	444	1235	486 ± 14	(2.8)	109 ± 2.9	426 ± 19	(4.4)	96 ± 4.5
W	446	1500	550 ± 10	(1.8)	123 ± 1.8	458 ± 12	(2.6)	102 ± 2.6
Mn	485	1839	502 ± 4.7	(0.9)	103 ± 0.9	462 ± 8.8	(1.9)	95 ± 1.9
Ni	458	1955	476 ± 21	(4.4)	103 ± 4.4	446 ± 12	(2.6)	97 ± 2.7
Ba	458	1972	521 ± 46	(8.8)	113 ± 8.8	481 ± 13	(2.7)	105 ± 2.7
Zn	433	1974	731 ± 47	(6.4)	168 ± 6.4	470 ± 39	(8.2)	108 ± 8.3
Al	11000	2053	10532 ± 759	(7.2)	95 ± 7.2	11050 ± 281	(2.5)	100 ± 2.5
Cr	411	2329	449 ± 7.5	(1.6)	109 ± 1.7	435 ± 7.1	(1.6)	105 ± 1.6
Gd	461	2339	472 ± 44	(9.3)	102 ± 9.3	488 ± 14	(2.8)	105 ± 3.0
Yb	473	2355	464 ± 20	(4.3)	98 ± 4.3	478 ± 14	(2.9)	101 ± 2.9
Y	479	2438	447 ± 34	(7.6)	93 ± 7.6	479 ± 17	(3.5)	99 ± 3.6
Sr	515	2531	541 ± 21	(3.8)	104 ± 3.9	542 ± 11	(2.0)	105 ± 2.2
Zr	473	2709	444 ± 38	(8.5)	93 ± 8.6	482 ± 18	(3.7)	101 ± 3.7
Hf	437	2774	413 ± 15	(3.6)	94 ± 3.6	439 ± 14	(3.1)	100 ± 3.3
U	461	2827	523 ± 54	(10)	113 ± 10	469 ± 15	(3.1)	101 ± 3.3
Th	457	3390	473 ± 51	(10)	103 ± 11	442 ± 14	(3.1)	96 ± 3.2

4.3.5. Comparison of elemental fractionation in the ICP with that during LAL sampling

LAL-sampled particles were decomposed by acid and analyzed by ICPMS. The EFs obtained by means of this procedure reflect elemental fractionation during LAL sampling. In contrast, slurry nebulization was carried out after the LAL-sampled particles were already present in the sample, and therefore the EFs obtained under these conditions reflect the elemental fractionation both during LAL sampling and in the ICP. The EFs obtained for the two sizes of LAL-sampled particles and by means of the two different analytical methods are compared in Table 4-4.

For volatile elements such as As, Sb, Pb, Cd, and Sn, the EFs for particles larger than 0.4 μm were negative: –41.8%, –29.5%, –14.1%, –20.4%, and –9.3%, respectively. In contrast, the EFs obtained for the samples subjected to slurry nebulization were positive: 39.3%, 26.6%, 20.2%, 58.3%, and 14.0%, respectively. In contrast, the EFs obtained for the samples subjected to slurry nebulization were positive: 39.3%, 26.6%, 20.2%, 58.3%, and 14.0%, respectively. The data of Ca intensities in Table 4-2 shows the mass of particles corresponding to different sampling by means of LAL. The intensity data of Ca in particles smaller than 0.4 μm (19817) was 2.6 times larger than that in particles larger than 0.4 μm (7541). That is, the mass of particles smaller than 0.4 μm was 2.6 times greater than that of particles larger than 0.4 μm. The EFs of volatile elements obtained by means of slurry nebulization were larger than addition of 2.6 times positive EFs for the LAL-sampled particles smaller than 0.4 μm plus the negative EFs for the LAL-sampled particles larger than 0.4 μm. Therefore, it was concluded that positive EFs obtained by means of slurry nebulization was caused by changes of EFs for larger particles from

negative to positive values. These results indicate that the volatile elements in larger particles were depleted during LAL sampling but enriched when the particles were introduced into the ICP. Note that the magnitude of enrichment was larger than the magnitude of depletion. Therefore, we conclude that the elemental fractionation observed in the ICP was larger than that observed during LAL sampling. The EFs for Sr, Zr, U, and Th were 0% ± 7%, which suggests that these elements can be quantified without the need to consider particle size–related elemental fractionation.

The elements in Table 4-4 were classified into two groups on the basis of the magnitude of the EF obtained for slurry nebulization. As, Sb, Pb, Cd, and Sn were classified into group 1 because their EFs were >14%, and Sr, Zr, U, and Th were classified into group 2 because their EFs were 0% ± 7%. The classification of the elements on the basis of their EFs showed good agreement with the previously reported classification based on fractionation index.[33]

Table 4-4 Comparison of enrichment factors obtained for different size of LAL-sampled particles and different analytical methods

Element	Group*	LAL-sampled particles separated by size		Differenet analytical methods	
		Particles ≤0.4μm (%)	Particles >0.4μm (%)	Slurry nebulization (%)	Acid digestion (%)
As	1	13.9 ± 6.6	-41.8 ± 8.9	39.3 ± 17.1	-6.6 ± 3.8
Sb	1	9.4 ± 0.9	-29.5 ± 7.6	26.6 ± 19.7	-8.9 ± 1.8
Pb	1	5.1 ± 0.9	-14.1 ± 7.4	20.2 ± 14.4	-4.3 ± 2.1
Cd	1	3.5 ± 2.4	-20.4 ± 3.7	58.3 ± 11.9	-2.5 ± 5.8
Sn	1	3.1 ± 2.6	-9.3 ± 3.6	14.0 ± 13.6	-6.8 ± 4.4
Sr	2	-0.3 ± 1.1	-6.9 ± 3.2	6.6 ± 3.8	-4.5 ± 1.3
Zr	2	-3.0 ± 1.2	2.8 ± 3.9	-5.2 ± 3.9	-2.1 ± 2.0
U	2	-2.3 ± 0.7	-5.5 ± 3.0	4.1 ± 4.1	-6.3 ± 1.7
Th	2	-4.8 ± 1.7	-3.6 ± 3.4	-2.7 ± 8.0	-6.2 ± 1.7

* Table 2-2

4.4. Summary

In this study, we investigated elemental fractionation in LAL-ICPMS by separately determining the magnitude of fractionation during LAL sampling and in the ICP. The LAL-ablated particles were completely collected in water. LAL-ablated particles exhibited elemental fractionation that was related to particle size. Volatile elements were enriched in particles smaller than 0.4 μm and depleted in particles larger than 0.4 μm. Our results indicate that both positive and negative fractionations occurred during LAL sampling. Scanning electron microscopy indicated that the smaller particles were spherical. These particles were produced through melting and congelation in the heat effective zone on the sample surface. The larger particles were spherical, agglomerated, and edge shaped. Our results indicate that the volatile elements were depleted in the larger particles and enriched in the smaller particles.

When all of the LAL-sampled particles were collected and analyzed by ICPMS after acid digestion, accurate and precise data were obtained, indicating that LAL sampling is a useful technique for quantitative analysis.

Chapter 5

Determination of trace elements in silicon carbide (SiC)

5.1. Introduction

5.2. Experimental

5.2.1. Instrumentation

5.2.2. Calculation of ablated amounts and sampled amounts

5.2.3. Reagents

5.2.4. Sample preparation

5.3. Results and discussion

5.3.1. SEM observation of LAL-sampled particles

5.3.2. Analysis of NMIJ 8001a and NMIJ 8002a CRMs

5.3.3. Analysis of sintered SiC and single-crystal SiC

5.4. Summary

Chapter 5 Determination of trace elements in silicon carbide (SiC)

5.1. Introduction

Laser ablation inductively coupled plasma mass spectrometry (LA-ICPMS) permits multielement analysis with minimal sample preparation and is widely used for direct analysis of solid samples. However, it requires calibration with a CRMs that has a matrix similar to that of the sample to minimize the effects of elemental fractionation related to matrix effects.[49, 53, 58] Because the preparation of matrix-matched CRMs is difficult and laborious, many alternative calibration strategies have been proposed for quantitative analysis by LA-ICPMS. For example, commercially available NIST reference glasses (SRM 610–617) have been widely used for LA-ICPMS applications with non-matrix-matched calibration;[60, 82, 83] and standard solution calib-ration,[18, 19] external calibration,[84] and online isotope dilution methods have also been reported.[67, 85, 86]

Silicon carbide (SiC) is used in various products in single-crystal, powder, and sintered forms.[40] Owing to its superior hardness, heat resistance, and chemical stability, sintered SiC has recently been used for semiconductor manufacturing equipment. Moreover, the use of single-crystal SiC for semiconductor power devices has been investigated because the bandgap and electric breakdown field strength of SiC are higher than those of silicon.[39, 41]

If SiC is to be used in such devices, the concentrations of dopants in the p–n junction formed on the surface layer must be controlled. Techniques for implanting dopants have been evaluated by means of secondary ion mass spectrometry (SIMS).[46, 87] This technique can be used to determine the depth profile of the dopants, but the oblique impact angle

and the primary ion energy have to be optimized for each element. SIMS is also useful for obtaining the depth profile of ion impurities (donors and acceptors),[88] but it is not appropriate for quantitative analysis, because matrix effects and variations of the accuracy and precision values are larger than those of LA-ICPMS and glow discharge mass spectrometry (GD-MS).[4, 5, 89] Bulk analysis is generally performed by means of GD-MS,[90-93] which has detection limits ranging from 0.0005-0.1 μg g^{-1}.[94] However, the detection limit is influenced by the sample matrix and the sample conductivity, and the detection limits of trace elements in SiC have been reported to range from 1-100 μg g^{-1}.[32] GD-MS is useful for qualitative analysis of bulk samples. SiC powder has been analyzed by means of LA-ICPMS with non-matrix-matched calibration,[66] and the measured concentrations of B, Ti, Cr, Mn, Fe, Ni, and Cu in a reference material (BAM-S003) were found to be in good agreement with the certified values. Slurry nebulization ICPMS has also been used for analysis of SiC powder.[95]

When SiC is used as a semiconductor substrate, the purity of the surface layer (several micrometers in depth) is important for the performance of wiring patterns formed on the substrate. Semiconductor failures such as reversal of the p–n junction can occur if metal impurities are present in the surface layer. Highly sensitive and accurate quantification is required to control contamination of the surface layer of the SiC substrate. In silicon semiconductor manufacturing, surface layer analysis can be performed by means of acid digestion ICPMS. However, this technique cannot be used for analysis of SiC surfaces, because some SiC crystal types are hard to digest, and therefore quantitative analysis of the surface layer of single-crystal SiC by means of acid digestion ICPMS has not been reported.

Recently, laser ablation in liquid (LAL) sampling was reported to produce

nanoparticles.[10, 38, 64] The sample is set in ultrapure water, the sample surface is laser ablated through the water, and the ablated particles are collected in the water and then analyzed by ICPMS with acid digestion. The micro- to nanosized particles produced by LAL sampling are more easily decomposed than the particles produced by sample cracking. In addition, LAL-ICPMS can be expected to provide reliable data because solution calibration can be used. In this study, impurities in SiC powder CRMs, sintered SiC, and single-crystal SiC were quantified by means of LA-ICPMS and LAL-ICPMS. The accuracies and limits of quantification (LOQs) of the two analytical techniques were compared.

5.2. Experimental

5.2.1. Instrumentation

A LA system (UP213, ESI, Portland, OR, USA) combined with an ICPMS instrument (Agilent 7500ce, Agilent Technologies, Tokyo, Japan) was used in this study. We used NMIJ 8001a and NMIJ 8002a from the National Metrology Institute of Japan (Ibaraki, Japan) and JCRM R021, JCRM R022, and JCRM R023 from the Ceramic Society of Japan (Tokyo, Japan) as CRMs. The certified values of the CRMs are summarized in Table 5-1. He gas was used to introduce ablated particles into a cascade impactor (inline type with NL-1-1A (<1.0 μm), Tokyo Dylec, Tokyo, Japan). Ar gas was added between the laser cell and the impactor. The operating conditions for the LA system and the ICPMS instrument are summarized in Table 5-2.

Using the NIST612 glass standard, we tuned the LA-ICPMS system to provide the highest sensitivity for ^{59}Co, ^{139}La, and ^{232}Th. For the determination of elements, LA was carried out in line-scanning mode under in-focus conditions. The diameter of crater and

the line width were 100 μm, the repetition rate was 20 Hz, the scanning speed was 10 μm s^{-1}, and the scanning time was 30 s, resulting in a single laser line with a length of 0.3 mm. The concentrations of ^{27}Al, ^{47}Ti, ^{52}Cr, ^{55}Mn, ^{56}Fe, ^{59}Co ^{60}Ni, ^{63}Cu, ^{88}Sr, ^{89}Y, ^{90}Zr, and ^{184}W were measured by LA-ICPMS with ^{29}Si as an internal standard. To obtain the depth profiles of elements in sintered SiC, LA was carried out in single site mode under in-focus conditions. The diameter of crater was 100 μm and repetition rate was 5 Hz. The depth profiles of ^{27}Al, ^{89}Y and ^{90}Zr were measured by LA-ICPMS with ^{29}Si as an internal standard.

Two plasma conditions were used for quantitative analysis by solution nebulization ICPMS: hot plasma in a helium collision mode was used for determination of ^{27}Al, ^{47}Ti, ^{52}Cr, ^{59}Co, ^{60}Ni, ^{63}Cu, ^{88}Sr, ^{89}Y, ^{90}Zr, and ^{184}W, and a cool plasma mode was used for determination of ^{55}Mn and ^{56}Fe. ^{103}Rh was measured as an internal standard under both plasma conditions.

An optical microscope (VHX-2000, Keyence, Osaka, Japan) was used for detailed observation of the ablated track of the single-crystal SiC. SiC particles were observed by scanning electron microscopy (SEM; S-4300, Hitachi High Technologies, Tokyo, Japan). All the sample surfaces were coated with a Pt/Pd alloy by ion sputtering (E-1045, Hitachi High Technologies, Tokyo, Japan) for SEM measurements.

Table 5-1 Certified values (in μg g^{-1}) of CRMs of SiC powder (NMIJ and JCRM)

Element	CRMs of NMIJ		CRMs of JCRM		
	NMIJ 8001a	NMIJ 8002a	R021	R022	R023
Al	83.2 ± 7.2 (8)	189 ± 19 (10)	390 ± 20 (5)	580 ± 20 (3)	30 ± 3 (10)
Ti	6.37 ± 0.68 (11)	47.7 ± 3 (6)	100 ± 4 (4)	30 ± 0	<10
Cr	1.98 ± 0.52 (26)	61.9 ± 9.4 (15)	40 ± 3 (8)	60 ± 5 (8)	10 ± 0
Mn	0.53 ± 0.09 (17)	1.6 ± 0.34 (21)	<10	10 ± 0	<10
Fe	46.7 ± 7.8 (17)	130 ± 7.4 (6)	180 ± 10 (6)	510 ± 10 (2)	150 ± 9 (6)
Co	-	-	-	-	-
Ni	1.52 ± 0.22 (15)	4.43 ± 0.8 (18)	10 ± 0	10 ± 0	10 ± 0
Cu	0.47 ± 0.17 (36)	11.5 ± 2.6 (23)	-	-	-
Sr	-	-	-	-	-
Y	0.31 ± 0.07 (21)	0.58 ± 0.07 (12)	-	-	-
Zr	-	-	10 ± 0	10 ± 0	<10
W	-	-	-	-	-

* The value in parentheses indicates the %RSD (n=3).

Table 5-2 Operating conditions used for laser ablation and ICPMS measurements

Laser model	UP213		
Laser type	Nd:YAG		
Wavelength	213 nm		
Pulse width	4 ns		
Laser energy	0.9 mJ		
Fluence	11 J cm^{-2}		
Laser frequency	20 Hz		
Ablation mode	Line scanning		
Scanning speed	10 µm sec^{-1}		
Diameter of crater	100 µm		
Carrier gas flow (He)	1.0 L min^{-1}		
ICPMS model	**Agilent 7500ce**		
	Solution nebulization		Laser ablation
Plasma condition	Hot plasma	Cool plasma	Hot plasma
RF power	1500 W	700 W	1500 W
Integration time	0.1 sec	0.1 sec	0.05 sec
Carrier gas flow (Ar)	0.8 L min^{-1}	0.8 L min^{-1}	0.9 L min^{-1}
Auxiliary gas flow (Ar)	0.3 L min^{-1}	0.7 L min^{-1}	–
Collision gas (He)	3.0 mL min^{-1}	–	2.0 mL min^{-1}
Internal standard	^{103}Rh	^{103}Rh	^{29}Si
Isotopes measured	^{27}Al, ^{47}Ti, ^{52}Cr, ^{59}Co, ^{60}Ni, ^{63}Cu, ^{88}Sr, ^{89}Y, ^{90}Zr, ^{184}W	^{55}Mn, ^{56}Fe	^{27}Al, ^{47}Ti, ^{52}Cr, ^{55}Mn, ^{56}Fe, ^{59}Co, ^{60}Ni, ^{63}Cu, ^{88}Sr, ^{89}Y, ^{90}Zr, ^{184}W

5.2.2. Calculation of ablated amounts and sampled amounts

Ablated amounts were calculated from the size of the ablation track form and the signal intensity of ^{29}Si. The ablated area and the ablated depth of the single-crystal SiC were 3.0 × 10^{-4} cm^2 and 1.6 × 10^{-3} cm, respectively. The ablated amount of the single-crystal SiC was 0.0015 mg, which was calculated by multiplying the density of SiC (3.21 g cm^{-3}) by the track volume of the single-crystal SiC. The depth of pressed powder samples and sintered SiC could not be measured accurately, because the sample surface was too rough. The signal intensity of ^{29}Si is related to the ablated amount of a sample. Ablated amounts of pressed powder samples and sintered SiC were calculated from Eq (1) under the assumption that the transportation efficiency of ablated particles was constant regardless of the ablated amount:

$$\text{Ablated amount}_{sp} = \frac{a \times \sum I_{\text{Si in sp}}}{\sum I_{\text{Si in crystal}}} \qquad \text{Eq (1)}$$

where a is the ablated amount of the single-crystal SiC, $\Sigma I_{\text{Si in sp}}$ is the integrated signal intensity of ^{29}Si in a sample, and $\Sigma I_{\text{Si in crystal}}$ is the integrated signal intensity of ^{29}Si in single-crystal SiC. The ablated amounts of NMIJ 8001a, NMIJ 8002a, and sintered SiC were 0.011, 0.0061, and 0.0023 mg, respectively.

For LAL-ICPMS, the sampled amounts of the sintered SiC and the single-crystal SiC were measured with a microbalance (MT5, Mettler Toledo, Zurich, Switzerland). The amounts of ablated particles were calculated from the difference between the weights of the sample before and after LAL sampling. The sampled amounts of the sintered SiC and single-crystal SiC were 0.23 and 0.19 mg, respectively.

5.2.3. Reagents

Hydrofluoric acid (25 M, Daikin Industries, Osaka, Japan), HNO_3 (ultrapure, 11 M, Kanto

Chemical, Tokyo, Japan), and H_2SO_4 (ultrapure, 18 M, Kanto Chemical, Tokyo, Japan) were used for acid digestion. Calibration standard solutions were prepared from the following SPEX CertiPrep (Metuchen, NJ, USA) multielement standards for ICPMS: XSTC-7, XSTC-8, and XSTC-13. The standards were diluted with 0.1 M HNO_3. Calibration curves were prepared by measuring standard solutions at concentrations of 0, 5, 10, 100, 500, and 5000 pg mL^{-1}.

5.2.4. Sample preparation

For LA-ICPMS, disk-shaped pellets were prepared by pressing 300 mg of each of the following SiC powder CRMs under a pressure of 10 MPa for 60 s: NMIJ 8001a, NMIJ 8002a, JCRM R021, JCRM R022, and JCRM R023. The diameter and height of the resulting pellets were 10 and 2 mm, respectively. Photographs of the sintered SiC and the single-crystal SiC samples are shown in Fig. 5-1a and 5-1b, respectively.

Two open-top chambers made of a tetrafluoroethylene–perfluoroalkyl vinyl ether copolymer (PFA) were used for LAL sampling. The outer diameter, inner diameter, and height of the chamber used for the sintered SiC were 32, 36, and 10 mm, respectively. The outer diameter, inner diameter, and height of the chamber used for the single-crystal SiC were 52, 60, and 7 mm, respectively. Each sample was placed in the specified chamber, and then 5.6 mL (for the sintered SiC) or 6.4 mL (for the single-crystal SiC) of ultrapure water (>18.2 MΩ cm, Milli-Q, Merck Millipore, Darmstadt, Germany) was added; as a result, the surface of the sample was 3 mm below the surface of the water. The sample surface was irradiated through the water. Forty laser lines, each 2 mm long, were cut at 100-μm intervals. The line width was 100 μm, the laser energy on the sample surface was 0.9 mJ, the laser frequency was 20 Hz, and the scanning speed was 10 μm s^{-1}.

After the ablation, the LAL-sampled particles suspended in the water were transferred to a polytetrafluoroethylene (PTFE) pressure vial by micropipette. In order to collect the ablated particles completely, 1 mL of ultrapure water was added in the chamber additionally, and then it was transferred to the PTFE pressure vial.

The LAL-sampled particles of the sintered SiC and the single-crystal SiC were submitted to high-pressure-acid digestion with a mixture of 2 mL of HF, 4 mL of HNO_3, and 1 mL of H_2SO_4 in the pressure vial, which was placed in a stainless steel jacket (HU-50, San-ai Kagaku, Aichi, Japan) and the stainless steel jacket was heated for 24 h in an oven at 210 °C. After high-pressure acid digestion, the digested solution was evaporated on a hot plate; heating was continued until the digested solution was reduced to a single droplet, which was diluted to 2 mL with 0.1 M HNO_3. The concentration of H_2SO_4 had to be adjusted to less than 1% for analysis by ICPMS because elemental interference by S cannot be corrected accurately when the H_2SO_4 concentration is above 1%.

Approximately 1 mg of the SiC powders (NMIJ 8001a and NMIJ 8002a) was weighed out and subjected to high-pressure acid digestion with same procedures as LAL-sampled particles. Sintered SiC was cracked with a hammer, and about 10 mg of the sample was weighed and then also subjected to high-pressure acid digestion except conducted for 96 h in an oven at 210 °C.

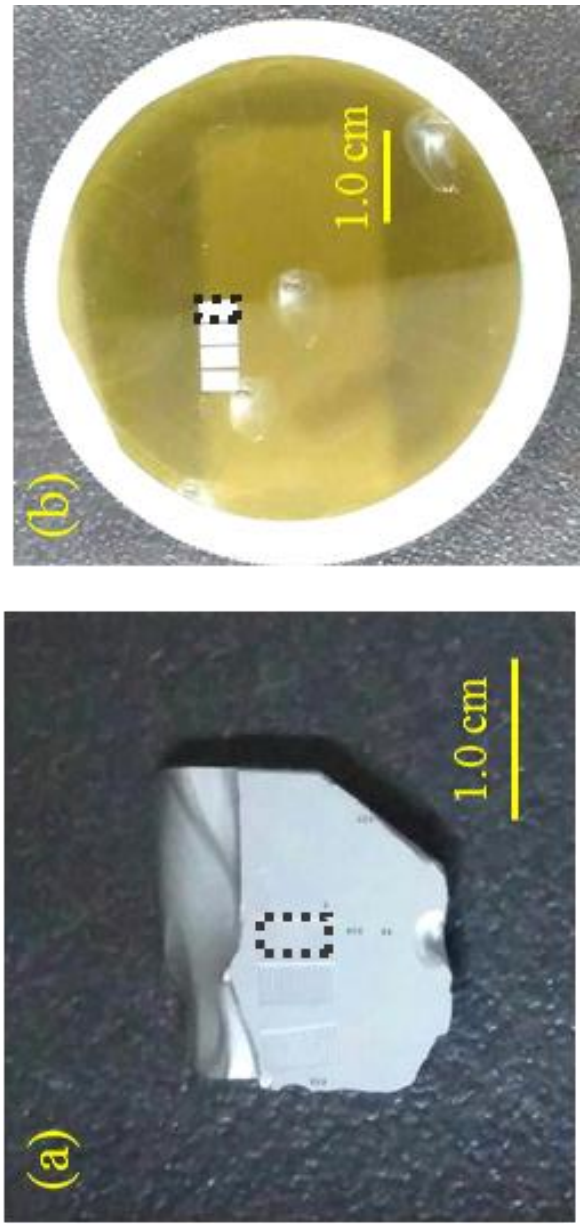

Fig. 5-1 Photographs of (a) sintered SiC and (b) single-crystal SiC (b). Dotted lines indicate LAL-sampling areas (0.2 mm by 0.4 mm).

5.3. Results and discussion

5.3.1. SEM observation of LAL-sampled particles

SiC powder (NMIJ 8002a) and LAL-sampled particles were put on a silicon wafer for SEM observation at a magnification of 5000× (Fig. 5-2). SEM indicated that the diameters of the NMIJ 8002a particles ranged from 0.1 to 2.0 μm (Fig. 5-2a). Sintered SiC particles sampled by LAL gave spherical and edge-shaped particles were observed among the LAL-sampled particles obtained from sintered SiC (Fig. 5-2b), whereas single-crystal SiC particles sampled by LAL gave mainly spherical particles (Fig. 5-2c). The diameters of the LAL-sampled particles of the sintered SiC and single-crystal SiC ranged from 0.1 to 5.0 μm. The spherical particles were likely generated in the heat effective zone resulting from the interaction between the sample surface and the laser beam, and the edge-shaped particles were generated mechanically by the laser-induced plasma shock wave.

LAL sampling has two advantages: it creates particles with dimensions smaller than several micrometers, and it changes the particle characteristics as a result of the melting–congelation process that occurs in the heat effective zone on the sample surface. The particles are transformed from hard-to-digest crystals to a soluble, spherical form. Therefore, sintered SiC and single-crystal SiC particles collected by LAL sampling can easily be decomposed by high-pressure acid digestion.

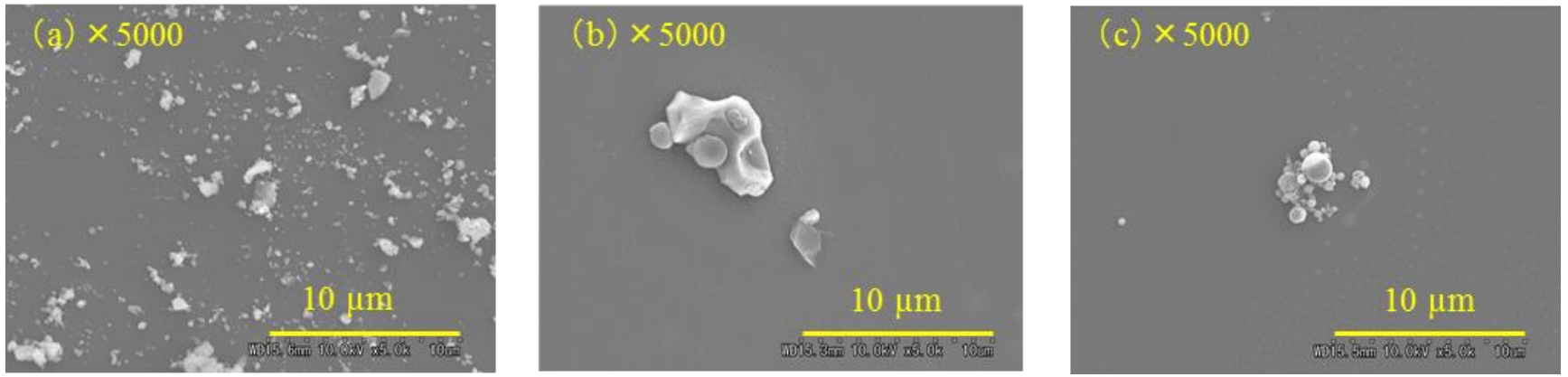

Fig. 5-2 SEM images of (a) commercially available SiC powder (NMIJ 8002a) without pretreatment, (b) sintered SiC particles collected by LAL-sampling, and (c) single-crystal SiC particles collected by LAL-sampling.

5.3.2. Analysis of NMIJ 8001a and NMIJ 8002a CRMs

The NMIJ 8001a and NMIJ 8002a CRMs were analyzed by means of LA-ICPMS and ICPMS with acid digestion. For LA-ICPMS, the integrated signal intensities of the elements were normalized by the integrated signal intensity of ^{29}Si, because the amounts ablated from different samples depended on the interaction between the laser light and the sample surface. LA was carried out for 30 s in line-scanning mode. LA-ICPMS was performed in time-resolved analysis mode, and element concentrations were calculated with Eq (2):

$$[\mathrm{M}] = \frac{(\sum I_{\mathrm{M}} / \sum I_{\mathrm{Si}}) - b}{s} \qquad \text{Eq (2)}$$

where [M] is the concentration of an element in the sample, ΣI_{M} is the integrated signal intensity of the element during laser ablation, ΣI_{Si} is the integrated signal intensity of ^{29}Si during laser ablation, s is the sensitivity for element M, and b is an intercept of the calibration curve.

For ICPMS with acid digestion, a standard solution was used for calibration. ICPMS was performed in spectrum analysis mode. Measured concentrations and recoveries of the elements are listed in Table 5-3. In the case of LA-ICPMS, the elements Co, Cu, Sr, Y, and W could not be quantified by LA-ICPMS, because their concentrations in the JCRM CRMs were not certified (Table 5-1). The measured concentrations of Al, Ti, Cr, Fe, and Ni in NMIJ 8001a and NMIJ 8002a were in good agreement with the certified values. The recoveries of these elements were 100% ± 20%. The recoveries of Mn for NMIJ 8001a and NMIJ 8002a were 74% and 69%, respectively. The concentration of Mn was quantified by means of a one-point calibration curve using JCRM R022, because the concentrations of Mn in JCRM R021 and JCRM R023 were not certified (Table 5-1). Therefore, the calibration curve of Mn has less reliability compared with other elements.

In the case of ICPMS with acid digestion, the recoveries of all measured elements were 100% ± 20%. The measured concentrations of Mn and Cu in NMIJ 8002a varied by 2% and 5%, respectively. However, the recoveries of Mn and Cu were 81% and 88%, respectively. These recoveries were worse than those of other elements. In contrast, the certified values of Mn and Cu in NMIJ8002a varied by 21% and 22%, respectively. We suggest that the worse recoveries for Mn and Cu were related to the variation of the concentrations in different sample lots. The recoveries of Ti, Mn, Fe, and Ni from NMIJ 8001a obtained by means of ICPMS with acid digestion were 100%, which was better than the recoveries obtained by means of LA-ICPMS. These results indicate that LA-ICPMS analysis is a useful technique for quantitative analysis of SiC powder without sample pretreatment. However, this technique is not appropriate when the concentration of an element is not certified in the CRMs.

Table 5-3 Analysis of SiC CRMs (NMIJ 8001a and NMIJ 8002a)

	NMIJ 8001a				NMIJ 8002a			
	LA-ICPMS		Acid digestion ICPMS		LA-ICPMS		Acid digestion ICPMS	
	Caliblated by JCRM CRMs*		Solution calibration		Caliblated by JCRM CRMs*		Solution calibration	
	Ablated amount: 0.011 mg		Sampling amount: 1.5 mg		Ablated amount: 0.0061 mg		Sampling amount: 1.0 mg	
Element	Found ($\mu g\ g^{-1}$)	Recovery (%)	Found ($\mu g\ g^{-1}$)	Recovery (%)	Found ($\mu g\ g^{-1}$)	Recovery (%)	Found ($\mu g\ g^{-1}$)	Recovery (%)
Al	79.8 ± 0.6 (1)	96	81.7 ± 0.8 (1)	98	184 ± 2.9 (2)	97	183 ± 2.1 (1)	97
Ti	7.3 ± 0.2 (2)	114	6.6 ± 0.4 (6)	103	56 ± 3.4 (6)	118	47.8 ± 3.2 (7)	100
Cr	2.0 ± 0.1 (4)	101	1.91 ± 0.2 (8)	96	62.3 ± 1.4 (2)	101	61.6 ± 1.4 (3)	100
Mn	0.39 ± 0.005 (1)	74	0.53 ± 0.05 (9)	100	1.1 ± 0.1 (11)	69	1.3 ± 0.02 (2)	81
Fe	47.5 ± 0.3 (1)	102	46.5 ± 1.5 (3)	99	119 ± 6.6 (6)	92	126 ± 3.9 (3)	97
Co	-	-	0.03 ± 0.002 (8)	-	-	-	0.15 ± 0.01 (7)	-
Ni	1.7 ± 0.1 (8)	110	1.50 ± 0.05 (3)	99	4.32 ± 0.8 (18)	97	4.31 ± 0.1 (2)	97
Cu	-	-	0.51 ± 0.1 (12)	108	-	-	10.1 ± 0.5 (5)	88
Sr	-	-	0.02 ± 0.01 (40)	-	-	-	0.04 ± 0.02 (43)	-
Y	-	-	0.33 ± 0.03 (8)	107	-	-	0.54 ± 0.01 (1)	92
Zr	0.31 ± 0.01 (5)	-	0.28 ± 0.02 (6)	-	16 ± 0.6 (4)	-	9.2 ± 0.1 (1)	-
W	-	-	0.30 ± 0.02 (6)	-	-	-	10.6 ± 0.4 (1)	-

* JCRM R021, JCRM R022, and JCRM R023

* The value in parentheses indicates the %RSD (n=3).

5.3.3. Analysis of sintered SiC and single-crystal SiC

The surface layer of the sintered SiC was analyzed by means of LA-ICPMS and LAL-ICPMS. The NMIJ CRMs were used as standard reference materials for LA-ICPMS. Because the certified values for the NMIJ CRMs may have varied with the sample lot, we used the concentrations of elements in the NMIJ CRMs obtained by acid digestion ICPMS in this study (Table 5-3) for calibration. For comparison with the surface layer analyses, the sintered SiC was cracked into fine bulk particles (<1.0 mm) with a hammer, and the bulk particles were analyzed by means of acid digestion ICPMS.

Quantitative data for the elements in the sintered SiC determined by means of the three analytical methods are summarized in Table 5-4. The concentrations of Al, Ti, and Cr determined by surface layer analysis were in good agreement (within 25%) for LA-ICPMS and LAL-ICPMS.

The concentrations of Fe and Ni obtained by LA-ICPMS were higher than those obtained by LAL-ICPMS, and those of Y and Zr obtained by LA-ICPMS were lower than those obtained by LAL-ICPMS. However, the concentrations of these four elements determined by these two techniques were on the same order of magnitude. The amounts ablated from the NMIJ CRMs were 5 times the amount ablated from sintered SiC. When the ablated amount was taken into account, the signal intensities of the elements decreased with increasing ablated amount owing to the mass loading effect in the ICP.[31] The signal intensities of Fe and Ni were reduced to a greater extent than the signal intensity of Si. Therefore, the intensities of Fe and Ni normalized by the internal standard element (Si) were smaller than the true normalized intensities. The normalized intensities of Fe and Ni in the NMIJ CRMs were reduced to a greater extent than were the normalized intensities of Fe and Ni in the sintered SiC. The concentrations of Fe and Ni in the sintered SiC were

overestimated.

The data for bulk cracked SiC can be taken as the average concentrations of impurities in sintered SiC. Comparison of the impurities in the surface layer as measured by LAL-ICPMS and the impurities in the bulk cracked SiC indicated that the data obtained by LAL-ICPMS were not as precise as than those obtained by acid digestion ICPMS. This difference was due to the fact that the sampled amount obtained by LAL-ICPMS was smaller than that obtained by acid digestion ICPMS. The concentrations of Al, Ti, Cr, and Fe could be higher than those of other elements. Al, Ti, Cr, and Fe are known to be present in the raw materials used to prepare the SiC powder. It is believed that many of the elements were present as a result of contamination from graphite susceptors and thermal insulation materials used to a growth furnace for sintering SiC powders.[43,96]

The surface layer and bulk data for Ti, Cr, Fe, Co, Ni, Sr and W were in good agreement, indicating that these elements were homogeneously distributed in the sintered SiC. In contrast, the concentrations of Al, Mn, Cu, Y, and Zr in the surface layer were higher than the concentrations in the bulk. Depth profiles of Al, Y, and Zr in sintered SiC are shown in Fig. 5-3. The depth profiles were obtained by LA-ICPMS under single-site mode. Aluminum was enriched in the range of about 30 μm depth from the sample surface. Y and Zr were enriched in the range of about 5 μm depth from the sample surface. The trend of elemental enrichment was the same as that of elemental concentrations shown in Table 5-4. Depth profiles of Mn and Cu could not be obtained by LA-ICPMS because the concentrations of these elements were too low to detect.

Table 5-4 Surface layer analysis and bulk analysis of sintered SiC

Sampling area	Surface		Surface		Bulk cracked SiC	
	LA-ICPMS		LAL-ICPMS		Acid digestion ICPMS	
	Ablated amount: 0.0023 mg		Sampling amount: 0.23 mg		Sampling amount: 13.5 mg	
	Caliblated by NMIJ CRMs*		Solution calibration		Solution calibration	
Element	Found ($\mu g\ g^{-1}$)		Found ($\mu g\ g^{-1}$)		Found ($\mu g\ g^{-1}$)	
Al	518 ± 16	(3)	460 ± 35	(8)	261 ± 6	(2)
Ti	146 ± 12	(8)	193 ± 25	(13)	204 ± 11	(5)
Cr	38 ± 3.0	(8)	32 ± 1.2	(4)	38 ± 2.7	(7)
Mn	< 3		0.4 ± 0.08	(22)	0.07 ± 0.003	(5)
Fe	162 ± 10	(6)	100 ± 11	(11)	118 ± 10	(8)
Co	< 1	(9)	1.1 ± 0.2	(19)	1.3 ± 0.1	(6)
Ni	37 ± 3	(8)	24 ± 3.4	(14)	30 ± 1.9	(6)
Cu	< 2		0.5 ± 0.06	(12)	0.05 ± 0.02	(41)
Sr	< 0.5		0.17 ± 0.02	(9)	0.16 ± 0.01	(9)
Y	1.2 ± 0.2	(19)	5.4 ± 0.7	(13)	0.4 ± 0.04	(10)
Zr	40 ± 6.2	(15)	98 ± 2.5	(3)	29 ± 2.5	(9)
W	< 1		0.48 ± 0.07	(14)	0.35 ± 0.03	(10)

* NMIJ 8001a and NMIJ 8002a

* The value in parentheses indicates the %RSD (n=3).

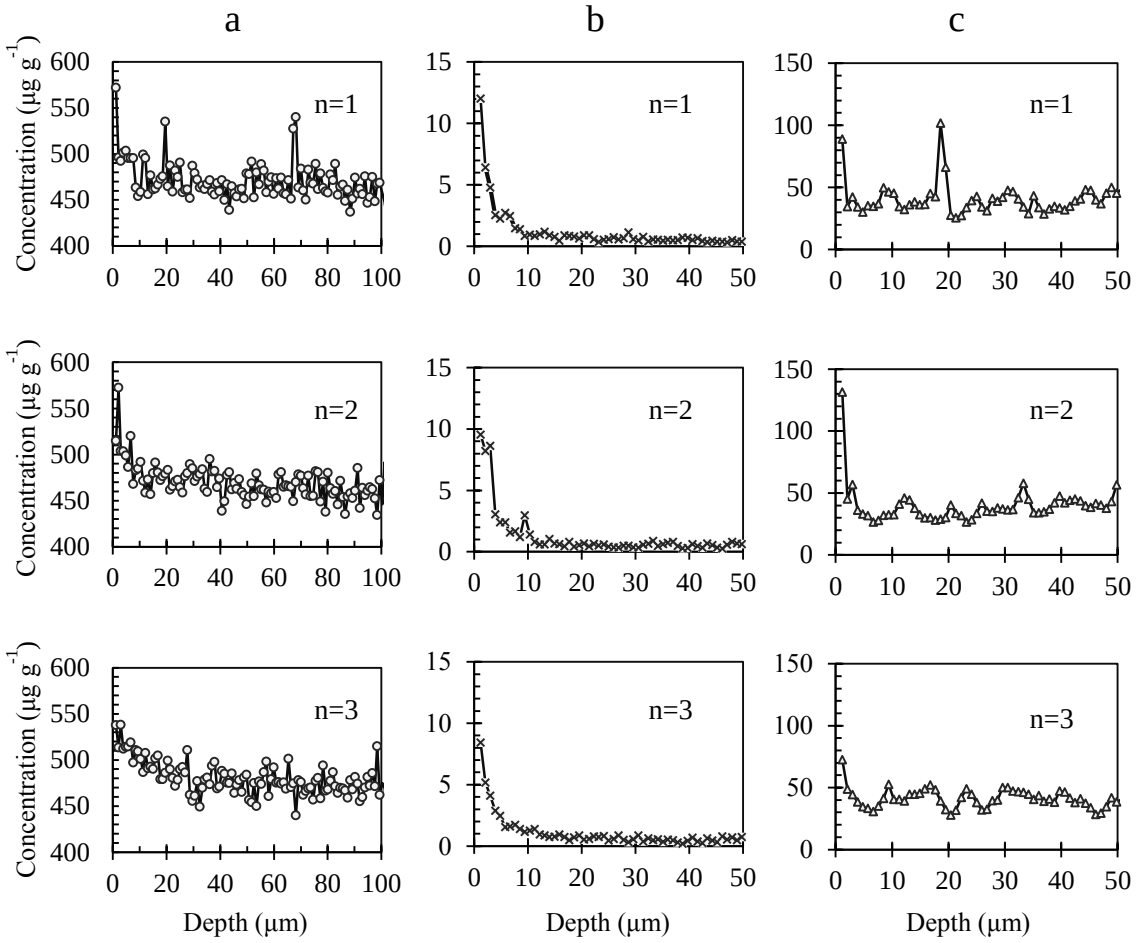

Fig. 3 Depth profiles of Al(a), Y(b), and Zr(c) in sintered SiC were obtained by LA-ICPMS under single-site mode. LA-ICPMS measurements were repeated three times.

Element concentrations and corresponding LOQs in the single-crystal SiC for LA- and LAL-ICPMS are summarized in Table 5-5. The LOQ was calculated as 10 times the standard deviation of repeated measurements of an operation blank (n = 5). The concentrations of all the measured elements in the single-crystal SiC were lower than the measured concentrations in the sintered SiC (Table 5-4). Semiconductor-grade single-crystal SiC is made by means of chemical vapor deposition epitaxy, which allows the synthesis of high-purity SiC substrates because pure gases are available to use. Using LA-ICPMS analysis, we were able to determine the Al and Ti concentrations in the single-crystal SiC, but the concentrations of the other elements were below the LOQ.

The Al concentration obtained by LA-ICPMS was lower than that obtained by LAL-ICPMS. The accuracy may have been reduced because the measured value was much lower than the calibration range. In contrast, the Ti concentrations obtained by LA- and LAL-ICPMS were in good agreement, and the determined Ti concentration was within the calibration range. Using LAL-ICPMS analysis, the LOQs of the elements ranged from 0.1 to 1.0 μg g^{-1}. We were able to determine the concentrations of Al, Ti, Cr, Mn, Fe, Ni, Cu, and Zr in the single-crystal SiC. To quantify Co, Sr, Y, and W, we will need to increase the sampled amount by using a longer laser ablation time to improve the LOQ.

The purity of the surface layer of sintered SiC and single-crystal SiC is very important for semiconductor power device manufacturing. Our results demonstrate that LA-ICPMS is a useful technique for quantification of elements present at concentrations high enough to be determined. Moreover, LAL-ICPMS is an appropriate analytical technique for evaluation of surface purity.

Table 5-5 Surface layer analysis of single-crystal SiC, and limit of quantification of different analytical method.

	LA-ICPMS		LAL-ICPMS	
	Ablated amount: 0.0015 mg		Sampling amount: 0.19 mg	
	Caliblated by NMIJ CRMs*		Solution calibration	
Element	Found ($\mu g\ g^{-1}$)	LOQ ($\mu g\ g^{-1}$)	Found ($\mu g\ g^{-1}$)	LOQ ($\mu g\ g^{-1}$)
Al	6 ± 1 (17)	5	22 ± 0.89 (4)	0.5
Ti	13 ± 5 (36)	5	19 ± 3.3 (18)	1.0
Cr	< 3	3	0.4 ± 0.06 (14)	0.4
Mn	< 3	3	0.2 ± 0.02 (9)	0.1
Fe	< 18	18	5.3 ± 0.9 (17)	0.5
Co	< 1	1	< 0.1	0.1
Ni	< 5	5	0.7 ± 0.1 (15)	0.2
Cu	< 2	2	3.3 ± 0.3 (8)	0.4
Sr	< 0.5	0.5	< 0.1	0.1
Y	< 0.5	0.5	< 0.2	0.2
Zr	< 1	1	1.1 ± 0.2 (18)	0.2
W	< 1	1	< 0.2	0.2

* NMIJ 8001a and NMIJ 8002a

* The value in parentheses indicates the %RSD (n=3).

5.4. Summary

In this study, we evaluated the use of LA-ICPMS and LAL-ICPMS for the determination of trace elements in SiC powders (NMIJ CRMs), sintered SiC, and single-crystal SiC. LA-ICPMS was found to be useful for quantitative analysis without sample pretreatment. The reliability of the data obtained by LA-ICPMS was reduced when the concentration of an element in a sample was outside the range of the calibration curve prepared by analysis of the CRMs. If the concentration of an element was not certified in the CRMs, the elements in the CRMs had to be determined by a reliable analytical method such as ICPMS with acid digestion.

It is impossible to locally decompose the surface layer of hard-to-digest samples such as sintered SiC and single-crystal SiC. We found that LAL sampling is a useful technique for microparticulation of samples, and this technique allowed us to arbitrarily change the sampling area (2 mm by 4 mm) in accordance with the purpose of the analysis. On the basis of our analysis of the impurities in the surface layer of sintered SiC and bulk cracked SiC, we suggest that possible sources of contamination include raw materials, graphite susceptors, thermal insulation materials, surface polishing materials, and cutting blades.

For the analysis of single-crystal SiC, a highly sensitive method is required. The LOQs of LA-ICPMS and LAL-ICPMS were 0.5-18 μg g^{-1} and 0.1-1.0 μg g^{-1}, respectively. We demonstrated that LAL-ICPMS could be used for evaluation of sintered SiC and semiconductor-grade single-crystal SiC. Moreover, increasing the sampled amount by increasing the LAL-sampling time can be expected to improve the LOQs.

Although LAL-ICPMS must be investigated further for use in situations in which high sensitivity and throughput are required, this technique should become a powerful

tool for semiconductor power device manufacturing. LAL-ICPMS can be used to determine trace elements without CRMs.

Chapter 6

Concluding remarks and future prospects

Chapter 6 Concluding remarks and future prospects

In this study, we succeeded to explain elemental fractionation by temporal changes of size distribution and elemental properties. The elements Ag, As, Se, Sb, Ga, Te, Bi, Pb, Cd, Re, Sn, Cu, W, and Zn were classified in Group 1. A remarkable peak of FI was observed at 2-3 min after the start of ablation under 0.5 mm defocus and 1.0 mm defocus conditions. Ablated particles larger than 0.22 μm could not be decomposed completely when the ablated particles were introduced into the ICP. Whereas the elements in Group 1 were more easily vaporized and ionized than Ca. On the other hand, volatile elements were enriched in ablated particles smaller than 0.22 μm during laser ablation regardless of the focus conditions. The magnitude of the enrichment increased as the aspect ratio of the crater increased. However, the magnitude of the enrichment at 0-1 min after the start of ablation was the same as that at 1-5 min after the start of ablation. For non-volatile elements (Group 2), temporal changes of FIs were constant when laser ablation progressed regardless of the size of ablated particles.

In the case of LAL sampling, both positive and negative elemental fractionation occurred. The volatile elements were depleted in the larger particles and enriched in the smaller particles. If all of the LAL-sampled particles were collected in the liquid and analyzed by ICPMS with acid digestion, the elements in samples were able to be determined with high reliability. It was indicated that LAL sampling was a useful technique for quantitative analysis.

A sintered SiC and a single-crystal SiC were analyzed by LA-ICPMS and LAL-ICPMS. LA-ICPMS analysis was a useful analytical technique without sample pretreatment. In order to perform accurate analysis, CRMs that have a similar matrix to the sample have to be prepared for calibration. In addition, target elements in CRMs need

to be certified, and signal intensities of elements should be corrected for by an internal standard. LAL-ICPMS was able to quantify trace elements in surface layer of sintered SiC and single-crystal SiC. Although LAL-ICPMS needs further investigation for high sensitivity and throughput, this technique should become a powerful tool for semiconductor power device manufacturing. The quantitative analysis with high accuracy and high precision by using the solution calibration is the greatest characteristic of LAL-ICPMS. It could be able to determine certified values for laboratory-made CRMs.

LA has been studied as a hyphenated technique for trace element analysis for solid samples, but we are considering that the LA is the sampling process, not the analysis. We believe that LA will be widely used to any other fields as a new sampling technique for spatial analysis.

References

1. T. H. Maiman, *Nature*, 1960, **187**, 493-494.

2. R. S. Houk, V. A. Fassel, G. D. Flesch, H. J. Svec, A. L. Gray and C. E. Taylor, , *Anal. Chem.*, 1980, **52**, 2283-2289.

3. A. L. Gray, *ANALYST*, 1985, **10**, 551-556.

4. J. S. Becker and H. Dietze, Int. *J. Mass. Spectrom.*, 2003, **228**, 127-150.

5. J. Pisonero, B. Fernández and D. Günther, *J. Anal. At. Spectrom.*, 2009, **24**, 1145-1160.

6. D. Tabersky, K. Nishiguchi, K. Utani, M. Ohata, R. Dietiker, M. B. Fricker, I. M. de Maddalena, J. Kocha and D. Günther, *J. Anal. At. Spectrom.*, 2013, **28**, 831-842.

7. M. Guillong, I. Horn and D. Günther, *J. Anal. At. Spectrom.*, 2003, **18**, 1224-1230.

8. A. M. Duffin, G. L. Hart, R. C. Hanlen and G. C. Eiden, *J. Radioanal. Nucl. Chem.*, 2013, **296**, 1031-1036.

9. F. Claverie, B. Fernández, C. Pécheyran, J. Alexis and O. F. X. Donard, *J. Anal. At. Spectrom.*, 2009, **24**, 891-902.

10. S. Okabayashi, T. D. Yokoyama, Y. Kon, S. Yamamoto, T. Yokoyama and T. Hirata, *J. Anal. At. Spectrom.*, 2011, **26**, 1393-1400.

11. M. S. A. Horstwood, G. L. Foster, R. R. Parrish, S. R. Noble and G. M. Nowell, *J. Anal. At. Spectrom.*, 2003, **18**, 837-846.

12. C. Pickhardt, J. Sabine and B. H. Dietze, Fresenius *J. Anal. Chem.*, 2000, **368**, 173-181.

13. S. Kappel, S. F. Boulyga, L. Dorta, D. Günther, B. Hattendorf, D. Koffler, G. Laaha, F. Leisch and T. Prohaska, *Anal Bioanal Chem.*, 2013, **405**, 2943-2955.

14. J. T. van Elteren, A. Izmer, M. Šala, E. F. Orsega, V. S. Šelih, S. Panighello and F. Vanhaecke, *J. Anal. At. Spectrom.*, 2013, **28**, 994-1004.

15. M. Ohata, H. Yasuda, Y. Namai and N. Furuta, *Anal. Sci.*, 2002, **18**, 1105-1110.

16. A. M. Leacha and G. M. Hieftje, *J. Anal. At. Spectrom.*, 2000, **15**, 1121-1124.

17. H. R. Kuhn and D. Günther, *J. Anal. At. Spectrom.*, 2006, **21**, 1209-1213.

18. C. O' Connor, B. L. Sharp and P. Evans, *J. Anal. At. Spectrom.*, 2006, **21**, 556-565.

19. Ludwik Halicz and Detlef Günther, *J. Anal. At. Spectrom.*, 2004, **19,** 1539-1545.

20. N. Furuta, *Appl. Spectrosc.*, 1991, **45(8)**, 1372-1376.

21. M. Ohata, D. Tabersky, R. Glaus, J. Koch, B. Hattendorf and D. Günther, *J. Anal. At. Spectrom.*, 2014, **29,** 1345-1353.

22. D. Güntherr and C. A. Heinrichb, *J. Anal. At. Spectrom.*, 1999, **13**, 1369-1374.

23. C. Liu, X. L. Mao, S. S. Mao, X. Zeng, R. Greif and R. E. Russo, *Anal. Chem.*, 2004, **76**, 379-383.

24. T. Hirata and Y. Kon, *Anal. Sci.*, 2008, **24**, 345-353.

25. H. R. Kuhn, M. Guillong and D. Günther, *Anal Bioanal Chem.*, 2004, **378**, 1069-1074.

26. Z. Wang, D. Qiu, Z. Ni, G. Tao and P. Yang, *Anal. Chim. Acta*, 2006, **577**, 288-294.

27. M. Ohata and N. Furuta, *Anal. Sci.*, 2004, **20**, 701-706.

28. L. Fornarini, V. Spizzichino, F. Colao, R. Fantoni and V. Lazic, *Anal. Bioanal. Chem.*, 2006, **385**, 272-280.

29. M. Guillong and D. Günther, *J. Anal. At. Spectrom.*, 2002, **17**, 831-837.

30. Z. Wang, B. Hattendorf and D. Günther, *J. Am. Soc. Mass Spectrom.*, 2006, **17**, 641-651.

31. I. Kroslakova and D. Günther, *J. Anal. At. Spectrom.*, 2007, **22**, 51-62.

32. R. Jäger, A. I. Saprykin, J. S. Becker, H. Dietze and J. A. C. Broekaert, *Mikrochim. Acta*, 1997, **125**, 41-44.

33. Y. Kataoka, K. Yamazaki, M. Shigeno, Y. Tada and K. Wittmaack, *Appl. Surf. Sci.*, 2003, **203-204**, 43-47.

34. Y. Tada, K. Suzuki and Y. Kataoka, *Appl. Surf. Sci*., 2008, **255**, 1320-1322.

35. G. Compagnini, A. A. Scalisi and O. Puglisi, *J. Appl. Phys.*, 2003, **94**, 7874-7877.

36. O. R. Musaev, A. E. Midgley, J. M. Wrobel and M. B. Kruger, *Chemical Physics Letters*, 2010, **487**, 81-83.

37. V. Amendola and M. Meneghetti, *Chem. Phys.*, 2013, **15**, 3027-3046.

38. D. N. Douglas, J. L. Crisp, H. J. Reid and B. L. Sharp, *J. Anal. At. Spectrom.*, 2011, **26**, 1294-1301.

39. H. Okumura, *Jpn. J. Appl. Phys.*, 2006, **45**, 7565-7586.

40. H. Tanaka, *J. Ceram. Soc. Jpn*., 2011, **119**, 218-233.

41. H. Matsunami, *Jpn. J. Appl. Phys.*, 2004, **43**, 6835-6847.

42. U. Schäffer and Viliam Krivan, *Anal. Chem.*, 1999, **71**, 849-854.

43. J. C. Viala, F. Bosselet, V. Laurent and Y. Lepetitcorps, *J. Mater. Sci.*, 1993, **28**, 5301-5312.

44. M. Franek and V. Krivan, *Fresenius' J. Anal. Chem.*, 1992, **342**, 118-124.

45. P. Barth and V. Krivan, *J. Anal. At. Spectrom.*, 1994, **9**, 773-776.

46. A. Besmehn and P. Hoppe, *Geochim. Cosmochim. Acta*, 2003, **67**, 4693-4703.

47. Y. M. Tairov and V. F. Tsvetkov, *J. Crystal Growth*, 1982, **52**, 146-150.

48. R. E. Russo, X. Mao, J. J. Gonzalez, V. Zorba and J. Yoo, *Anal. Chem.*, 2013, **85**, 6162-6177.

49. H. P. Longerich, D. Günther and S. E. Jackson, *Fresenius' J. Anal. Chem.*, 1996,

355, 538-542.

50. B. J. Fryer, S. E. Jackson and H. P. Longerich, *Can. Mineral.*, 1995, **33**, 303-312.
51. T. E. Jeffries, S. E. Jackson and H. P. Longerich, *J. Anal. At. Spectrom.*, 1998, **13**, 935-940.
52. I. Rodushkin, M. D. Axelsson, D. Malinovsky and D. C. Baxter, *J. Anal. At. Spectrom.*, 2002, **17**, 1223-1230.
53. K. P. Jochum, B. Stoll, K. Herwig and M. Willbold, *J. Anal. At. Spectrom.*, 2007, **22**, 112-121.
54. Q. Z. Bian, J. Koch, H. Lindner, H. Berndt, R. Hergenröder and K. Niemax, *J. Anal. At. Spectrom.*, 2005, **20**, 736-740.
55. A. Kate Souders and Paul J. Sylvester, *J. Anal. At. Spectrom.*, 2010, **25**, 975-988.
56. J. Koch, A. von Bohlen, R. Hergenröder and K. Niemax, *J. Anal. At. Spectrom.*, 2004, **19**, 267-272.
57. Y. R. Luo and J. A. Kerr, in "CRC Handbook of Chemistry and Physics", ed. D. R. Lide, 86th ed., 2005, Taylor & Francis, New York, Chap. 9, 54.
58. R. Machida, T. Nakazawa and N. Furuta, *Anal. Sci.*, 2015, **31**, 345-355.
59. R. E. Russo, X. Mao, H. Liu, J. Gonzalez and S. S. Mao, *Talanta*, 2002, **57**, 425-451.
60. M. Ohata, D. Tabersky, R. Glaus, J. Koch, B. Hattendorf and D. Günther, *J. Anal. At. Spectrom.*, 2014, **29**, 1345-1353.
61. O. V. Borisov, X. Mao and R. E. Russo, *Spectrochim. Acta, Part B*, 2000, **55**, 1693-1704.
62. R. Hergenröder, *J. Anal. At. Spectrom.*, 2006, **21**, 505-516.
63. H. R. Kuhn and D. Günther, *J. Anal. At. Spectrom.*, 2004, **19**, 1158-1164.

64. R. Machida, T. Nakazawa, Y. Sakuraba, M. Fujiwara and N. Furuta, *J. Anal. At. Spectrom.*, 2015, **30**, 2412-2419.

65. J. O'Reilly, D. Douglas, J. Braybrook, P. So, E. Vergucht, J. Garrevoet, B. Vekemans, L. Vinczec and H. G. Infante, *J. Anal. At. Spectrom.*, 2014, **29**, 1378-1384.

66. H. Zhou, Z. Wanga, Y. Zhu, Q. Li, H. Zou, H. Qu, Y. Chen and Y. Du, *Spectrochim. Acta, Part B*, 2013, **90**, 55-60.

67. M. Tibi and K. G. Heumann, *J. Anal. At. Spectrom.*, 2003, **18**, 1076-1081.

68. Y. Zhu, A. Hioki and K. Chiba, *J. Anal. At. Spectrom.*, 2013, **28**, 301-306.

69. T. Do, H. Hsieh, W. Chang, E. Chang and C. Wang, *Spectrochim. Acta, Part B*, 2011, **66**, 610-618.

70. A. J. G. Mank and P. R. D. Mason, *J. Anal. At. Spectorm.*, 1999, **14**, 1143-1153.

71. V. Amendola and M. Meneghetti, *Adv. Funct. Mater.*, 2012, **22**, 353-360.

72. H. Wu, R. Yang, B. Song, Q. Han, J. Li, Y. Zhang, Y. Fang, R. Tenne and C. Wang, *ACS Nano*, 2011, **5**, 1276-1281.

73. V. Morandi, F. Marabelli, V. Amendola, M. Meneghetti and D. Comoretto, *J. Phys. Chem. C*, 2008, **112**, 6293-6298.

74. P. Liu, Y. Liang, X. Lin, C. X. Wang and G. Yang, *ACS Nano*, 2011, **5**, 4748-4755.

75. J. G. Williams, A. L. Gray, P. Normanut and L. Ebdon, *J. Anal. At. Spectrom.*, 1987, **2**, 469-472.

76. N. S. Mokgalaka, R. I. McCrindle and B. M. Botha, *J. Anal. At. Spectrom.*, 2004, **19**, 1375-1378.

77. N. S. Mokgalaka, T. Wondimu and R. I. McCrindle, *Bull. Chem. Soc. Ethiop.*, 2008, **22**, 313-321.

78. M. Aramendia, M. Resanob and F. Vanhaecke, *J. Anal. At. Spectrom.*, 2009, **24**, 41-50.

79. Z. Wang and P. Yang, *J. Anal. At. Spectrom.*, 2014, **29**, 2091-2103.

80. T. E. Itina, *J. Phys. Chem. C*, 2011, **115**, 5044-5048.

81. J. Koch, I. Feldmann, N. Jakubowski and K. Niemax, *Spectrochim. Acta, Part B*, 2002, **57**, 975-985.

82. D. B. Aeschliman, S. J. Bajic, D. P. Baldwin and R. S. Houk, *J. Anal. At. Spectrom.*, 2003, **18**, 872-877.

83. D. Tabersky, N. A. Luechinger, M. Rossier, E. Reusser, K. Hametner, B. Aeschlimann, D. A. Frick, S. C. Halim, J. Thompson, L. Danyushevsky and D. Günther, *J. Anal. At. Spectrom.*, 2014, **29**, 955-962.

84. F. Claverie, J. Malherbe, N. Bier, J. L. Molloy and S. E. Long, *Anal. Chem.*, 2013, **85**, 3584-3591.

85. S. F. Boulyga and K. G. Heumann, *Int. J. Mass Spectrom.*, 2005, **242**, 291-296.

86. C. Yang, P. Chi, Y. Lin, Y. Sun and M. Yang, *Talanta*, 2010, **80**, 1222-1227.

87. K. Wittmaack, *Surf. Interface Anal.*, 1998, **26**, 290-305.

88. M. P. McCann, W. F. Calaway, M. J. Pellin, I. V. Veryovkin, I. Constantinides, A. Adriaens and F. Adams, *Surf. Interface Anal.*, 2002, **33**, 394-400.

89. M. J. Whitehouse, Geostand. *Geoanal. Res.*, 2004, **28**, 195-201.

90. R. Matschat, J. Hinrichs and H. Kipphardt, *Anal. Bioanal. Chem.*, 2006, **386**, 125-141.

91. Y. Xing, L. Xiaojia and W. Haizhou, *Int. J. Mass. Spectrom.*, 2007, **262**, 25-32.

92. W. Vieth and J. C. Huneke, *Spectrochim. Acta*, 1991, **46B**, 137-153.

93. M. Kasik, C. Venzago and R. Dorka, *J. Anal. At. Spectrom.*, 2003, **18**, 603-611.

94. A. I. Saprykin, J. S. Becker and H.-J. Dietze, *Fresenius' J. Anal. Chem.*, 1999, **364**, 763-767.

95. Z. Wang, D. Qiu, Z. Ni, G. Tao and P. Yang, *Anal. Chim. Acta*, 2006, **577**, 288-294.

96. J. Nishio, M. Kushibe, K. Masahara, K. Kojima, T. Ohno, Y. Ishida, T. Takahashi, T. Suzuki, T. Tanaka, S. Yoshida and K. Arai, *Mat. Sci. Forum*, 2002, **389-393**, 215-218.

List of publications

[1] R. Machida, T. Nakazawa and N. Furuta.
Temporal changes of fractionation index caused by changes in the large size of ablated particles in laser ablation-inductively coupled plasma mass spectrometry.
Anal. Sci., 2015, **31**, 345-355. [Chapter 2]

[2] R. Machida, T. Nakazawa, Y. Sakuraba, M. Fujiwara and N. Furuta.
Particle size-related elemental fractionation in laser ablation in liquid inductively coupled plasma mass spectrometry.
J. Anal. At. Spectrom., 2015, **30**, 2412-2419. [Chapter 4]

[3] R. Machida, T. Nakazawa and N. Furuta.
Temporal changes of size distribution of mass and relative intensity for ablated particles during laser ablation inductively coupled plasma mass spectrometry.
J. Anal. At. Spectrom., 2015, **31**, 809-814. [Chapter 3]

[4] R .Machida, R. Nishioka, M. Fujiwara and N. Furuta.
Determination of trace elements in single-crystal silicon carbide by laser ablation in liquid ICP-MS., to be submitted. [Chapter 5]

Acknowledgements

The author wishes to thank all people who supported this work. First, I would like to express my sincere appreciation to Professor Naoki Furuta (Chuo University) for giving me the valuable opportunity. I couldn't have done this work without the great deal of his support.

I am deeply grateful to Professor Toshitaka Funazukuri, Professor Kenji Katayama, Professor Ichiro Shoji (Chuo University), and Professor Takeshi Hirata (Kyoto University) for their helpful advices on improving this thesis.

I would like to express my gratitude to Dr. Richard E. Russo (Lawrence Berkeley National Laboratory), Professor Detlef Günther (ETH Zürich), and Dr. Jhanis Gonzalez (Applied Spectra, Inc.). They gave me some valuable suggestions when we met at an international conference in the USA and a special lecture in Japan.

I had attended a doctoral course while belonging to the Sumika Chemical Analysis Service, Inc. I appreciate all the person for helping my job.

I would also like to thank all past and present Furuta's laboratory members for not only their help in this work but also for their kindness. I sincerely want to give special thanks to Dr. Takashi Nakazawa, Mr. Masahide Fujiwara, and Ms. Yuka Sakuraba for performing my work together. Dr. Masaki Ohata (The National Institute of Advanced Industrial Science and Technology) is a senior of this laboratory and a good teacher on LA-ICPMS. I also wish to thank his warm advice on this work.

Last, but certainly not least, I want to thank my wife, a son, a daughter, and parents for constantly supporting me in every aspect of my life.

March 24, 2016

Ryo Machida